Wesleyan University The Honors College

Our Stellar Neighborhood: Analysis of the Local Interstellar Medium using Absorption Spectroscopy

by

Julian Dann
Class of 2017

A thesis submitted to the
faculty of Wesleyan University
in partial fulfillment of the requirements for the
Degree of Bachelor of Arts
with Departmental Honors in Astronomy

Middletown, Connecticut April, 2017

Acknowledgements

Many thanks to my advisor Seth Redfield, who has allowed me to learn at my own pace, supported my efforts, and provided constant enthusiasm and encouragement.

Thank you to all of our research group for listening to our ISM gibberish. After two years of group meetings, I have learned a lot about the research process and appreciate the easygoing and accepting environment. Special shout-out to Wilson Cauley for his probing questions and suggestions that have helped me gain a better understanding of my material.

Special thanks to Girish Divurri, who I believe has now grown to accept me as a friend (about time)! Girish has always been willing to help piece over complicated problems and shared my excitement of new plots.

Thanks to Simon Wright for always having an iphone charger that kept me from being a lonely hermit in the basement.

To our ever-present proverbial observatory bird, Sarah Corner, thank you for bringing coated popcorn and smiles.

We would like to acknowledge NASA HST Grant GO-12278 and GO-13346 awarded by the Space Telescope Science Institute, which is operated by the Association of Universities for Research in Astronomy, Inc., for NASA, under contract NAS 5-26555, and a student fellowship from the Connecticut Space Grant Consortium for their support of this research.

Contents

1 Introduction **1**

1.1 Overview of the Interstellar Medium 1

1.2 Observing the ISM 7

1.3 The ASTRAL Dataset 9

1.4 Space Telescope Imaging Spectrograph 10

1.5 Historical Data and Models 11

1.6 *Breakthrough Starshot* 12

2 Methods **15**

2.1 Observing Absorption Profiles with *HST* 15

2.2 Observed Ions 18

2.3 Broadening Mechanisms 20

2.4 Predicting the Stellar Continuum 21

2.5 Challenges due to Spectral Type 24

2.6 Fitting Interstellar Absorption 24

2.7 Determining Uncertainty and Errors 26

2.8 Geocoronal Emission and Absorption 28

3 In Depth α Centauri **29**

3.1 Introduction to the Star System 29

3.2 Observations . . . 31
3.3 Historical Analysis . . . 32
3.3.1 Flux Calibration . . . 32
3.3.2 Wavelength Calibration . . . 33
3.3.3 Final Profiles . . . 35
3.4 Fits for α Centauri A & B . . . 38
3.5 Electron Density . . . 39
3.6 Dust Composition . . . 45
3.7 Dust Grain Size . . . 47
3.7.1 The Weingartner Dust Model . . . 51
3.7.2 Discussion of Grain Size distribution . . . 55
3.8 Temperature and Turbulence . . . 57
3.9 Implications on Breakthrough Starshot . . . 59

4 ASTRAL Stars **61**

4.1 Post-processing of STIS Spectra . . . 61
4.2 ASTRAL Fits . . . 62
4.3 Temperature and Turbulence . . . 75
4.4 Red Giant Stars . . . 81
4.5 Depletion . . . 82
4.6 Discussion . . . 85
4.6.1 HD 48915 . . . 85
4.6.2 HD 172167 . . . 86
4.6.3 HD 87901 . . . 87
4.6.4 HD 108903 . . . 87

5 Conclusion **89**

5.1 Back to *Breakthrough Starshot* 94

5.2 Future Work 95

Bibliography **97**

Chapter 1

Introduction

1.1 Overview of the Interstellar Medium

The interstellar medium (ISM) is the formal name for the space between stars in the Milky Way. Space, commonly imagined as an empty vacuum, is actually full of clouds of gas and dust, which are constantly interacting. These clouds of gas and dust are the medium in which stars are formed, spend their main-sequence lifetimes, and eventually die in. If you are so lucky to live in a place where the Milky Way is visible (Figure 1.1), you know first hand what I have been studying. As a resident of the Milky Way, you live in the outer part of one of the spiral arms, about 8 kiloparsecs, or 26,000 light years, from the center of the galaxy (Francis & Anderson 2014). There is an incredible amount of gas and dust between our solar system and the center of the galaxy, making it difficult to observe astrophysical objects in the plane of the galaxy in the visible, UV, or in the soft X-ray (Osterbrock 1989). Therefore, when we look up at the Milky Way with our own eyes we see the dust lanes of the spiral arms. These are dense clouds in the ISM scattering the light from billions of stars in our galaxy and making it opaque in certain wavelengths.

Some of these clouds of gas and dust are remnants of dying stars, while others are active regions of star formations in which cold, dense molecular clouds collapse

Figure 1.1: Dust in the Milky Way as seen from an area with low light pollution. The bulge is the line of sight towards the center of the galaxy. (*cdn.pcwallart.com*)

to form a nuclear stellar core as gravitational potential overcomes pressure. These two regions define the extremes of the interstellar medium, in star formation regions, densities can reach $n \sim 10^5$ atoms cm^{-3}, whereas in hot, sparse regions the densities can be much lower ($n \sim 10^{-5}$ atoms cm^{-3}). In density alone, it spans ten magnitudes; the ISM is diverse! Far out in our spiral arm, we are removed from the nearest stellar nursery, and therefore the region around us has a low density, which is easily heated by stellar radiation. The broader region surrounding our solar system and other nearby stars is known as the Local Bubble, which has a radius of $r \sim 100$ parsecs. It contains the Local Interstellar Cloud (LIC) with a density of $n \sim 0.3$ atoms cm^{-3} and the G-Cloud, as well as about a dozen other similar structures (Redfield & Linsky 2007). These clouds of gas and dust have distinct physical characteristics caused by their stellar neighbors. While the ISM is composed of both gas and dust, it is important to note that gas constitutes the vast majority of mass at over 99%. Approximately 91% of that gas is hydrogen, and only 0.1% of atoms in the ISM are heavier than helium (Boulanger et al. 2000). According to astronomers, and this thesis, all elements heavier than helium are considered metals.

The ISM is constantly changing due to the interaction of gas and dust with surrounding stars. The interaction between a star and its interstellar environment, known as stellar feedback, impacts the temperature, turbulence,density, composition, and ionization of the surrounding medium (Grisdale et al. 2017). A major contributor of stellar feedback is the stellar wind composed of supersonic charged particles that exit the star and stream outward in all directions creating a sphere of stellar influence. Different types of stars have different stellar wind strengths, therefore, models of stellar feedback on the ISM must adjust for stellar type. Post-main sequence stars, including red giants, have large mass loss rates, that can be observed in stellar spectra as saturated absorption features as shown in Figure 2.5.

Throughout a star's lifetime it interacts with the ISM in different ways. Young O and B stars emit lots of ultraviolet radiation creating spheres of ionization, first theorized by Bengt Strömgren in 1937. The neutral hydrogen surrounding the star becomes ionized and lose their electrons becoming a sphere of singly ionized hydrogen (H II). Many of the ions observed in the local interstellar medium are not neutral because they get ionized easily due to heating of the low density surrounding material. During their main-sequence lifetimes these stars have strong stellar winds that shoot radiation and charged particles constantly into its stellar neighborhood. As the star runs out of hydrogen to burn in its core, it transitions to burning helium. Some develop into Wolf-Rayet stars which have extremely high surface temperatures and strong stellar winds. At this stage they have completely lost their outer hydrogen layers. These strong winds inject lots of energy into the

ISM, but not quite as much as the next stage of stellar evolution. The star goes supernova, suddenly collapsing its core as it falls out of hydrostatic equilibrium after running out of fusible material. This ejects the outer layers of the star leaving either a black hole or a neutron star in its wake (Heger et al. 2003). These catastrophic events impact their environment long after they have faded away. Current measurements of the LISM support the theory that there was a recent supernova that caused heating and abundance of metals.

Supernovae are an important source of heavy elements in the interstellar environment. In a sense, they are recycling processes which infuse metals into clouds which become star formation regions. The Big Bang produced mainly hydrogen and helium and therefore the older stars all are metal-poor (Pop II), however, the injection of metals into the ISM from supernovae, has created stars with large metallicities (Pop I). In our depletion analysis, Section 3.6, we assume solar abundances of elements for all of the gas between our solar system and the target. However, the recent supernova theory could affect this assumption.

The boundary between our solar system and the LISM is important and informative because it is dependent on the environment through which our Sun travels. The edge of the solar system can be defined in many different ways. One possible definition is the region dominated by the solar wind. This bubble of solar wind around the Sun is known as the heliosphere, or the astrosphere for other stars. The edge of the heliosphere is the region in which the pressure of the solar wind is equal to the pressure of the interstellar medium around it. This border, called the heliopause, is highly variable and changes based on the pressure of the solar wind and the interstellar medium through which the Sun is travelling. As the solar wind approaches the edge of the heliosphere, it slows to subsonic speeds at the termination shock, then goes through a region of extreme turbulence and wave activity called the heliosheath. Another boundary at the edge of the solar system is formed when the relative motion of the star and its interstellar environment is supersonic. This boundary is a bow shock where a pileup of interstellar gas and dust slowly gets diverted around the finite body of the solar system. An interesting application of studying the interstellar medium is that we can observe astrospheric bow shocks and, using information about the surround ISM, indirectly measure the stellar wind. Strong stellar winds are known to strip the atmospheres of orbiting planets making it important for the habitability of exoplanets (Jakosky et al. 1994).

Studying the ISM has become more popular recently because of the increasing likelihood of an achievable interstellar mission. For the first time ever, we are receiving in-situ measurements of the interstellar medium from both *Voyager* spacecrafts. *Voyager 1*, a spacecraft launched by NASA in 1977, passed from our heliosphere into the LISM in 2013, making it the first human-made object to experience interstellar space (Fisk & Gloeckler 2014). Using the few remaining operable instruments on board, astronomers can take in-situ measurements of the extremely immediate interstellar environment for the first time. This is an incredible achievement and a great opportunity to study the extremely local interstellar medium.

However, astronomers have been studying the ISM for decades without help from the *Voyager* missions. Classical theories of the interstellar medium from Goldsmith et al. (1969), McKee & Ostriker (1977), and Wolfire et al. (1995) assume that the ISM is in thermal, steady-state equilibrium. These models have three defined regions: the cold neutral medium (CNM) with temperature $T \geq 50$ K, the warm neutral (WNM) or ionized medium (WIM) with $T \sim 8000$ K, and the hot ionized medium (HIM) with $T \sim 1{,}000{,}000$ K. The extreme low density of our immediate neighborhood, evidence of previous supernovae, and strong stellar winds are indications of the ISM being out of equilibrium. A new model of the interstellar environment was necessary to describe our immediate surroundings. Currently, Redfield & Linsky (2008) have identified fifteen discrete clouds based on observations of 157 lines of sight using absorption spectroscopy (Figure 1.2). The goal of this thesis is to build upon this model with more observations of heavy elements of previously observed and unobserved lines of sight. From old observations we can look for changes in ISM absorption features over time. With new observations we can improve the model by identifying new clouds and further constraining physical properties of known clouds. Many things can be inferred from studying absorption profiles of intervening clouds of gas and dust, such as temperature, turbulence, electron density, depletion, dust composition, and size distribution of dust molecules.

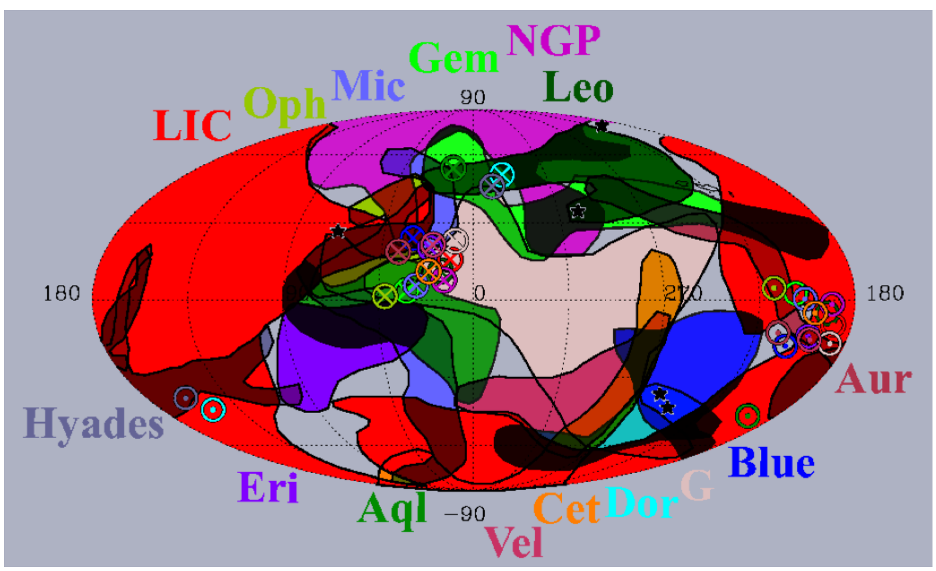

Figure 1.2: The fifteen cloud model from Redfield & Linsky (2008) where the upwind heliocentric direction of the velocity vector for each cloud is indicated by the $\otimes$ symbol and the downwind vector is represented by the $\odot$ symbol.

1.2 Observing the ISM

The interstellar medium was first discovered by Johannes Hartmann in 1904 who noted that the 393.4 nm calcium line had a distinct absorption feature that did not match the radial velocity of the star. This puzzled him, and led him to believe that it must have been caused by a cloud of gas and dust along the line of sight. For nearly a century, there was little astronomers could due to study the diffuse interstellar medium surrounding the Sun because the overwhelming majority of important resonance lines associated with the ISM are found in the ultraviolet, which is blocked by Earth's atmosphere (Figure 1.3). It was not until astronomers could launch their telescopes above the atmosphere, that they were able to observe in the ultraviolet. Before this, the most important lines that were observable were Na I and Ca II in the optical region of the electromagnetic spectrum.

In order to observe the diffuse local interstellar medium (LISM), astronomers use absorption spectroscopy. The low surface brightness of the LISM makes it only possible to observe by looking at the absorption of the LISM clouds against a bright background source. Spectroscopy is a measure of how much light is being received across a range of wavelengths. Atoms emit and absorb photons at characteristic wavelengths as electrons make bound-bound, or bound-free transitions. By observing these transitions in laboratories on Earth, astronomers can identify the atoms responsible for interstellar absorption found in stellar spectra. Incoming energetic photons from the background star are absorbed by atoms or molecules whose cross section is large compared with the wavelength of the photon. For any given ion, an associated photon of a particular wavelength gets absorbed before reaching the spectrograph, resulting in an absence of photons at that wavelength.

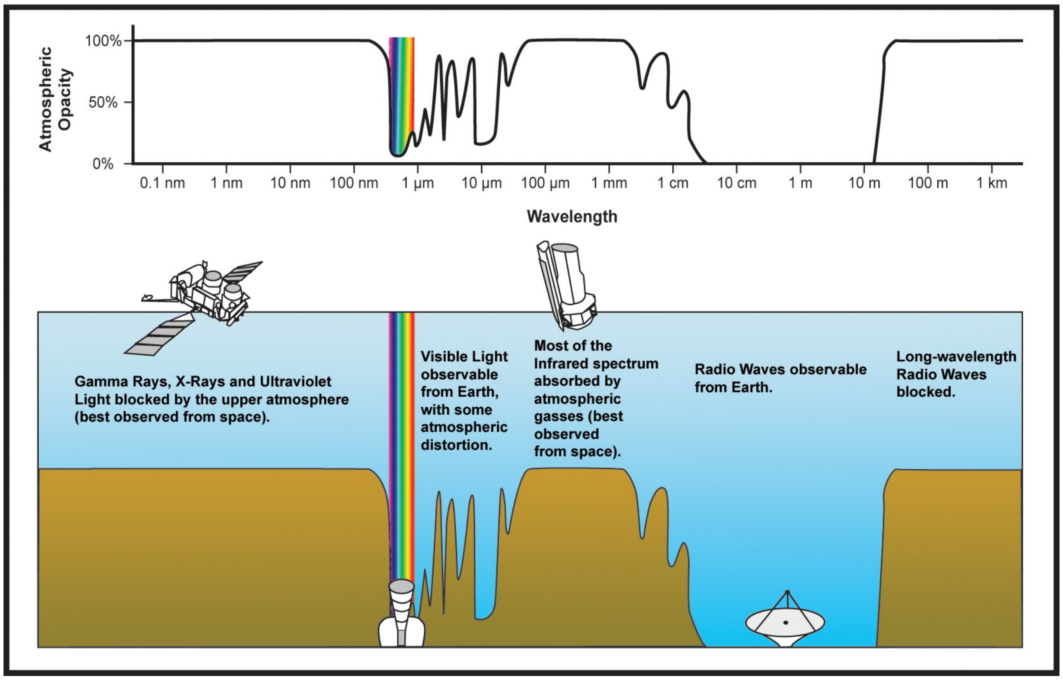

Figure 1.3: A cartoon of the transmittance of different wavelengths of light through Earth's atmosphere, showing the importance of space observatories for modern astrophysical observations (IPAC (2008)).

This photon bumps an electron up into a higher energy level or ionizes it, where it is lost or deexcites, emitting another photon in a different direction. The emission from ionization and heating of the cloud is much too faint to measure directly.

Absorption features can be described by three parameters: position (radial velocity), width (Doppler parameter), and depth (column density). Clouds of gas and dust in the ISM disrupt the stellar emission lines with deep and narrow features at the same radial velocities across all ion transitions present in the cloud. By observing a variety of ions for each sight line we can determine compositions along each line of sight by looking at the depth of absorption features. We can also look for ionization and electron density from these measurements. Using the width of features, we can constrain the temperature and turbulence of the cloud. A standard absorption feature is shown in Figure 1.4 with markers for the different parameters.

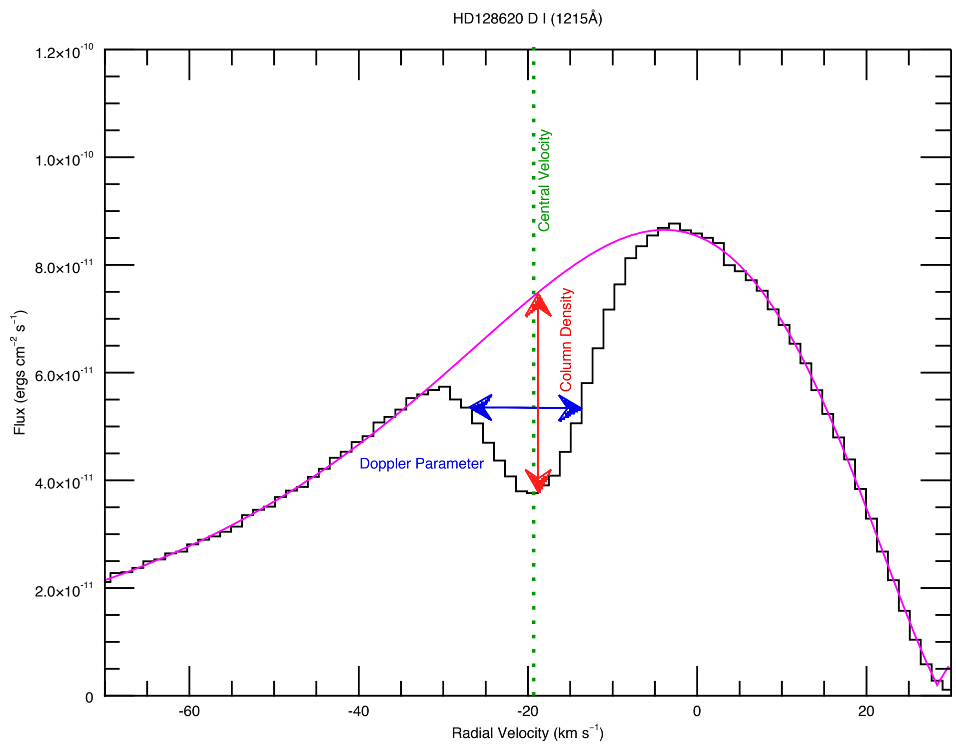

Figure 1.4: This plot is the DI 1215 Å transition for the sightline towards HD128620. The magenta shows the estimate for the stellar emission profile in the absence of the interstellar absorption. The parameters that describe the Voigt profiles we fit to the feature are illustrated on the feature.

1.3 The ASTRAL Dataset

This project used a dataset provided by the Advanced Spectral Library Project (ASTRAL), whose goal is to collect high-quality ultraviolet spectra of nearby bright stars using *Hubble Space Telescope's* Space Telescope Imaging Spectrograph (*HST*/STIS). I used spectra from 13 different sightlines that are categorized as cool G/F/K/M stars, hot B/A stars, or red giants. Each stellar classification presented different challenges to fitting.

Strong interstellar transition lines are primarily found in the ultraviolet, which is blocked by Earth's atmosphere. As can be seen in Figure 1.3, the atmosphere is opaque at wavelengths less than $\lambda \sim 3000$ Å. Before the development of sounding rockets or satellites, there was little that could be done to observe the interstellar medium. The *Hubble Space Telescope*, placed in low Earth orbit in 1990, changed our understanding of interstellar space and has served as our eyes for the LISM ever since.

1.4 Space Telescope Imaging Spectrograph

Using *HST*/STIS, astronomers have been able to obtain high resolution spectra with resolutions $R \equiv \lambda/\Delta\lambda > 100,000$. ASTRAL observations span the near UV from $\lambda \sim 1150 to 3000$Å with the use of at least two different echelle gratings. These gratings are used at high incidence angles to separate high diffraction orders allowing for higher resolutions. For all exposures, a high (H) or medium (M) resolution grating is used for the far-UV, named E140H or E140M. The near-UV exclusively uses the E230H grating for high resolution observations of all targets. The high resolution echelle gratings produce a resolving power of $R \equiv \lambda/\Delta\lambda = 114000$ while the medium resolution produces $R \equiv \lambda/\Delta\lambda = 45800$. In 2004, the instrument failed and was not repaired until another mission in 2009, therefore we cannot look for historical changes in that period. Before STIS, *HST* had a different spectrograph on board called the Goddard High Resolution Spectrograph (GHRS). GHRS was one of the original four pieces of equipment aboard *HST*. It could observe between $1150 - 3200$ Å, but could not take high resolution spectra over large wavelength ranges. Instead, small chunks of the UV of $\lambda \sim 20$ Å could be requested at $R \equiv \lambda/\Delta\lambda > 100,000$. It was replaced during a servicing mission in 1997 by the Space Telescope Imaging Spectrograph (STIS) which was able to observe broader wavelength ranges at an even higher resolution. STIS was used to take all of the data for the ASTRAL project. Using the Mikulski Archive for Space Telescopes (MAST), we can compare spectra for certain stars in our sample over more than twenty years. Using this archived data, we can look for changes in the radial velocity, broadening, and depth of different ion transitions in each spectra. We perform this analysis on α Centauri A and B, the most frequently observed system in our sample.

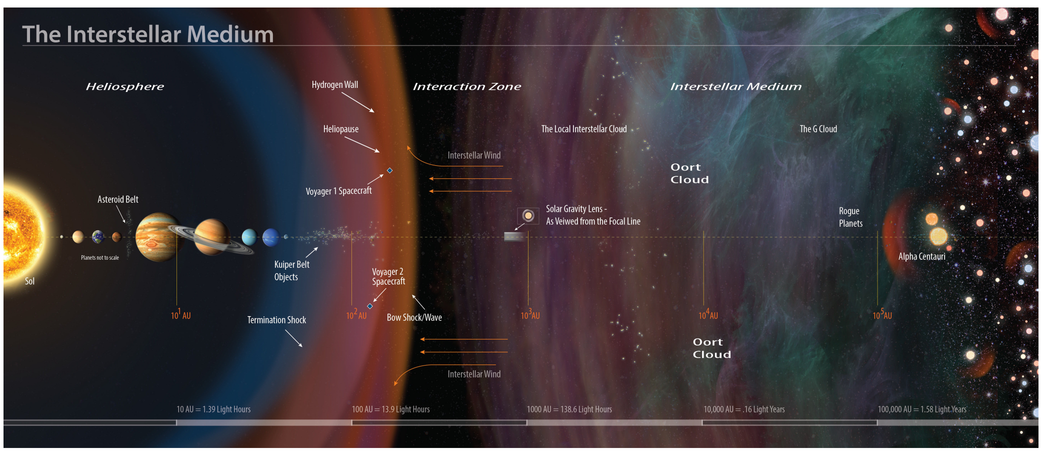

Figure 1.5: A depiction of the structure between us and α Centauri. It shows the structure of the heliosphere and the interstellar clouds along the line of sight.

1.5 Historical Data and Models

The process of fitting absorption features is complicated and can at times seem subjective. Because of this, it is important to look at other times these sight lines have been observed for ISM absorption features. Over the last twenty years the main people working on the local interstellar medium have been Thomas Ayres, Jeffrey L. Linsky, Rosine Lallement, and Seth Redfield all using the *HST* for absorption spectroscopy. Their work helps to verify our own, as well as inform us of how each sight line may have changed over time. In this work we have at

Table 1.1: The ASTRAL cool and hot stars.

Object Name (1)	Proper Name (2)	Distance (pc) (3)	V_{rad} (km/s) (4)	Stellar Type (5)
HD 128621	α Cen B	$1.255^{+0.039}_{-0.42}$	-20.70 ± 0.9	K1V
HD 128620	α Cen A	$1.325^{+0.0072}_{-0.0073}$	-21.40 ± 0.76	G2V
HD 48915	α CMa	$2.637^{+0.011}_{-0.011}$	-5.50 ± 0.4	A1V+DA
HD 61421	α CMi	$3.514^{+0.015}_{-0.016}$	-3.20 ± 0.9	F5IV
HD 172167	α Lyr	$7.679^{+0.021}_{-0.021}$	-20.60 ± 0.2	A0Va
HD 62509	β Gem	$10.358^{+0.029}_{-0.029}$	3.23 ± 0.02	K0III
HD 432	β Cas	$16.784^{+0.11}_{-0.11}$	4.30 ± 0.8	F2III
HD 87901	α Leo	$24.313^{+0.21}_{-0.21}$	5.90 ± 2.0	B8IVn
HD 108903	γ Cru	$27.152^{+0.13}_{-0.13}$	21.00 ± 0.1	M3.5III
HD 164058	γ Dra	$47.304^{+0.22}_{-0.22}$	-27.91 ± 0.19	K5III
HD 17573	41-Ari	$50.787^{+0.49}_{-0.49}$	4.00 ± 4.1	B8Vn

times overlaid old spectra on the ASTRAL dataset, to look for changes in centroid velocity, width, and depth. We also fit magnesium absorption for various archived spectra to compare our values with theirs. From this we can infer changes in the cloud structure in between *Hubble* and the background star.

For each sightline we can also look at the prediction given from the Redfield Kinematic Model[1] developed in Redfield & Linsky (2008) which uses 270 measurements for 157 lines of sight to radial velocities of clouds traversing our lines of sight. From these measurements, 15 discrete clouds within 15 parsecs were identified by having common radial velocities, compositions, turbulence, and temperatures. For any line of sight it produces a list of clouds that traverse and clouds that are within 20°.

1.6 *Breakthrough Starshot*

In the last few decades interstellar travel has been seen as a more achievable goal. Projects, like *One Hundred Year Starship* and *Breakthrough Starshot*,

[1] http://lism.wesleyan.edu/LISMdynamics.html

have been announced making it imperative to understand the very local interstellar medium. On April 12th 2016, Yuri Milner announced the *Breakthrough Starshot Initiative*, a privately funded mission whose aim is to send thousands of nano-spacecraft to α Centauri, the closest star system only 1.3 parsecs away (van Leeuwen 2007). Part of the enthusiasm for this mission is because of the discovery of a possibly habitable planet orbiting the faintest of the three star system, Proxima Centauri (Anglada-Escudé et al. 2016).

The advance of technology has allowed electrical engineers to make everything much smaller, therefore a large spacecraft may never be necessary except for manned missions. This nanocraft would be gram-scale and could carry cameras, photon thrusters, a power supply, and communication equipment while significantly reducing the force needed to accelerate. Because of how small it is, they predict that they will be able to get the spacecraft to $v \sim 0.2c$ using a light sail as illustrated in Figure 1.6. At this rate, it will reach α Centauri within our generation! ($\sim$ 20 years after its launch) A similar method of propulsion is already in use today with solar , which harness the momentum of charged particles and radiation in the solar wind. For *Breakthrough Starshot*, the momentum will come from a massive phased array of lasers on Earth [2].

While the project is in the proof-of-concept stage, we can begin planning for the issues it would encounter between us and α Centauri. Since the announcement of the project, many scientists have rushed to help solve the problems it presents. Hoang et al. (2016) models the effect gas and dust could have on the spacecrafts as they travel through the ISM. They conclude by asking for an in depth analysis of the dust along the line of sight. More specifically, the main problem could be the collision of these tiny spacecrafts, referred to as "StarChips", with large dust

[2]https://breakthroughinitiatives.org/Initiative/3

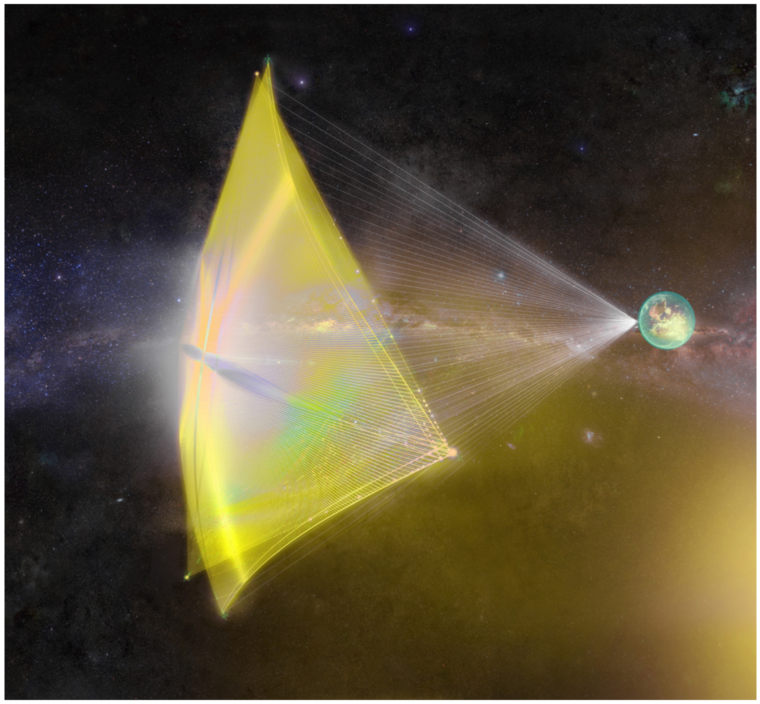

Figure 1.6: An illustration of the proposed *Breakthrough Starshot Initiative* showing the light sail propelled by lasers on Earth. (*https://breakthroughinitiatives.org*)

particles, therefore we must constrain their composition and size distribution. Part of this thesis will be a response to this article by looking in depth at the HD128620 (α Cen A) and HD128621 (α Cen B) sightlines.

Chapter 2

Methods

2.1 Observing Absorption Profiles with *HST*

Within stellar spectra there are three main contributors: the continuum, emission lines, and absorption lines. The continuum is caused by the blackbody radiation of the star, which is a function dependent only on the effective temperature of the body. Emission lines are caused by gas in the stellar atmosphere emitting photons, while absorption profiles are caused by intervening material absorbing, scattering, or reflecting light from the background source star resulting in an absence of photons at a characteristic wavelength corresponding to the absorbing particle. All three processes are found in our stellar spectra. It is the absorption, however, that yields direct information about the interstellar clouds of gas and dust along the line of sight.

Absorption spectroscopy allows astronomers to observe dim astronomical objects that block light from bright background objects like stars. In order to identify ISM components, we look at specific transitions of elements that are likely to be found in the ISM, and look for deep and narrow features at the same radial velocity over a range of ion transitions. A consequence of absorption spectroscopy is not knowing the radial extent of the clouds along the line of sight. We can, however, distinguish between different clouds by their radial velocities. A procedure is needed when absorption profiles are close enough to overlap and blend without giving distinct local minima, like in Figure 2.2. From these characteristic absorption profiles, we can constrain the temperature, turbulence, electron density, depletion, dust size, and dust composition of individual clouds along the line of sight.

With the use of the Space Telescope Imaging Spectrograph on *HST*, we have been able to look at a large range of ion transitions between 1150 Å and 3100 Å. This is the ideal wavelength band for LISM observations because it has a huge number of important metal lines. Even though the ISM is composed primarily of hydrogen, the metal composition is an important tracer for dynamic processes in interstellar space. In order to identify important ion transitions, we looked to Redfield & Linsky (2002), Redfield & Linsky (2004b), Redfield & Linsky (2008), and others. Morton (2003) is used to find the rest wavelengths of ion transitions in a vacuum, the gamma coefficient, and the oscillator strength based on laboratory results. The gamma coefficient is a measure of the natural broadening of the line profile. Natural broadening is a consequence of Heisenberg's uncertainty principle in the lifetime of energy states of the electrons. The oscillator strength is a measure of the probability of an atom to absorb or emit photons as the ion transitions between energy states. With these ion transition properties, we can fit absorption features and make direct comparisons between ions.

An important consequence of using absorption spectroscopy to study the LISM, is that the farther away we look, the more material we must look through. The more material in between us and the background star, the higher the likelihood that features will be saturated and blended. Saturated features are the result of ISM clouds absorbing all of the light at a certain wavelength (Figure 2.1). By losing information about the bottom of the feature, we lose confidence in our ability to identify the number of local minima or clouds, an accurate Doppler parameter (a measure of width), and the true column density (a measure of depth). This is a major concern for red giants, whose winds saturate and obscure the continuum. In the case that the ISM absorption feature is fully saturated, we can look at other transitions with lower oscillator strengths in Morton (2003).

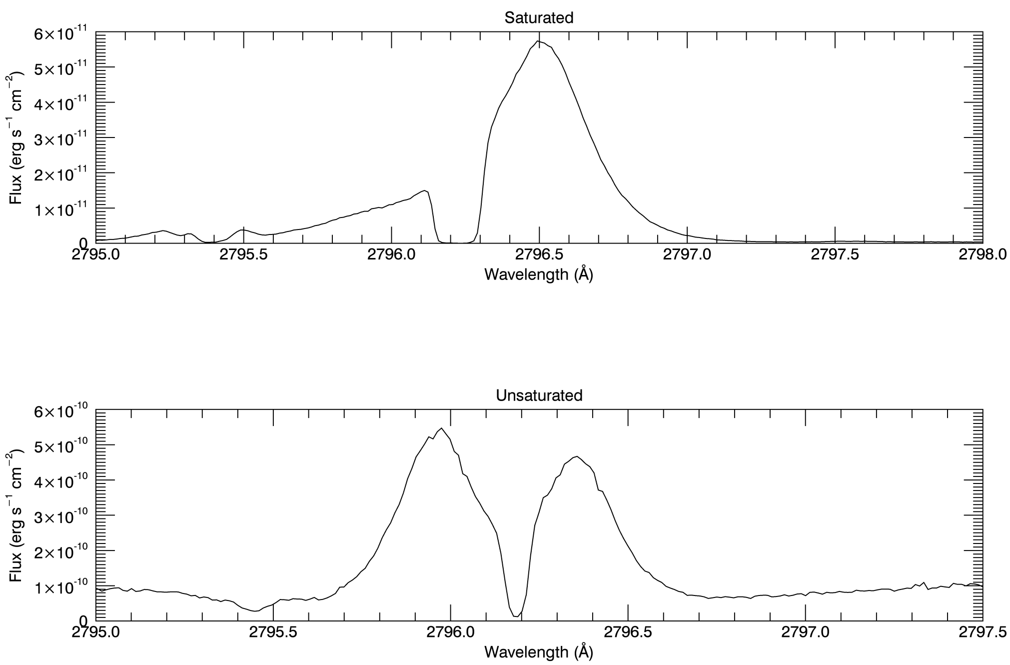

Figure 2.1: Saturation of Mg II 2796 Å transition for two different lines of sight. The top line profile shows how much information is lost by having a saturated line. We cannot accurately measure the true width, depth, or number of components for that line of sight without looking at other transitions with a lower oscillator strength to reveal the bottom of the feature. The bottom panel shows a different line of sight where you can get accurate measurements and identify multiple clouds.

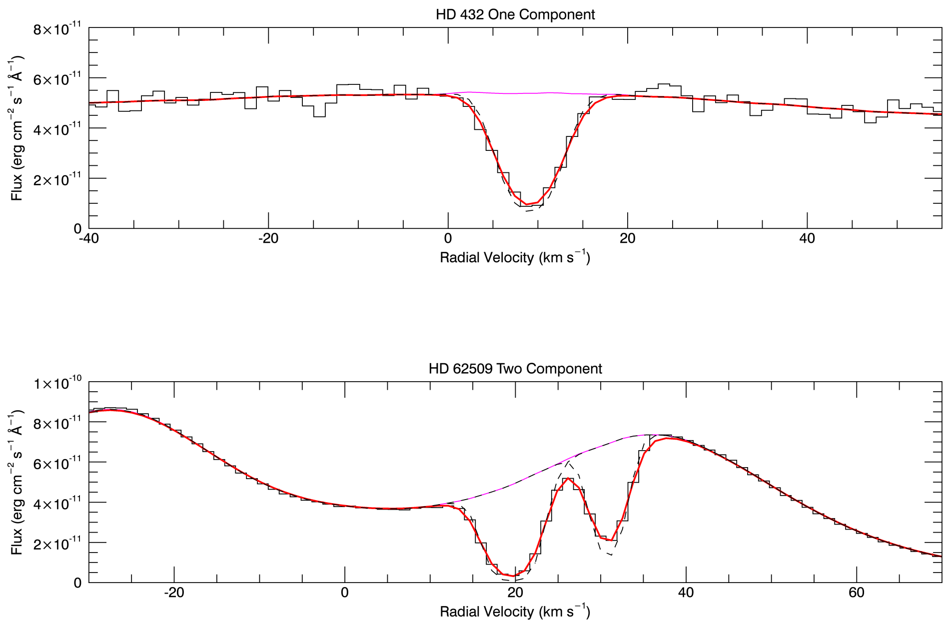

Figure 2.2: This shows MgII 2796 Å for two different sight lines, the top panel is a one component fit, the bottom panel has two discrete local minima at different radial velocities indicating the presence of two clouds. The black line is the data, the magenta is the fitted continuum, and the solid red line is the fit generated by *gismfit.pro*

2.2 Observed Ions

The ASTRAL targets used for the main study were taken in May 2015 with the Space Telescope Imaging Spectrograph (STIS) on board *HST*. STIS began operating in 1997 after the termination of the Goddard High Resolution Spectrograph (GHRS). STIS has three 1024×1024 detector arrays and can observe in both the UV and the optical with resolution up to $R \equiv \frac{\lambda}{\Delta\lambda} \sim 114,000$ for E140H and E230H. For our dataset, STIS used echelle gratings: E230H, E140H, and E140M to produce the spectra. Echelle gratings are carefully grooved surfaces used to diffract light for increased dispersion of spectral features. Such high resolution is necessary because of the importance of true line widths to the study. With these

Table 2.1: Observed ions

Ion (1)	λ_{vac}(Å) (2)	AB/GAMMA (3)	F (4)
D I	1215.3376	$6.27e+08$	$2.777e-01$
C II	1334.5323	$2.880e+08$	$1.28e-01$
C II Excited	1335.6627	$2.880e+08$	$1.28e-01$
....	1335.7077	$2.880e+08$	$1.15e-01$
N I	1199.5496	$4.104e+08$	$1.328e-01$
....	1200.2233	$4.097e+08$	$8.849e-02$
....	1200.7098	$4.093e+08$	$4.423e-02$
O I	1302.1685	$5.750e+08$	$4.887e-02$
Mg II	2796.3543	$2.162e+08$	$6.123e-01$
....	2803.5315	$2.592e+08$	$3.054e-01$
Si II	1190.4518	$3.503e+09$	$2.502e-01$
....	1193.2897	$3.495e+09$	$4.991e-01$
....	1260.4221	$2.533e+09$	$1.007e+00$
....	1304.3702	$1.720e+09$	$1.473e-01$
....	1526.7066	$1.960e+09$	$2.303e-01$
Fe II	2585.6500	$2.720e+08$	$6.457e-02$
....	2600.1729	$2.700e+08$	$2.239e-01$

Table 2.2: Table showing all of the ions observed with their rest wavelengths in a vacuum, their gamma factors, and their oscillator strength taken from Morton (2003).

configurations, the spectra spans from 1100 Å to 3100 Å. (The E140M echelle grating produces spectra with a resolution of R $= \frac{\lambda}{\Delta\lambda} \sim 45,800$.)

The ultraviolet region of the electromagnetic spectrum is particularly useful because it has a large amount of metal transition lines that are found in the ISM. Earth's atmosphere is opaque in the near-UV, so it is necessary to use space observatories to observe this important part of the electromagnetic spectrum. While the ISM is made up of only 0.1 % metals, it is these transitions that are most informative because hydrogen is always saturated. We look at ion transitions for deuterium, carbon, nitrogen, oxygen, magnesium, silicon, and iron (See Table 2.1).

2.3 Broadening Mechanisms

When fitting absorption features, we take into consideration three different parameters: λ_{cen} the centroid wavelength/velocity, b the Doppler parameter (width), and $\log N$ the column density (depth). The Doppler broadening parameter is caused by a wide variety of velocities of atoms and molecules in an interstellar cloud. It can be dominated by thermal motions, in which random motions of a heated gas result in a fast and slow population and/or governed by turbulent motions.

The other main broadening mechanisms are natural broadening and collisional broadening. Natural broadening is a result of the uncertainty principle, which relates the lifetime of the excited states with the uncertainty of its energy, in decaying atoms where the time of the initial state and final state define the width due to this mechanism. Collisional broadening is caused by particles colliding with excited atoms and dislodging an electron and a resultant photon, which reduces the effective lifetime of emission, therefore, turbulent areas have broader line profiles. In general however, the most important broadening mechanism in the ISM is the Doppler component because the LISM is not dense enough for sufficient collisions.

Part of the challenge of my work will be to distinguish between thermal and turbulent Doppler broadening. This is spelled out in greater detail in Redfield & Linsky (2004b). Accurate constraints on temperature and turbulence are placed by comparing the observed line widths of ions with different atomic masses. The observed line width b (the Doppler parameter) is related to the temperature (T)

and turbulent velocity (ξ) in Equation 2.1.

$$b^2 = \frac{2kT}{m} + \xi^2 = 0.016629\frac{T}{A} + \xi^2, \tag{2.1}$$

where k is the Boltzmann constant, m is the mass of the ion, and A is the atomic weight of the ion in atomic mass units (amu). This method is only possible if the width of the line profile is well known, which requires the absorption feature to be unsaturated. This method is most effective when comparing ions that have very different masses. The ideal ions to use are hydrogen and iron, however because of how abundant hydrogen is in the ISM, it is easier to fit for the absorption of deuterium which has a neutron in addition to the single proton in the nucleus of the atom. This can be seen in Figure 2.3 where hydrogen lines, such as Lyman-α at 1215 Å, reveal structures apart from interstellar clouds. In this transition we also see heliospheric and astrospheric absorption, which can blend with the interstellar component (Linsky & Wood 1996). Deuterium is a great alternative because it is the next lightest ion and is generally unsaturated making for simple fitting of the interstellar absorption profile.

2.4 Predicting the Stellar Continuum

In order to fit interstellar absorption features we must first reconstruct the emission of the star as it would appear in the absence of intervening gas and dust. Stars radiate as blackbodies in accordance with Planck's law, meaning that stars emit light at all wavelengths with the peak wavelength given by Wien's law,

$$\lambda_{max} = \frac{2900\mu m}{T} \tag{2.2}$$

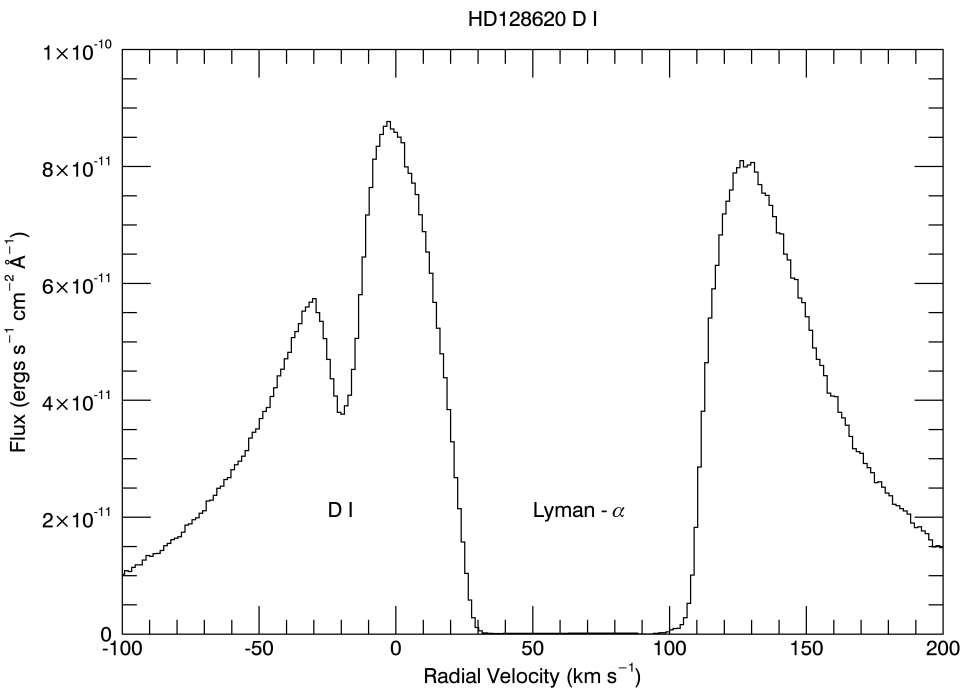

Figure 2.3: A depiction of absorption of Lyman-α (1215 Å) in comparison with the unsaturated deuterium for HD 128620.

Wien's law tells us that for hotter stars, the peak of the stellar continuum will be at shorter wavelengths. The STIS spectrograph on board the *Hubble Space Telescope* records high resolution data in the ultraviolet from 1100 Å to 3100 Å so the easiest stars to fit will be the hot A/B stars in the ASTRAL sample because the peak of their continuum is in the ultraviolet. The cool sun-like ASTRAL stars peak in the optical and present a greater challenge when predicting continuum because of more prominent stellar emission lines. An example of this can be seen in Figure 2.4, where the interstellar absorption is found in the middle of stellar emission lines and can be blended with strong stellar winds if they are present.

The program *mkfb.pro*, written by S. Redfield uses a least-squared polynomial fit to "bridge the gap" over regions of absorption (Redfield & Linsky 2002). The

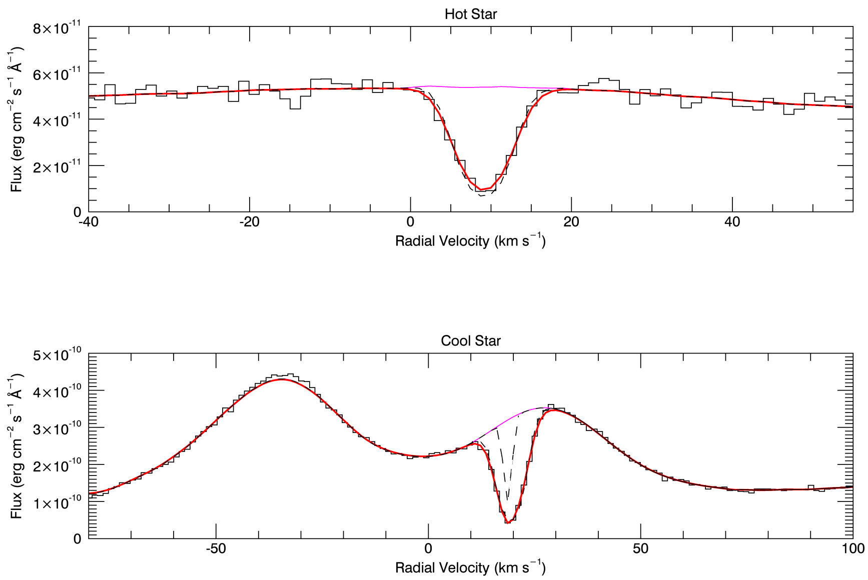

Figure 2.4: The top panel shows the continuum of a hot star which is shifted towards shorter wavelengths as described by Wien's Law (Equation2.2). Because of this, it is much easier to predict that the more confusing profile of the cool star in the lower panel. The magenta line is the predicted continuum using the least-squared polynomial fit.

order of the polynomial is influenced by the type of star and the signal to noise ratio. In general, cooler stars need higher order polynomials to account for the more noticeable stellar emission lines. The polynomial fit takes into account data selected from directly shortward and directly longward of the absorption feature. There is an art to this, there are times in which more or less data should be used, and the data bracketing the absorption can play a huge role in the resultant fit. For some lines of sight, the clouds have significantly different radial velocities and the continuum can be seen between the absorption features. In this case, three segments of the continuum are identified for fitting. When fitting lines of different oscillator strengths, if the resulting fits are higher or lower than the absorption feature it is an indicator that the height of the continuum is incorrect and should be adjusted.

2.5 Challenges due to Spectral Type

Stellar spectra are different based on what type of star is being observed. Due to Wien's law, we know that the hotter the star the shorter its peak wavelength will be. The easiest stars to fit therefore are the hot stars whose continuum is higher in the UV making it easier to find where the line would be without the absorption feature. The hardest stars to fit were the red giants because they have much stronger stellar winds that produce added absorption than can get in the way of the interstellar absorption, see Figure 2.5. The wind from red giant stars increases along the asymptotic branch due to an increase in radius and a lower surface gravity. The velocities from this wind result in broadened absorption features around ion transitions.

2.6 Fitting Interstellar Absorption

After making the stellar continuum, we can then fit the absorption using *gismfit.pro* program written by S. Redfield and B. Wood and used in LISM studies such as Redfield & Linsky (2002). The absorption features are fit using Voigt profiles, which is the combination of Gaussian and Lorentzian profiles. The process begins by assuming that there is only one cloud along the line of sight. In certain absorption profiles, it is clear that there are multiple clouds because of multiple local minima in the absorption. However, lines of sight that actually have one cloud can be fit better with multiple components, this may be a trap! An F-test is performed to determine if the multiple component fit does a considerably better job based on its χ^2 value. The F-test is an important tool that quantifies the "goodness of fit" and often suggests that the fit with more components is not

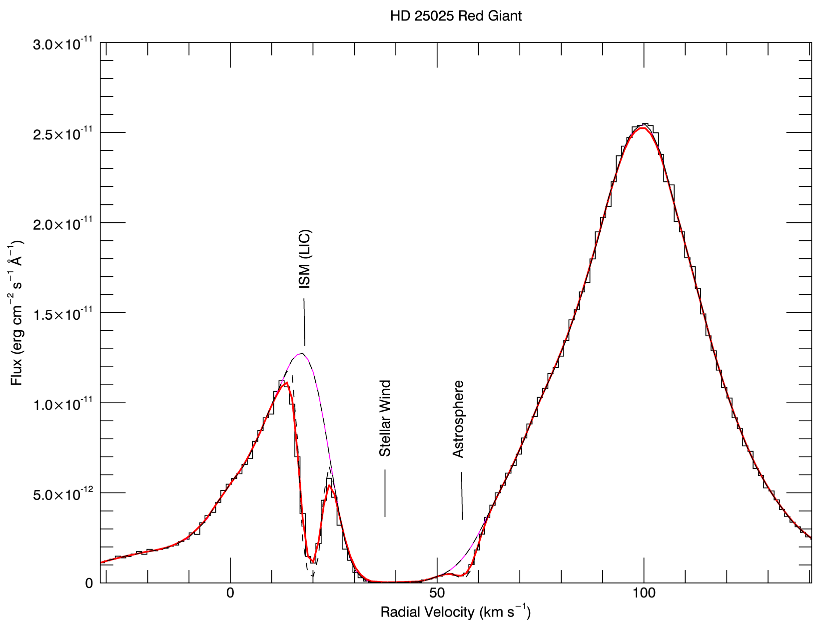

Figure 2.5: This is a red giant star (HD 25025), with broad stellar wind absorption features as well as interstellar absorption around the Mg II (2796Å) transition. This makes it difficult to fit a continuum. There is one ISM absorption feature and one feature caused by the astrosphere, these are identified as divergences of the data from the magenta continuum.

significantly better to justify the existence of another cloud along the line of sight.

Fitting a line profile requires approximations of the centroid of absorption, the Doppler width, and the column density (depth). The rest wavelength of the ion transitions in a vacuum, the gamma factor, and the oscillator strength for the given ion transition given in Morton (2003). This information is made into an input file for each star and ion transition and imported into the *gismfit.pro* program. The program also requires the continuum made by the *mkfb.pro* program. When the fit is too high or too low, it is often a result of an inaccurate continuum. This is a convenient check on the continua, and allows us to go back to fix the continuum.

Systematic errors associated with the central radial velocity of the absorption feature, the Doppler parameter, and the column density can be mitigated by looking at multiple resonance lines. C II, N I, Mg II, Si II, and Fe II have multiple lines for the same transition that can be fit together. These multiplets are important checks to make the measurements more accurate. The different resonance lines only change in their oscillator strengths, so certain lines will be deeper and others shallower. A larger oscillator strength is associated with deeper transitions. In the case that there is too much saturation or not enough absorption we can look for other lines that would give more information.

2.7 Determining Uncertainty and Errors

The first step for determining uncertainty in our measurements is to take a Markov Chain Monte Carlo (MCMC) of the fit parameters. The Monte Carlo method is a random sampling to determine the probability of the outcome of the fit, it is often used when systematic errors overshadow random errors. The simulation generates random values for parameters around the initial guesses for the centroid, Doppler parameter, and column density. One hundred iterations of the simulation is sufficient to approximate the uncertainty of each fit parameter. It is useful to neglect doing a MCMC until the values are somewhat constrained, as the MCMC will fail if the guesses are too far off.

Looking at ions with multiple resonance lines is a key method for reducing random errors and getting a better approximation of key parameters. Each multiple resonance line is fit individually but also combined, where the parameters for each individual line are fixed together. Fixing the components between resonance lines is possible because the only differences between the two lines should be the gamma factor and the oscillator strength. This provides a second check on the fit. Mg II and Fe II have two such lines in the near-UV, however NI has three lines and Si II has five allowing for a rigorous fitting method. Once each line is fit individually and combined we can take a weighted mean based on their associated error from the MCMC. To further reduce systematic error, we take a standard deviation of the values and use the larger of the error between the two methods. It is important to take the column densities out of log space before calculating error for it. This process leads to single values and errors for the central velocity of the component, the Doppler parameter, and the column density that you can use to determine other physical properties.

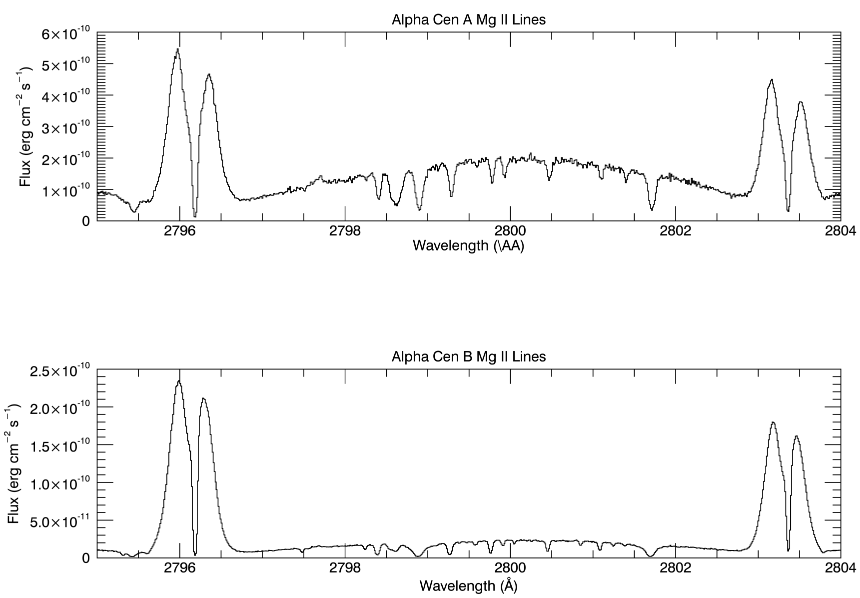

Figure 2.6: Magnesium absorption features for HD 128620 and HD 128621 showing the similarities between multiplet lines and the significant difference in the continuums based on their stellar types. HD 128620 (α Cen A) is a hotter star (G) which has a higher continuum at shorter wavelengths. HD 128621 (α Cen B) a cooler star (K) peaks at $\lambda \sim 7000$Å meaning its continuum will be much lower as it is much less likely to radiate as a blackbody in UV wavelengths.

2.8 Geocoronal Emission and Absorption

In certain elements, usually nitrogen and oxygen, there is an added absorption feature due to absorption of phtons in Earth's upper atmosphere. These geocoronal absorption features are caused by particles in the upper atmosphere absorbing lights at characteristic wavelengths corresponding to the cross-sectional area of the particle. It can also be seen in geocoronal emission, also known as "airglow", in Lyman-α in which hydrogen particles in the upper atmosphere drop from the $n = 2$ energy level to the $n = 1$ ground state by emitting a photon with a wavelength of 1215.67 Å. These features are offset in stellar spectra by the velocity at which Earth is moving with respect to the RA and DEC of the target. This can be calculated by obtaining ephemeris information for heliocentric and barycentric velocity vectors from *baryvel.pro* (NASA distributed function). With this it can be projected along the line of sight, this can be seen in Figure 4.23.

Chapter 3

In Depth α Centauri

This chapter addresses two stars within the ASTRAL sample that are particularly exciting because of the aforementioned *Breakthrough Starshot* mission. By studying the spectra in our sample toward α Centauri (HD 128621 and HD 128620), we can get a better understanding of the interstellar environment through which the mission must travel in order to reach its target. The temperature, turbulence, electron density, dust composition, and the dust size distribution, will all play an important part in planning for *Breakthrough Starshot*. With this information, we hope that scientists on the project can create a better informed StarChip design to mitigate the challenges presented by interstellar travel.

3.1 Introduction to the Star System

As astronomical instruments have improved, astronomers have had to come to terms with the overabundance of planets in the universe. The first confirmed detection of an exoplanet came in 1992 using the radial velocity method, which looks for periodic motion in the motion of the host star to imply the presence of the gravitational pull of a planet (Wolszczan & Frail 1992). In the quarter century since this discovery, astronomers have discovered thousands more; it is now probable to find more than a planet around every star. Therefore, it is no surprise the European Space Agency announced, in 2016, the discovery of another nearby planet. Using the European Southern Observatory in Chile they discovered a planet slightly larger than Earth orbiting in the habitable zone of Proxima Centauri, a member of the nearest star system α Centauri (Anglada-Escudé et al. 2016). The habitable zone around a star is the region in which liquid water could exist based on the radiation being absorbed by a body at some distance and a range of possible greenhouse effects. However, habitability is much more complicated, and this term should be used with caution. The habitability of a planet can be influenced by the stellar wind, planetary magnetic fields, the planetary atmosphere, plate tectonics, and many other factors (Lammer et al. 2009). Even so, this planet, denoted Proxima Centauri b, is very exciting and warrants study, as it is by far the closest "habitable" exoplanet. α Centauri, our closest stellar neighbor, is composed of three stars: α Centauri A (G2V), α Centauri B (K1V), and Proxima Centauri (M6Ve). α Centauri A & B are in a tight binary orbit with a period of 79.90 years (Hartkopf et al. 2001). The outcast of the system, Proxima Centauri, orbits its companions about 500 times farther out than Neptune does our Sun ($\sim$ 15000 AU) (Reipurth & Mikkola 2012). Because of its proximity and brightness, the system has been a common target for astronomical observations. In fact, it was only the second binary system ever discovered, done so while Jean Richaud was observing a comet in 1689 (Kameswara 1984).

Proxima Centauri b orbits much closer to its host than Earth does to the Sun ($\sim$ 0.05 AU), however, it is still in the habitable zone because the red dwarf star emits less intense radiation. A consequence of the proximity of Proxima b's orbit is that it may be tidally locked, in which the same side of the planet faces the star throughout its orbit (Witze 2016). This would result in extreme temperature changes between the dayside and the nightside. Therefore, it is possible that life could only exist along the terminator. A mission to directly image the planet and resolve structures on the surface would be an incredible feat and very useful for understanding more about the conditions of the planet. This is part of the goal of *Breakthrough Starshot*!

The *Breakthrough Starshot Initiative* is currently working towards obtaining these in situ measurements of the α Centauri system. It could be the first truly interstellar mission! The contents of this chapter hope to elaborate on the interstellar environment through which the mission's spacecrafts must travel. We will explore elemental compositions, temperature, turbulence, historical changes, dust grain composition, and dust grain size distributions.

3.2 Observations

Due to α Centauri being such a popular target for observing runs, we have bountiful high resolution near-UV spectra from the *Hubble Space Telescope*. With a combination of spectra from both GHRS and STIS, we can look for changes in the local interstellar medium between 1992 and 2015. Challenges of comparing spectra arise because spectrographs are sensitive instruments, so there are various calibrations that are necessary to appropriately analyze changes in the ISM. The first thing we can do is to overlay the spectra on each other to see morphological changes and shifts in the radial velocity of the absorption feature. We look at magnesium features only because they are heavily observed, unsaturated, and have high signal to noise. A flux calibration and a wavelength adjustment for the peak wavelengths and stellar orbits is necessary to compare ISM absorption features in the α Centauri system. The primary spectra is the most recent one from the ASTRAL project taken by STIS in May of 2015. The rest of the spectra

Table 3.1: Historical Observations of α Cen A and B

HD No.	Other Name	Instrument	Grating	Spectral Range (Å)	Resolution ($\lambda/\delta\lambda$)	Exp. Time (s)	PI Name	Program ID	Date
128621...	α Cen B	STIS	E140M	1140-1709	45800	4275	Ayres	Current	2015 May 21
...		STIS	E230H	2724-2995	114000	750	Ayres	13938	2015 Aug 12
...		STIS	E230H	2574-2846	114000	750	Ayres	13938	2015 Aug 12
...		STIS	E140H	1388-1590	114000	1500	Ayres	13938	2015 Aug 12
...		STIS	E140H	1206-1408	114000	1500	Ayres	13938	2015 Aug 12
...		STIS	E140H	1206-1408	114000	1500	Ayres	11839	2015 Jan 7
...		STIS	E140H	1388-1590	114000	1500	Ayres	11839	2015 Jan 7
...		STIS	E230H	2724-2995	114000	750	Ayres	13938	2015 Jan 7
...		STIS	E140M	1140-1735	45800	4275	Ayres	13465	2014 Jul 24
...		STIS	E140M	1140-1735	45800	4950	Ayres	12374	2011 Feb 9
...		STIS	E230H	2324-2596	114000	1296	Ayres	11839	2010 Jul 1
...		STIS	E230H	2574-2846	114000	884	Ayres	11839	2010 Jul 1
...		STIS	E230H	2374-2646	114000	1500	Ayres	11839	2010 Jan 24
...		STIS	E230H	2624-2895	114000	850	Ayres	11839	2010 Jan 24
...		HRS	ECH-B	2792.596-2807.528	100000	707.2	Linsky	5712	1996 May 5
...		HRS	ECH-B	1212.145-1218.783	100000	3264	Linsky	5712	1995 May 5
...		HRS	ECH-B	2792.611-2807.541	100000	1088	Linsky	3943	1993 Apr 29
...		HRS	ECH-B	2593.572-2606.155	100000	979.2	Linsky	3943	1993 Apr 29
128620...	α Cen A	STIS	E140H	1150-1685	114000	3×4695	Ayres	Current	2015 May 21
...		STIS	E230H	2662-2885	114000	3100	Ayres	Current	2015 May 21
...		STIS	E230H	2674-2945	114000	500	Linsky	13938	2015 Aug 12
...		STIS	E230H	2674-2945	114000	500	Linsky	13938	2015 Jan 7
...		STIS	E140M	1140-1735	45800	13465	Ayres	13465	2014 Feb 12
...		STIS	E230H	2624-2895	114000	3100	Linsky	7263	2000 Apr 10
...		STIS	E230H	2374-2646	114000	4900	Linsky	7263	2000 Apr 10
...		STIS	E230H	2124-2396	114000	3500	Linsky	7263	1999 Apr 10
...		STIS	E230H	1874-2146	114000	2000	Linsky	7263	1999 Apr 9
...		STIS	E140H	1497-1699	114000	4695.195	Linsky	7263	1999 Feb 12
...		STIS	E140H	1315-1517	114000	4695.2	Linsky	7263	1999 Feb 12
...		STIS	E140H	1140-1335	114000	4695.2	Linsky	7263	1999 Feb 12
...		HRS	ECH-B	2792.601-2807.538	100000	489.6	Linsky	5712	1995 May 1
...		HRS	ECH-B	2593.556-2606.144	100000	652.8	Linsky	5712	1995 May 1
...		HRS	ECH-B	1212.141-1218.779	100000	2814.2	Linsky	5712	1995 Mar 1
...		HRS	ECH-B	2792.632-2807.560	100000	761.6	Linsky	3943	1993 Mar 1
...		HRS	ECH-B	2593.582-2606.163	100000	652.8	Linsky	3943	1993 Mar 1
...		HRS	ECH-B	2574.692-2587.982	100000	1996.8	Lallement	2461	1992 Aug 14
...		HRS	ECH-B	2590.094-2603.089	100000	1996.8	Lallement	2461	1992 Aug 14
...		HRS	ECH-B	2797.574-2812.825	100000	1996.8	Lallement	2461	1992 Aug 14

can be downloaded from the Mikulski Archive for Space Telescopes (MAST).[1] The specifications for each observation are elaborated in Table 3.1.

3.3 Historical Analysis

3.3.1 Flux Calibration

As said before, spectrographs are fickle beasties and, therefore, we see a wide range of peak fluxes across multiple spectra. Over short timescales, the flux should not vary for these main sequence stars and, therefore it is a very safe assumption that the peaks should be equal. The stellar variability is discussed further in Ayres

[1] *https://archive.stsci.edu/*

Table 3.2: Historical measurements of ISM absorption features for α Centauri A & B

HD No.	Other Name	Ion	Component No.	v (km s^{-1})	b (km s^{-1})	log N_{ion} log cm^{-2}	Reference
128621.....	α Cen B	D I	1	-18.2 ± 0.1	6.88 ± 0.17	12.775 ± 0.009	1
		Mg II	1	-18.1 ± 0.1	2.34 ± 0.21	12.73 ± 0.11	1
		Fe II	1	-17.77 ± 0.44	2.17 ± 0.69	12.50 ± 0.13	10
128620.....	α Cen A	D I	1	-18.2 ± 0.1	6.55 ± 0.27	12.799 ± 0.015	1
		C II	1	-18.70 ± 0.11	2.93 ± 0.15	14.30 ± 0.12	6
		N I	1	-19.58 ± 0.64	3.44 ± 1.17	13.89 ± 0.20	6
		O I	1	-18.63 ± 0.03	2.64 ± 0.19	14.43 ± 0.12	6
		Mg II	1	-18.0 ± 0.2	2.27 ± 0.08	12.74 ± 0.06	1
			1	-17.7 ± 2.5	2.19	12.71	8
			1	-17.8 ± 0.1	2.26 ± 0.02	12.691 ± 0.003	1 of 8
		Si II	1	-17.92 ± 1.28	2.14 ± 0.60	12.83 ± 0.15	6
		Fe II	1	-17.7 ± 0.1	1.78 ± 0.14	12.455 ± 0.022	1
			1	-18.3 ± 1.5	1.34	12.36	8
			1	-18.2 ± 0.1	1.43 ± 0.02	12.441 ± 0.004	1 of 2

Table 3.3: (1) Linsky & Wood (1996); (2) Bertin et al. (1995); (3) Linsky et al. (1995); (4) Dring et al. (1997); (5) Piskunov et al. (1997); (6) Redfield & Linsky (2004a); (7)Hébrard et al. (1999); (8) Lallement et al. (1995); (9)Lallement et al. (1994); (10) Redfield & Linsky (2002)

(2010). This allows us to take the flux and multiply it by a constant such that the peaks for all spectra are equal. In some cases, observations with low signal to noise make this process more complicated, as can be seen in the April 1993 spectra in Figures 3.3 or 3.5.

3.3.2 Wavelength Calibration

Over the course of twenty years and different spectrographs, it is no wonder that there are changes in the wavelength calibration. If there were no interstellar absorption we would be able to see the peak of stellar emission clearly and calibrate easily. However, the peak of the stellar emission is not visible due to the ISM absorption cutting right through it. In order to find the peak stellar emission, we use a bisector method to analyze the stellar line on either side of the absorption feature. We take an average $x-$position of a point from the left and one from the right that are at the same flux. The resulting vertical line from the bisector method can be seen in Figure 3.1. In an ideal world, this would result in a perfectly vertical line that would line up with where the peak would be in the absence of absorption, assuming symmetric stellar emission. By performing this for both magnesium lines and all spectra, we can center each of the profiles on the position of the most recent data from May 2015. It was useful to plot the centroid for each spectra against the corresponding profile for each spectra to verify that it is accurate. This centroid is shown in contrast with the prediction of the radial velocities for both stars in the binary from Pourbaix et al. (2002), where peak emission is at the same wavelength before adjusting for the change in the stellar radial velocities as the two stars orbit one another. After doing this, we see that while the centroids of the stellar emission line up, the LISM absorption does not (Figure 3.2). This is because we have not yet adjusted for those changes in the radial velocity caused by the binary orbits. The binary system has a period of P = 79.90 years, therefore over the course of $\sim$ 23 years, there will be a noticeable change in the radial velocity of each star as it moves towards and away from us. Using the model for the system from Pourbaix et al. (2002), we can adjust the profile such that the peak emission centered together in the first wavelength calibration are adjusted for the change in radial velocity of the two stars as they sweep around their orbits.

From here, we can look at the effect centering the stellar emission has on the absorption profile, shown in Figure 3.3.

After adjusting the centroids to the correct radial velocities from Pourbaix et al. (2002) in Figure 3.4, we get a finalized profile in Figure 3.5. Where we see offsets that are due to changes in the radial velocities of the two stars orbiting one another.

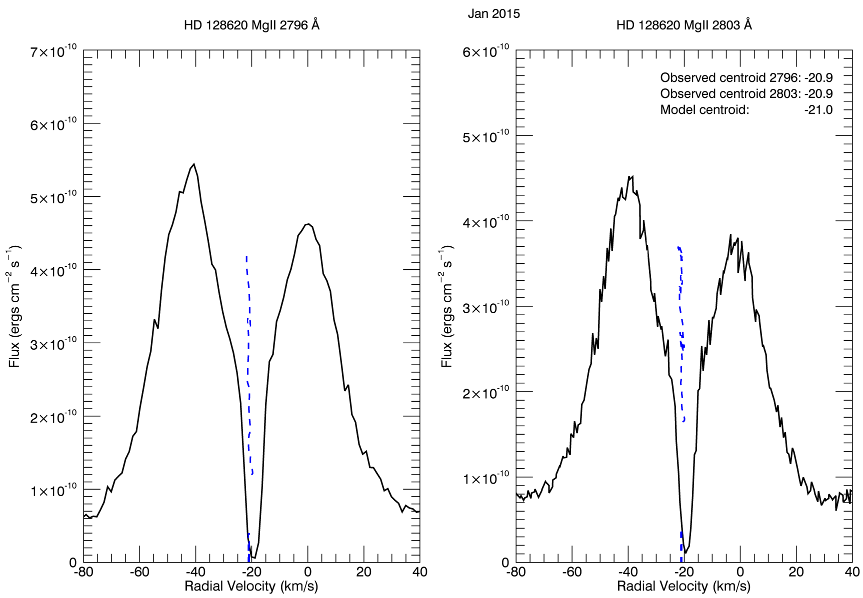

Figure 3.1: Magnesium profiles of α Centauri A from observations taken in January 2015 in observing program 13938. The longer dashed blue line is the predicted peak emission from the bisector method and the Pourbaix et al. (2002) model is the short dashed blue line at the bottom of each plot. This shows that there was very little wavelength calibration needed for this spectra.

3.3.3 Final Profiles

The result of these three calibrations shows that the radial velocity of the cloud between us and α Centauri, the G cloud, does not change substantially, see Figure 3.5. However, it appears likely that there are certain morphological changes in the line profile. The spectra taken by GHRS in August of 1992 is significantly shallower than the other profiles. This is most easily seen by creating continua for each line and taking a residual by subtracting the continuum by the flux. This results in seeing the absorption as if it were in emission, see Figure 3.6. The variation in depths can be attributed to a number of issues.

In order to get a good estimate of width and depth changes over time, it is necessary to actually go through and fit each magnesium line for all stars.

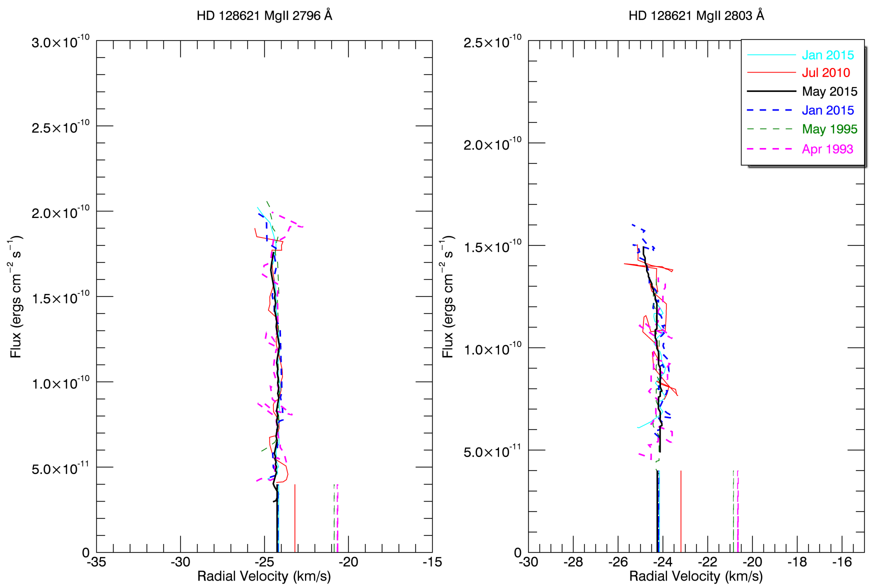

Figure 3.2: The peaks of stellar emission are forced to the same velocity before they are adjusted to the correct radial velocities shown in Pourbaix et al. (2002).

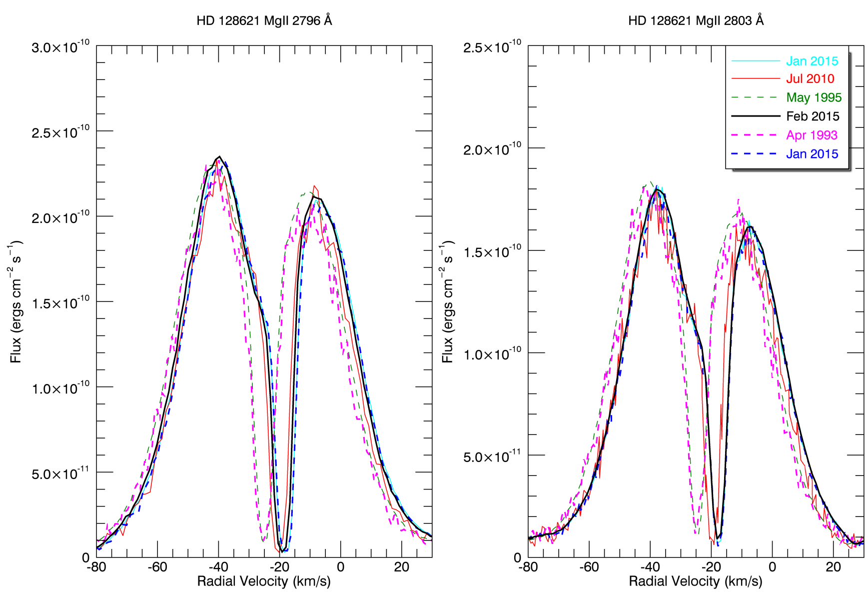

Figure 3.3: Historical spectra for HD128621 before adjusting for radial velocity changes of the star.

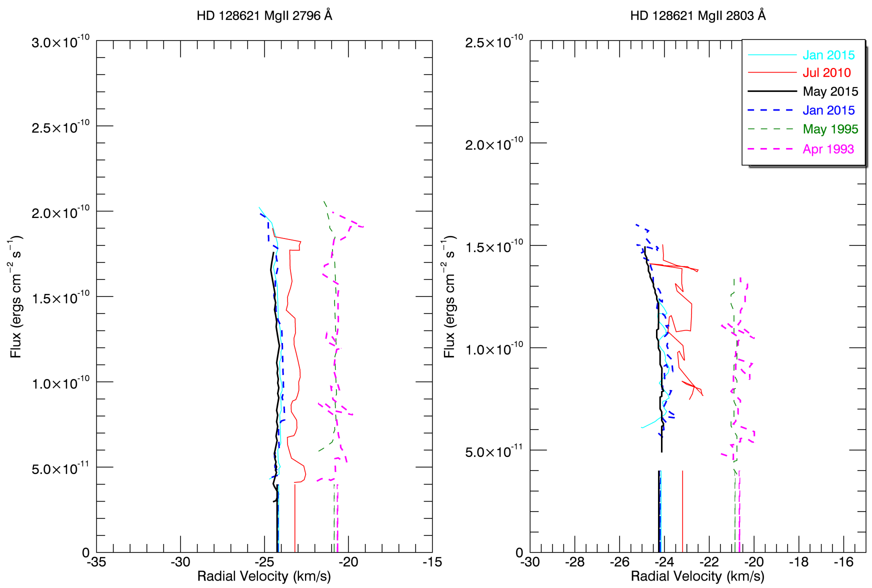

Figure 3.4: Centroid lines verified through individual profiles like in Figure 3.1. The vertical lines along the bottom represent the expected radial velocities for each centroid from Pourbaix et al. (2002). This is the final wavelength adjustment that results in overlapping absorption features seen in Figure 3.5.

This serves as an important check on how our procedure for fitting interstellar absorption compares with older ones written by Lallement et al. (1994) or Linsky & Wood (1996), seen in Figure 3.7.

There are very few inconsistencies between the results we measured and previous measurements. Therefore, we cannot conclusively make any assumptions about the changing nature of the LISM over the course of the last twenty five years. We next decided to take the old spectra and take our own measurements to verify that our fitting routines produced the same results. We performed fits on the singly ionized magnesium line because it is generally unsaturated and consistently has a high resolution the results of our fits to this data can be seen in Table 3.4.

By fitting each of these model spectra we can negate issues in comparing the

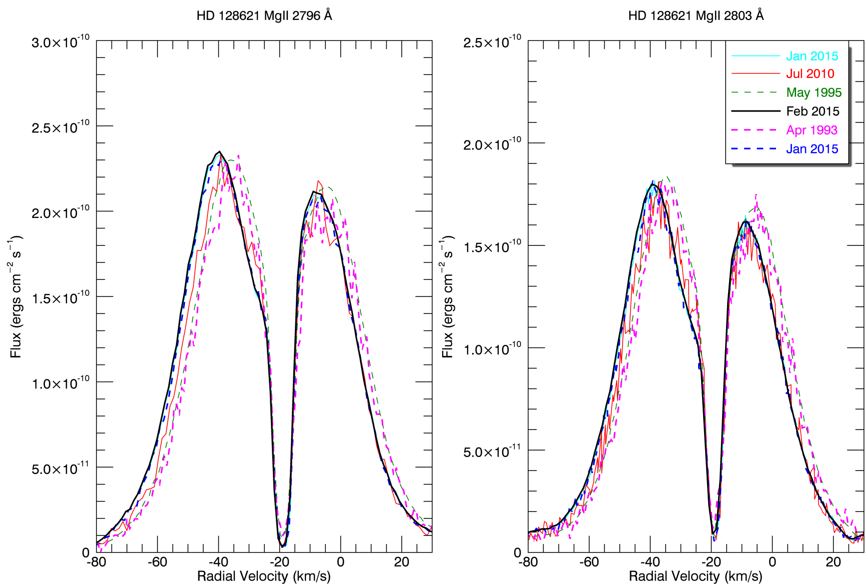

Figure 3.5: Finalized positions of archived spectra showing how the absorption feature remains fairly constant. This shows how the radial velocity of the cloud has not been changing noticeably over the last twenty years.

spectra because they are convolved with the corresponding line spread functions and have their own continua. It is clear that from Figure 3.7 that all of the changes are well within their errors.

3.4 Fits for α Centauri A & B

In this section, we show our fits for both stars for various transitions in the ultraviolet region of the electromagnetic spectrum. α Centauri A has high resolution data for both the far and near UV. As visible in Figure 3.8, the signal to noise ratio is much lower at N I ($SNR \sim 3.3$) than at Mg II ($SNR \sim 19.6$). This results in more uncertainty in our fits parameters as shown in Table 3.5. The same problem occurred at iron in which the component is barely visible in the Fe II (2587 Å) profile. For this fit, we used only the simultaneous fit because it is

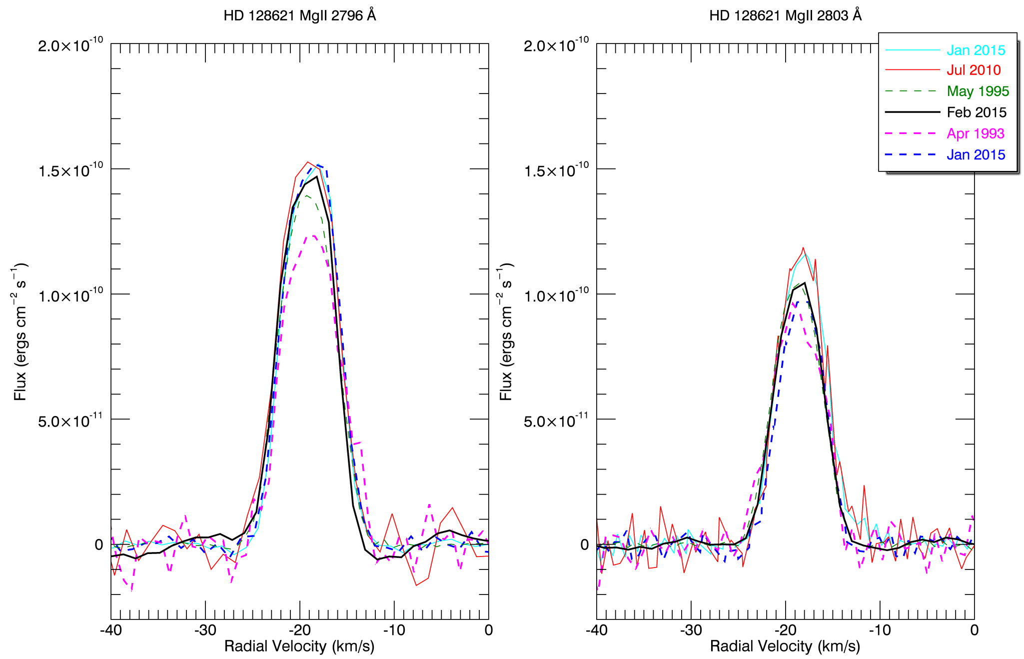

Figure 3.6: The absorption features for HD128621 subtracted by their corresponding continuums made with *mkfb.pro*.

fixed with the more pronounced Fe II (2600 Å) line, which has a larger oscillator strength.

α Centauri B had only high resolution data for the near-UV. This results in less accurate fits in the far-UV due to having less information.

The parameters given by these fits are presented in Table 3.5, the fits with asymmetric column densities are from a weighted mean based on the associated errors for individual and simultaneous fits.

3.5 Electron Density

Electron densities in the interstellar environment can be inferred through ratios of ground level ion transitions and their excited counterpart. In the past, this has been performed using N (Mg II)/N (Mg I), however this requires ionization

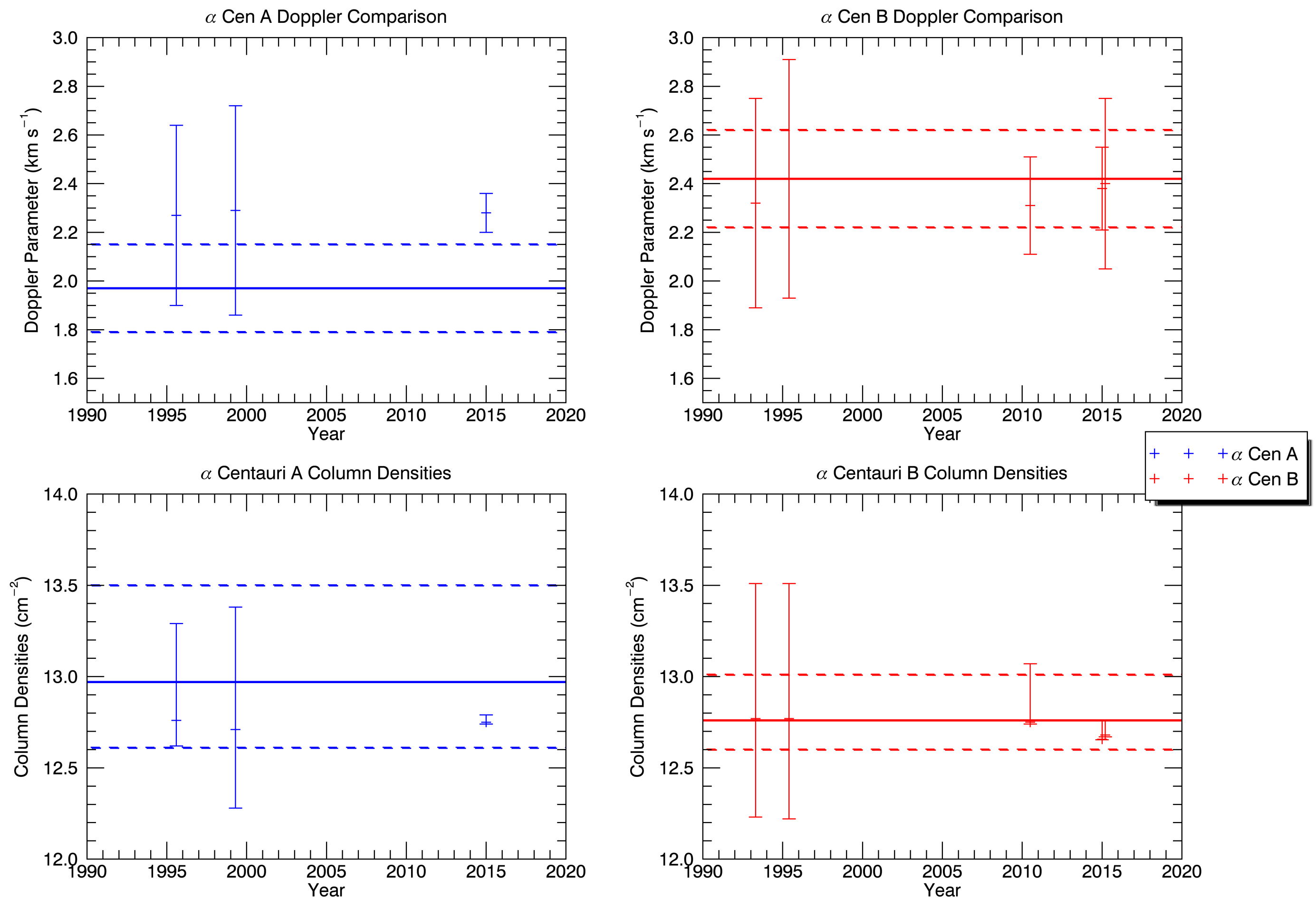

Figure 3.7: Comparison between the Doppler parameters and column densities for both stars from values in Table 3.2. The solid line is the value we found in our sample with the dashed lines being the upper and lower limits.

HD Number	Year	Ion	v (km s^{-1})	b (km s^{-1})	log N (cm^{-2})
128621.....	May 2015	Mg II	-17.89 ± 0.28	1.97 ± 0.18	$12.97^{+0.53}_{-0.36}$
	Jan 2015	Mg II	-18.85 ± 0.07	2.32 ± 0.43	$12.77^{+0.54}_{-0.74}$
	Jan 2015 2	Mg II	-18.77 ± 0.02	2.42 ± 0.49	$12.77^{+0.55}_{-0.74}$
	Jul 2010	Mg II	-18.88 ± 0.06	2.31 ± 0.20	$12.75^{+0.01}_{-0.32}$
	May 1995	Mg II	-18.87 ± 0.08	2.38 ± 0.17	$12.657^{+0.003}_{-0.102}$
	Apr 1993	Mg II	-18.90 ± 0.04	2.40 ± 0.35	$12.68^{+0.01}_{-0.08}$
128620.....	May 2015	Mg II	-17.91 ± 0.064	2.42 ± 0.20	$12.76^{+0.25}_{-0.16}$
	Jan 2015	Mg II	-18.09 ± 0.06	2.27 ± 0.37	$12.76^{+0.14}_{-0.53}$
	Apr 1999	Mg II	-18.55 ± 0.21	2.29 ± 0.43	$12.71^{+0.43}_{-0.67}$
	May 1995	Mg II	-19.77 ± 0.82	2.28 ± 0.08	$12.75^{+0.01}_{-0.04}$

Table 3.4: Magnesium fit results for all spectra available taken with STIS or GHRS

HD Number	Year	Ion	v (km s^{-1})	b (km s^{-1})	$\log N$ (cm^{-2})
128621.....	May 2015	D I	-16.896 ± 0.030	6.548 ± 0.053	12.9087 ± 0.0016
		C II	-18.178 ± 0.036	3.349 ± 0.102	13.942 ± 0.043
		C II*	-18.200 ± 0.037	3.430 ± 0.090	12.460 ± 0.011
		N I	-20.640 ± 1.019	4.11 ± 1.92	$13.28^{+0.16}_{-0.11}$
		O I	-19.802 ± 0.044	3.881 ± 0.088	14.344 ± 0.019
		Mg II	-17.89 ± 0.28	1.97 ± 0.18	$12.97^{+0.53}_{-0.36}$
		Si II	-19.22 ± 0.71	2.33 ± 0.86	$12.67^{+0.26}_{-0.16}$
		Fe II	-17.68 ± 0.41	1.86 ± 0.34	$12.55^{+1.45}_{-0.29}$
128620.....	May 2015	D I	-18.80 ± 0.04	6.446 ± 0.062	12.9907 ± 0.0032
		C II	-20.226 ± 0.041	3.337 ± 0.07	14.074 ± 0.032
		C II*	-20.200 ± 0.036	3.338 ± 0.074	12.058 ± 0.057
		N I	-20.79 ± 0.68	6.18 ± 0.76	$13.71^{+0.40}_{-0.21}$
		O I	-19.233 ± 0.057	1.75 ± 0.28	15.67 ± 0.40
		Mg II	-17.913 ± 0.064	2.42 ± 0.20	$12.76^{+0.25}_{-0.16}$
		Si II	-19.51 ± 0.75	1.98 ± 0.61	$12.82^{+0.26}_{-0.16}$
		Fe II	-18.19 ± 0.11	1.75 ± 0.22	$12.505^{+0.077}_{-0.066}$

Table 3.5: Fit results for multiple ions of the most recent spectra in the ASTRAL project taken on *HST* with STIS in May of 2015.

equilibrium and is heavily dependent on temperature (Redfield & Falcon 2008). Collisionally excited carbon (C II*), on the other hand, compared with the C II resonance line column density allows us to measure the number density of electrons (n_e) in the environment. The collisionally excited carbon line is actually

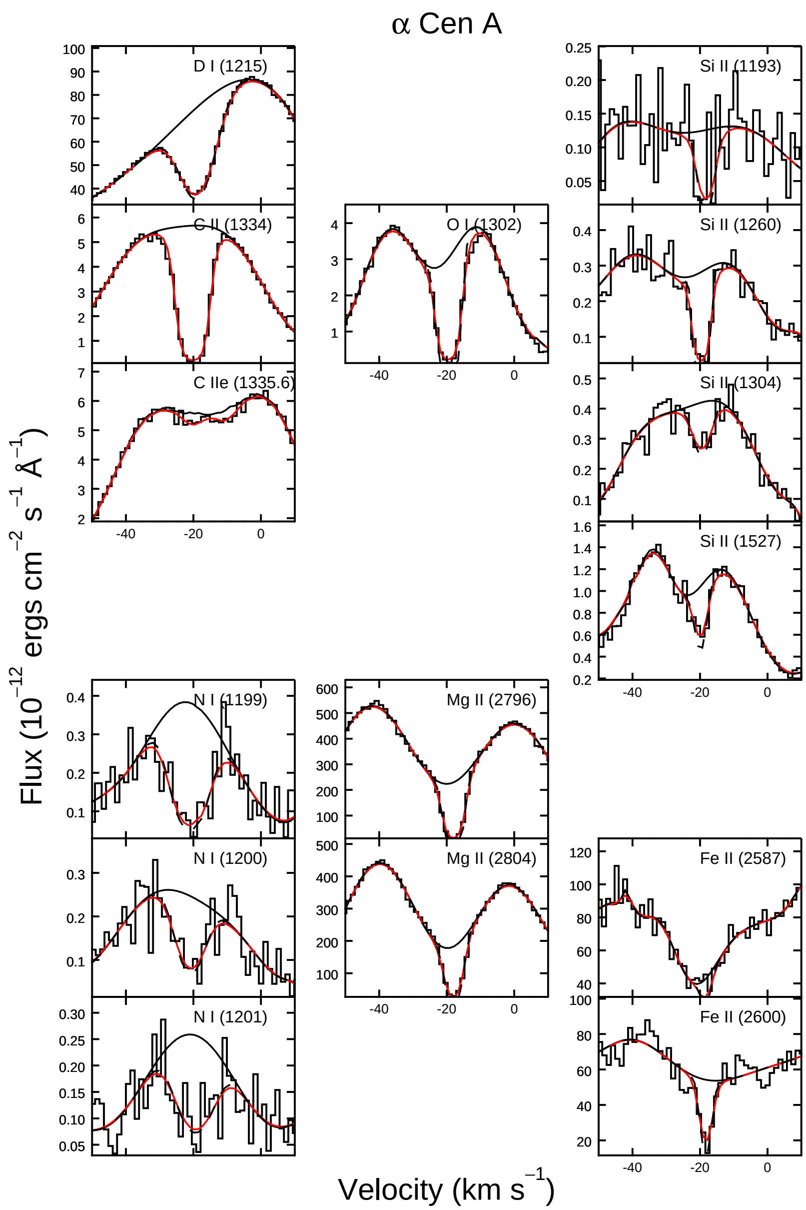

Figure 3.8: Individual and simultaneous fits for α Centauri A. The black histogram line is the data, which shows varying signal to noise ratios across the spectrum. The thick red line is the fit; the thin black line is the reconstructed continuum. The C II* absorption feature is actually a doublet with individual peaks with 0.4 Å of each other.

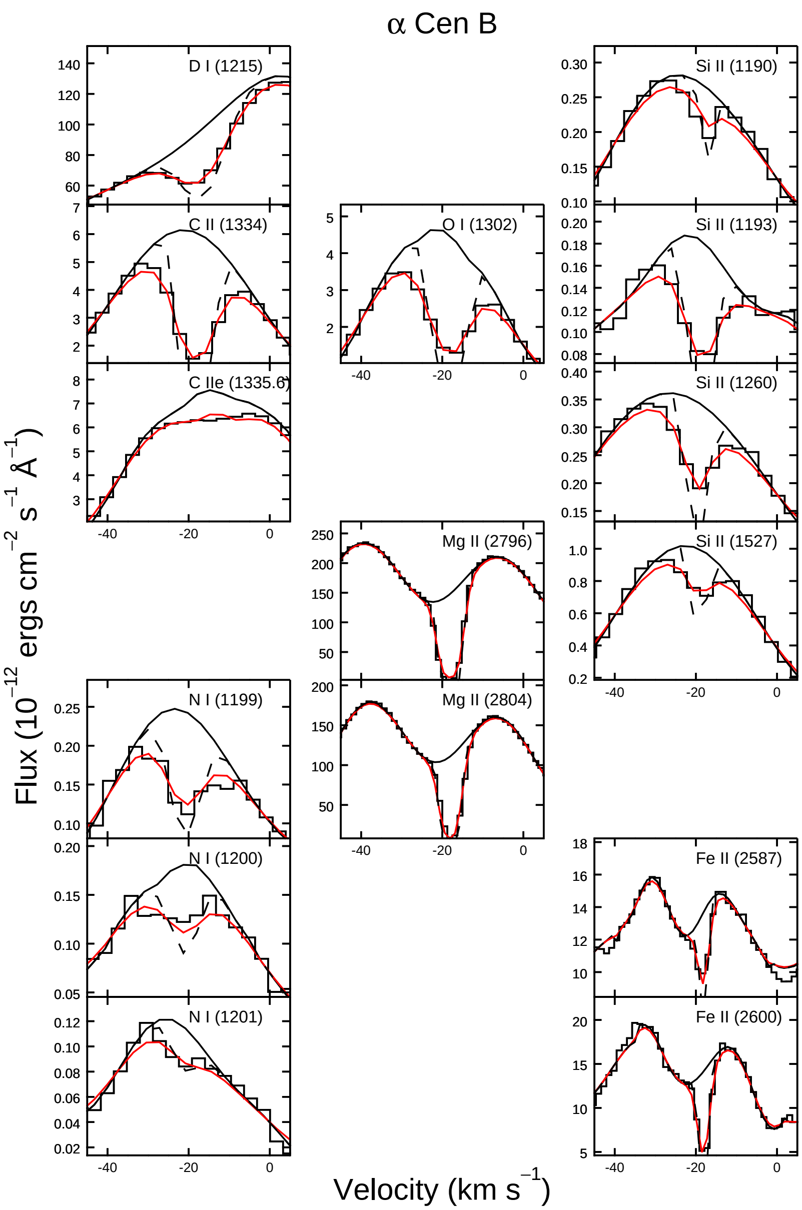

Figure 3.9: Combined fits for α Centauri B. Description same as Figure 3.8.

a doublet at 1335.66 Å and 1335.70 Å. These two lines can be treated as two components of a single line by incorporating the appropriate central wavelengths,

HD Number	Ion	v (km s^{-1})	b (km s^{-1})	log N(cm^{-2})	n_e (cm^{-3})
128620.....	C II	-20.213 ± 0.036	3.338 ± 0.074	14.070 ± 0.033	$0.156^{+0.036}_{-0.029}$
	C II* (1335.66 Å)	-20.200 ± 0.036	3.338 ± 0.074	12.058 ± 0.057	
	C II* (1335.70 Å)	-20.200 ± 0.036	3.338 ± 0.074	12.058 ± 0.057	
128621.....	C II	-18.211 ± 0.037	3.430 ± 0.090	13.912 ± 0.032	$0.565^{+0.059}_{-0.053}$
	C II* (1335.66 Å)	-18.200 ± 0.037	3.430 ± 0.090	12.46 ± 0.011	
	C II* (1335.70 Å)	-18.200 ± 0.037	3.430 ± 0.090	12.46 ± 0.011	

Table 3.6: Fits for carbon lines for both α Centauri stars with the calculated electron densities from Equation 3.1.

gamma coefficients, and oscillator strengths. By taking a simultaneous fit, where we fix the central velocities and the Doppler parameters, but allow the column density to vary between the resonance line and the excited state, we can obtain the electron densities for both lines of sight. The results are shown in Table 3.6 and in Figures 3.8 and 3.9. The following equation allows us to solve for the electron density for each line of sight,

$$\frac{N(\text{C II}^*)}{N(\text{C II})} = \frac{n_e C_{12}(T)}{A_{21}}, \tag{3.1}$$

where $N(\text{C II})$ and $N(\text{C II}^*)$ are the column densities for each line. A_{21}, the radiative de-excitation rate coefficient is $A_{21} = 2.29 \times 10^{-6}$ s^{-1} from Nussbaumer & Storey (1981). The collision rate coefficient can be expressed in cgs units as,

$$C_{12}(T) = \frac{8.63e-6\Omega_{12}}{g_1 T^{0.5}} \exp -\frac{E_{12}}{kT}. \tag{3.2}$$

The values for the electron density are surprisingly different between the two lines of sight. A typical value for the LISM found by Redfield & Falcon (2008) toward the LIC cloud is$n_e = 0.12 \pm 0.04$ cm^{-3}, an average of multiple traversing lines of sight. However, for α Centauri, it is the G cloud we care about. The difference could be due to the inferred C II* absorption seen in Figure 3.9, this is in contrast from the clearer absorption features in Figure 3.8.

3.6 Dust Composition

Interstellar dust can be studied by assuming that the giant molecular cloud that formed our Sun, had a uniform composition similar to the abundances observed in the Sun. However, this is not what we observe; the interstellar medium has depletions for most elements. These depletions are attributed to the condensation of gas into dust grains. The condensation temperature is the point at which a gas becomes a solid, therefore the lower the condensation temperature the less likely the dust grain will exist in the interstellar environment, which in this region is still warm from the radiation of a recent supernova (Galeazzi et al. 2014).

In order to calculate depletion, we analyze the column densities, calculated in Section 2.6, for multiple ions along each line of sight. Solar abundances are taken from Asplund et al. (2005) and hydrogen column densities are from Wood et al. (2004). Using the following equation we can solve for the depletions of various ions along many lines of sight,

$$\left[\frac{X_{gas}}{H}\right] = \log\left(\frac{N(x)}{N(H)}\right) - \log\left(\frac{X}{H}\right)_{\odot}. \tag{3.3}$$

This is the conceptual version from Jenkins (2009), which applies to diffuse interstellar environments like the LISM. He also extends this model to deal with dense star-forming regions by adding two components A_X and F_*, which are the propensity of the element to increase its particular depletion level and the line of sight depletion factor. This equation results in a depletion in log space for the gas ratio of elements to hydrogen. Plotting condensation temperature against depletion for each line of sight and various ions results in evidence for a larger depletion for higher condensation temperatures. (Figure 3.10)

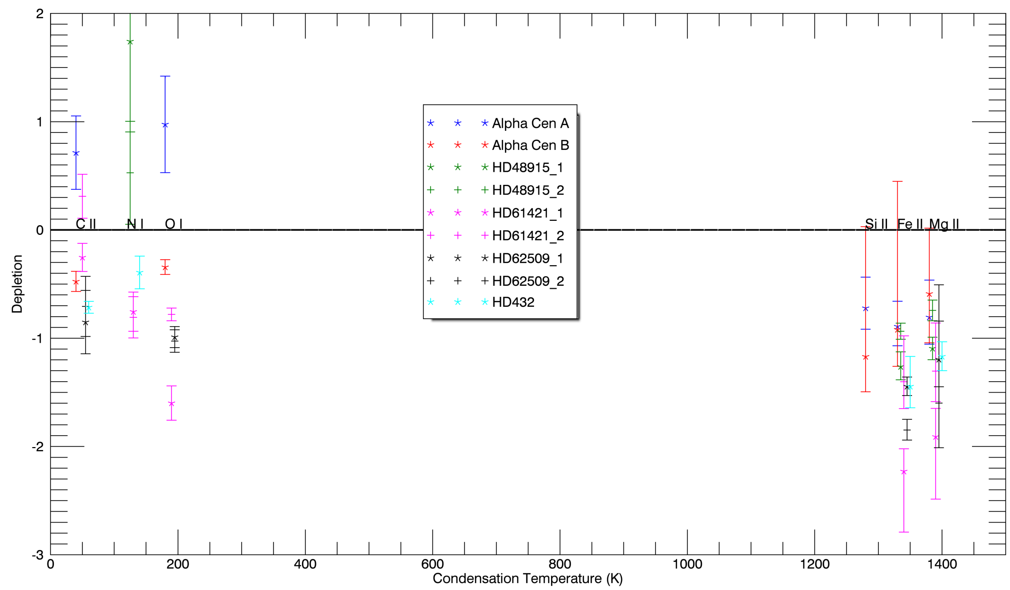

Figure 3.10: Condensation temperature for various elements plotted against the measured depletions. Condensation temperatures taken from Ebel (2000). The associated error bars are due to error in Asplund et al. (2005) values and column density errors. The horizontal line shows where the observed column density is equal to solar abundances.

Using these depletions, we can estimate the amount of dust shown in Equation 3.4,

$$\left(\frac{X_{dust}}{H}\right) = \left(\frac{X}{H}\right)_{\odot} \left(1 - 10^{\left[\frac{X_{gas}}{H}\right]}\right). \tag{3.4}$$

By looking at the ratio of magnesium and iron to silicon in the interstellar environment, we can get a handle on the composition of the dust grains as shown in Figure 3.11.

From this graph, we see that the lines of sight we are looking at are more ionized than we would have expected for the local interstellar medium. This is based on the ratio of the column densities of singly ionized magnesium to singly ionized iron. The bottom portion of the plot show that the interstellar material

HD Number	Ion	Depletion (dex)	Dust (cm^{-2})
128620.....	CII	$-0.347^{+0.082}_{-0.082}$	$14.16^{+0.11}_{-0.13}$
	OI	$+0.98^{+0.45}_{-0.45}$	$0.0^{+0.0}_{-0.0}$
	MgII	$-0.80^{+0.34}_{-0.25}$	$13.49^{+0.12}_{-0.20}$
	SiII	$-0.72^{+0.30}_{-0.20}$	$13.449^{+0.076}_{-0.16}$
	FeII	$-0.98^{+0.13}_{-0.12}$	$13.433^{+0.062}_{-0.068}$
128621.....	C II	$-0.475^{+0.093}_{-0.093}$	$14.240^{+0.090}_{-0.106}$
	O I	$-0.343^{+0.069}_{-0.069}$	$14.42^{+0.10}_{-0.12}$
	Mg II	$-0.58^{+0.62}_{-0.45}$	$13.43^{+0.18}_{-nan}$
	Si II	$-0.86^{+0.30}_{-0.20}$	$13.473^{+0.065}_{-0.116}$
	Fe II	$-0.93^{+1.50}_{-0.34}$	$13.422^{+0.081}_{-0.0}$

Table 3.7: Depletion values for both α Centauri stars. The 0's are caused by having an overabundance compared with solar values.

is generally of an olivine composition, which is a confirmation of the current prediction (Draine 2011) (Frisch et al. 2011).

3.7 Dust Grain Size

The extinction of stars was first noticed by Barnard in 1907 and confirmed by Trumpler (1930) who showed that there was a dimming of distant stars in addition to the inverse square law. He did this using the "pair method", in which he compared the spectra of an extincted star with another nearby star of similar spectral class. Extinction occurs because grains in interstellar space absorb and scatter light corresponding to the cross-sectional area of the dust grain. This results in a wavelength dependent extinction curve which increases at shorter wavelengths. Hidden in extinction curves are a couple of spectral features purely made by dust such as the 2175 Å feature from polynuclear aromatic hydrocarbons (PAH), the C-H feature at 3.4μm, and the silicate feature at 10μm. Dust can also be observed in the wavelength-dependent polarization of light from reddened stars

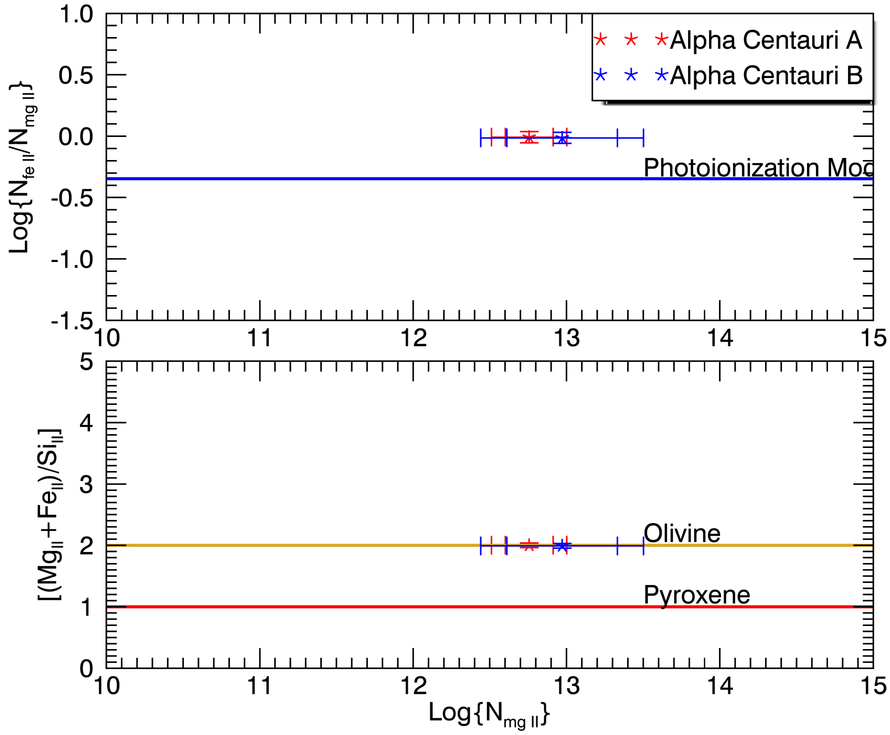

Figure 3.11: The top portion of the graph shows the prediction for this ratio from photoionization models from Slavin & Frisch (2002). The bottom graph shows the observed ratio of dust along each line of sight for the two main stars in α Centauri. The two lines distinguish olivine and pyroxene silicates.

(Draine 2011). Because there are no closer stars than those in the α Centauri system, we attempted to produce an extinction curve using a model spectra for each star from UV Blue created in Rodríguez-Merino et al. (2005a). We took the spectra of the star corresponding to the metallicity, effective temperature, and surface gravity of each star. Calculating extinction was done using the following equation,

$$\frac{A_\lambda}{\mathrm{mag}} = 2.5\log_{10}[F_\lambda^0/F_\lambda], \tag{3.5}$$

where F^0_λ is the star with no extinction, or in our case the model spectra, and F_λ is the α Cen star.

Using this, we looked to see if we could observe the characteristic bump at 2175 Å along either line of sight which is caused by polynuclear aromatic hydrocarbon (PAH) molecules. In Figure 3.12, we find no conclusive evidence of any bump for either star likely because these stars are too close. The α Centauri stars are generally used as the unextincted stars; it may not be possible to find lines of sight with less extinction.

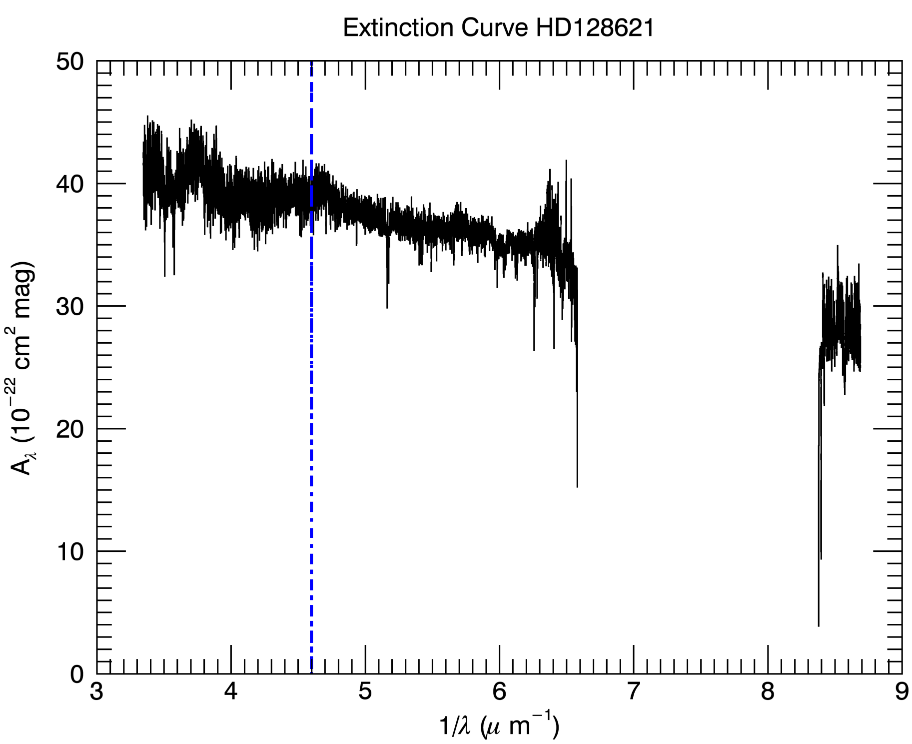

Figure 3.12: An extinction curve for α Centauri B showing no definitive information about aromatic carbon dust grains. The blue line indicates the position at which the bump should peak. The large gap is the area at which the model does not have a prediction for. This does not show the typical galactic trend seen in Figure 3.13.

While, this extinction curve clearly does not have a bump at 2175 Å, it also does not even have the general trend that it should. Model extinction curves, like in Figure 3.13, which use equations from Cardelli et al. (1989), show that there should be more extinction at shorter wavelengths. This is because interstellar dust grains are generally very small, which absorb or scatter light that is proportional to the cross sectional area of the particle. This well known galactic trend is not reflected in the extinction curve, which means that something is likely wrong in the model or with our scaling function. We attempted to solve this by getting a higher resolution spectra from Rodríguez-Merino et al. (2005b) and broadening it to the STIS high resolution $R \equiv \lambda/\Delta\lambda = 114000$. However, no matter our scaling factor, we could not get an extinction curve with the correct trend. This is likely because the model is not accurate enough at shorter UV wavelengths because of its complexity and lack of continuum in this region. An option would be to get a spectra from a line of sight with even less extinction than the α Centauri stars and to attempt the pair method again. However, this would be a longshot. Therefore, the best method available to us is to take an interstellar dust size distribution for the diffuse interstellar medium and adjust until we see the correct ratios of elements, as detailed in the following sections.

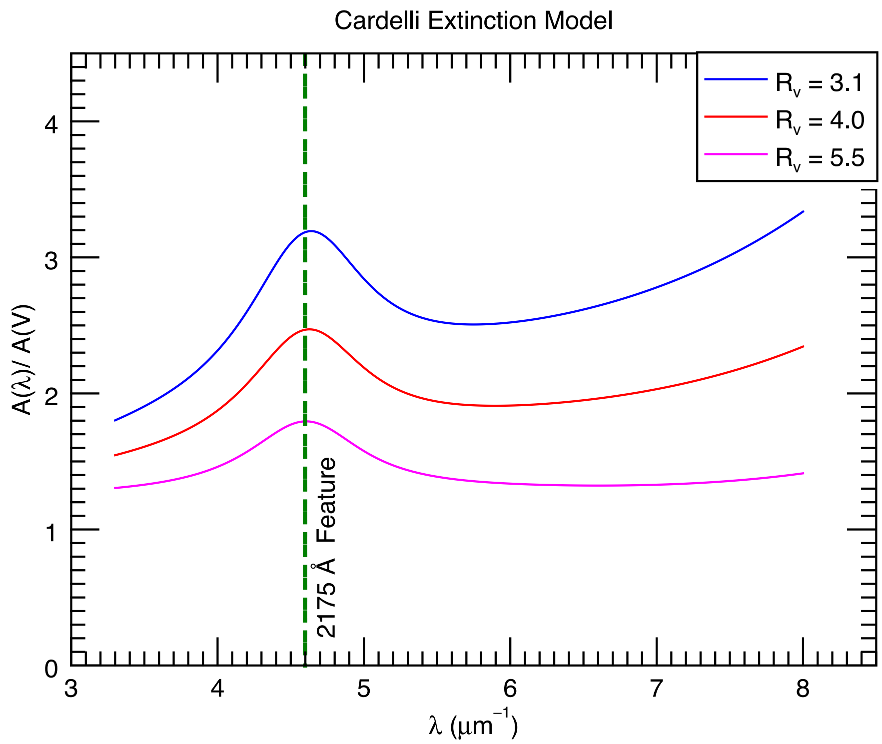

Figure 3.13: Model extinction curves from Cardelli et al. (1989) for $\mathrm{R}_v = 3.1, 4.0, 5.5$ showing how the extinction at the 2175 Å feature relative to the V-band varies.

3.7.1 The Weingartner Dust Model

Weingartner & Draine (2001) model the size distribution for grains in various ISM conditions based on two parameters. The R_v constant, which is the ratio of visual extinction to reddening $R_V = \frac{A(V)}{E(B-V)}$ and b_C which is the carbon abundance of very small grains. With these two values, Weingartner & Draine (2001) recreate values for power law indices α_g and α_s, curvature parameters β_g and β_s, transition sizes $a_{t,g}$ and $a_{t,s}$, upper cutoff parameters $a_{c,g}$ and $a_{c,s}$ (where g and s stand for the graphite and silicate grain compositions). They present various models based on changing R_V values and b_C values. They also have two cases, in which, case B is distinguished from Case A by fixing the grain volumes at the values found for

$R_V = 3.1$; $V_{tot,s} = 3.9 \times 10^{-27}$ cm^3 H^{-1} and $V_{tot,g} = 2.3 \times 10^{-27}$ cm^3 H^{-1}. They create this case to account for their assumption that the extinction in the I band ($N(I)/N_H$) is independent of R_V. They find it unlikely that grains entering an environment with higher density will have part of their grain volume transferred to the gas phase. We, therefore, assume the value of $R_V = 4.0$, $b_C = 4 \times 10^{-5}$, and case B from Weingartner & Draine (2001) for the diffuse interstellar medium. Using this model, we can solve for the number of grains at each radii based on the dust we measured in Section 3.6. There is a significant contribution from very small carbonaceous grains shown in Equation 3.6. This equation is responsible for the PAH 2175 Å extinction bump,

$$\frac{1}{n_H}\left(\frac{dn_{gr}}{da}\right)_{vsg} \equiv D(a) = \sum_{i=1}^{2} \frac{B_i}{a} \exp\left(-\frac{1}{2}\left[\frac{\ln a/a_{0,i}}{\sigma}\right]^2\right), \quad a > 3.5\text{Å} \tag{3.6}$$

$$B_i = \frac{3}{(2\pi)^{3/2}} \frac{\exp -4.5\sigma^2}{\rho a_{0,i}\sigma} \times \frac{b_{C,i} m_C}{1 + \operatorname{erf}[3\sigma/\sqrt{2} + \ln a_{0,i}/3.5\text{Å}]\sigma\sqrt{2}}, \tag{3.7}$$

where a is the grain size, $\sigma = 0.4$, $\rho = 2.24$ g cm^{-3} is the density of graphite, m_C is the mass of a single carbon atom, $b_{C,1} = 0.75 b_C$, $b_{C,2} = 0.25 b_C$, b_C is the total carbon abundance (per H nucleus) in the log-normal populations, $a_{0,1} = 3.5$ Å, $a_{0,2} = 30$ Å. The *vsg* stands for the very small grain population (PAH molecules) that is described by this function.

Coupling this small dust grain population with Equation 3.8, the size distributions of carbonaceous dust grains, we can get probabilities for various sizes (a). From Li & Draine (2001) we assume a graphitic molecule composition for grains larger than 50 Å and the polycyclic aromatic hydrocarbon (PAH) grain composition for grains smaller than this threshold. In order to constrain dust along the line of sight, we apply depletion measurements to this until the amounts we see match the model.

$$\frac{1}{n_H}\left(\frac{dn_{gr}}{da}\right) = D(a) + \frac{C_g}{a}\left(\frac{a}{a_{t,g}}\right)^{\alpha_g} F(a;\beta_g, a_{t,g}) \times \begin{cases} 1, & 3.5\text{Å} < a < a_{t,g} \\ \exp -[(a-a_{t,g})/a_{c,g}]^3, & a > a_{t,g} \end{cases} \tag{3.8}$$

The equation $D(a)$ for small PAH grains is found in Equation 3.6. The resulting distributions from these equations for $R_v = 4.0$ for Weingartner & Draine (2001)'s case B ,in which, grain volumes are held fixed at the values found for $R_v = 3.1$, as shown in Figure 3.14 and Table 3.8

R_V	$10^5 b_C$	α_g	β_g	$a_{t,g}$ (μm)	$a_{c,g}$ (μm)	C_g	α_s	β_s	$a_{t,s}$	$a_{c,s}$	C_s
4.0	4.0	-1.96	-0.813	0.0693	3.48	2.95×10^{-13}	-2.11	2.10	0.198	0.1	3.13×10^{-14}
Dann Model	4.0	-1.96	-0.813	0.0693	3.48	2.95×10^{-13}	-1	-1	1	0.3	2×10^{-15}

Table 3.8: Parameters used for the Weingartner & Draine (2001) model and the added silicate component accounting for data from Frisch et al. (1999). We used the same carbonaceous distribution for both but added the new silicate model to the original silicate model, shown in Figures 3.15 and 3.16

We first attempted to solve for dust grain size distributions by randomly generating billions of unique particles based on the Weingartner & Draine (2001)

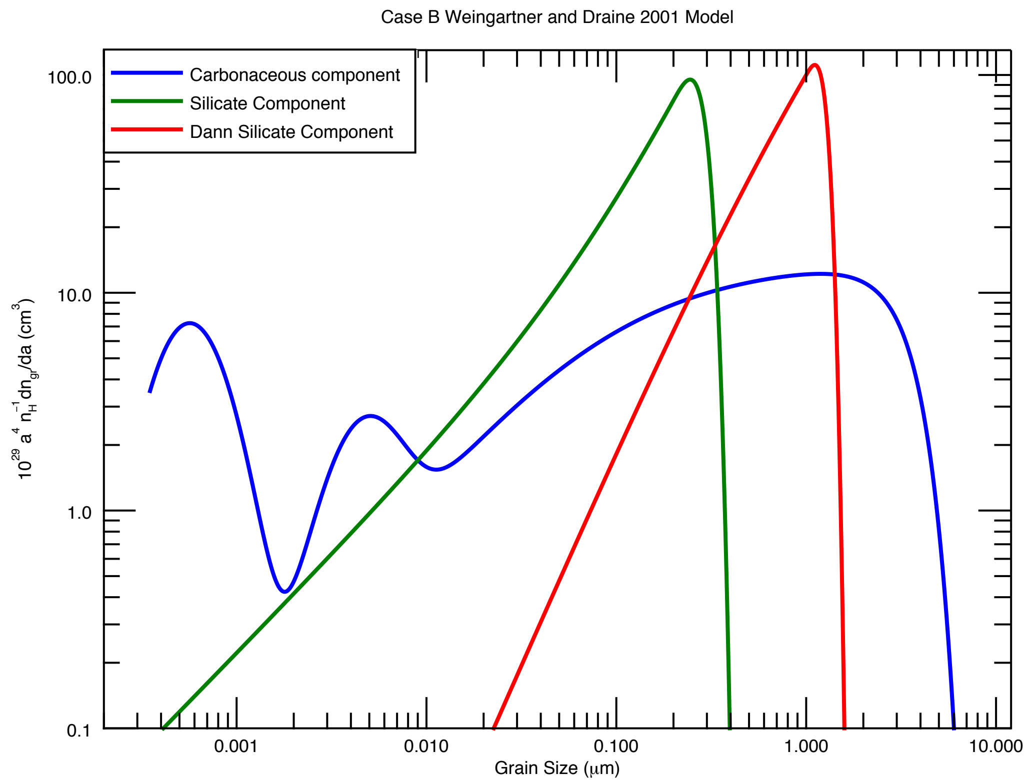

Figure 3.14: Distribution of grain sizes against a function of probability scaled by a^4, which emphasizes the probabilities of large grains. The green line is the silicate distribution from Weingartner & Draine (2001); the blue line is the carbonaceous distribution using PAH and graphitic grains. The red component is an added silicate component to fit Frisch et al. (1999) data shown in Figure 3.16.

probability function. However, this is extremely computationally expensive. Instead we computed it through using the probability density function and scaling it such that C II, Mg II, and Fe II have an identical number of atoms as we observe in the absorption features. From this we can calculate the amount of carbon and oxygen we should be seeing along the line of sight. Carbonaceous grains are much simpler to deal with because they are a mixture of abundant hydrogen and depleted carbon. However, silicate grains in the ISM are generally of olivine composition, whose endmembers are forsterite (Mg_2SiO_4) and fayalite (Fe_2SiO_4)

(Draine 2011). The ratio of magnesium to iron is used as the ratio of forsterite to fayalite in the interstellar environment. The number of grains is plotted against the size of the grain in Figure 3.15.

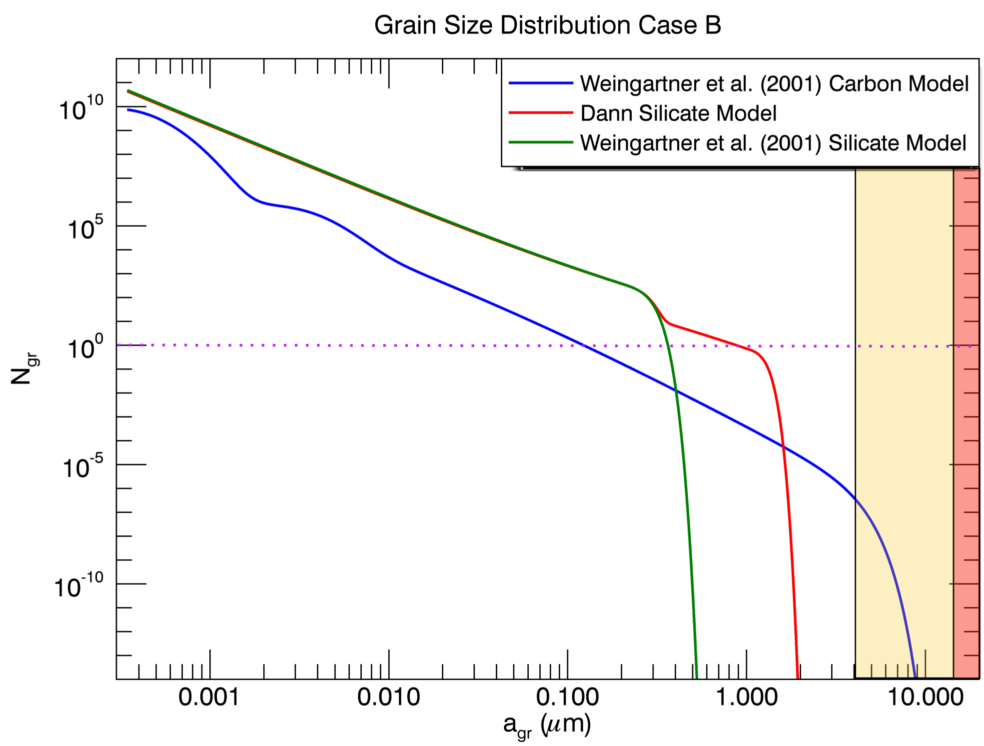

Figure 3.15: Grain radii plotted against the number of grains based on the model given in Weingartner & Draine (2001) It also shows an added silicate component in red that fits the dust grain mass measurements from *Galileo* and *Ulysses* missions shown in Frisch et al. (1999) and shown in Figure 3.16. The red zone denotes where Hoang et al. (2016) finds that a nanocraft with dimensions: $L = 5$ cm and $H = 0.3$ cm with density $\rho \sim 2.2$ g cm^{-3} will be completely destroyed by a dust grain larger then 15 μm. The yellow corresponds with the destruction of a spacecraft with $L = 1$ cm and H= 0.1 cm at $\sim 4\mu$m.

3.7.2 Discussion of Grain Size distribution

When we plotted the mass distribution and compared with the mass of particles measured by the *Ulysses* and *Galileo* missions within the heliosphere in Frisch

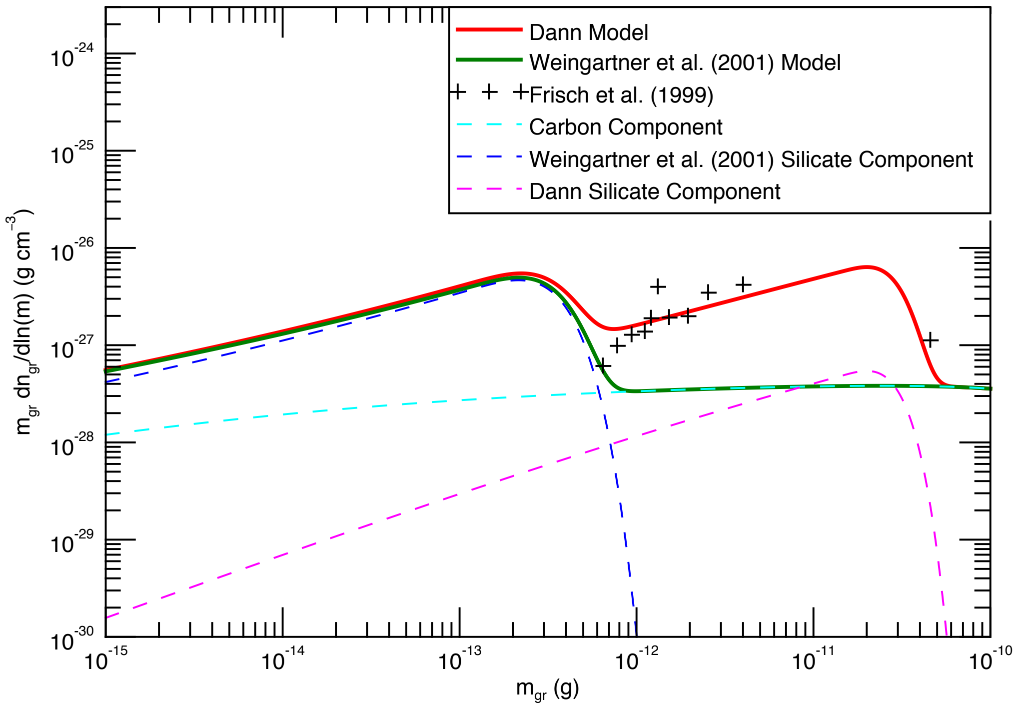

Figure 3.16: Distribution of grain masses where the dashed lines represent the individual components of the bold lines (Weingartner & Draine 2001).

et al. (1999), we wanted to change the model slightly to account for the discrepancy between the Frisch et al. (1999) measurements and Weingartner & Draine (2001), as Weingartner & Draine (2001) shows in their Figure 24. We, therefore, fit another silicate component to replicate the data. From this adjusted model we expect *Breakthrough Starshot* to encounter even larger grains.

HD Number	Model	$N_gr \geq 1\mu$m	$N_gr \geq 4\mu$m	$N_gr \geq 15\mu$m	For/Fay (%)
128621.....	Weingartner & Draine (2001)	0.092	$4.01e-05$	$2.07e-42$	50.2/49.8
	Our Model	137.72	$4.01e-05$	$2.07e-42$	50.2/49.8

Table 3.9: Probabilities of grains along the α-Centauri B line of sight.

By assuming a silicate grain distribution, we are only affecting the small grain distribution because of its sharp cutoff. This is a lower limit on the number of grains at each interval. We are not showing results for HD 128620 because of an overabundance of observed oxygen that is higher than solar values, this is likely caused by over-saturation seen in Figure 3.15.

3.8 Temperature and Turbulence

Using the Doppler widths of absorption features for various ions, we can constrain temperature and turbulence. This is because of the relationship between an atom's mass and its heat capacity. The more massive the atom, the less it will respond to changes in temperature, and therefore the less it will exhibit characteristics of thermal broadening. On the other hand, deuterium, as a light ion, gets hot and excited and moves with random motions in the presence of heat. Iron will be the best source of information about the turbulent or non-thermal broadening in the interstellar clouds of gas and dust. The observed line width b (the Doppler parameter) is related to the temperature (T) and turbulent velocity (ξ) in Equation 3.9.

$$b^2 = \frac{2kT}{m} + \xi^2 = 0.016629\frac{T}{A} + \xi^2, \tag{3.9}$$

where k is the Boltzmann constant, m is the mass of the ion, and A is the atomic weight of the ion in atomic mass units (amu). While it takes any two ions to solve the equation, it is best constrained by elements that have the largest difference in mass, deuterium and iron are preferable. It is extremely important to get accurate measurements of the widths. Magnesium is often used in conjunction with iron and deuterium because it of its high signal to noise in all of our spectra and because it is normally unsaturated.

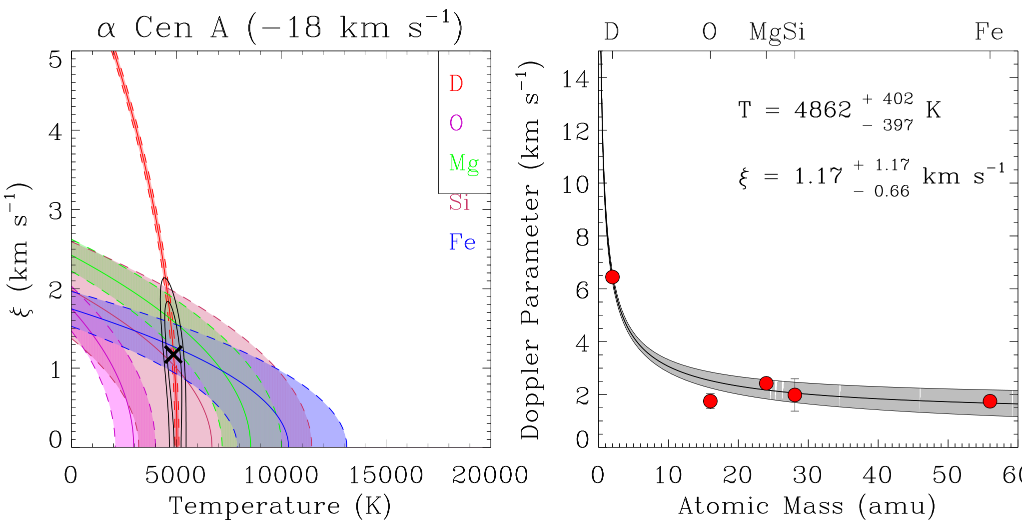

Figure 3.17: Temperature and turbulence curves for α Centauri A with deuterium, oxygen, magnesium, silicon, and iron. On the left plot, it shows solutions for individual ions using Equation 3.9. The shaded region surrounding the solution is a function of the error in the Doppler parameter of the fit. Notice the vertical nature of the lighter ions that have a better constraint on temperature. The X marks the mean of the solutions weighted by their errors. The plot on the right shows in shaded grey the model Doppler parameter for the given temperature and turbulence based on the atomic mass of the ion. The dots indicate the true Doppler parameter from the fits and their associated errors. When the dots are red, the absorption feature has high resolution (E140H or E230H), when it is blue it is of medium resolution (E140M or E230M). The black contours denote the $\pm 1\sigma$ errors.

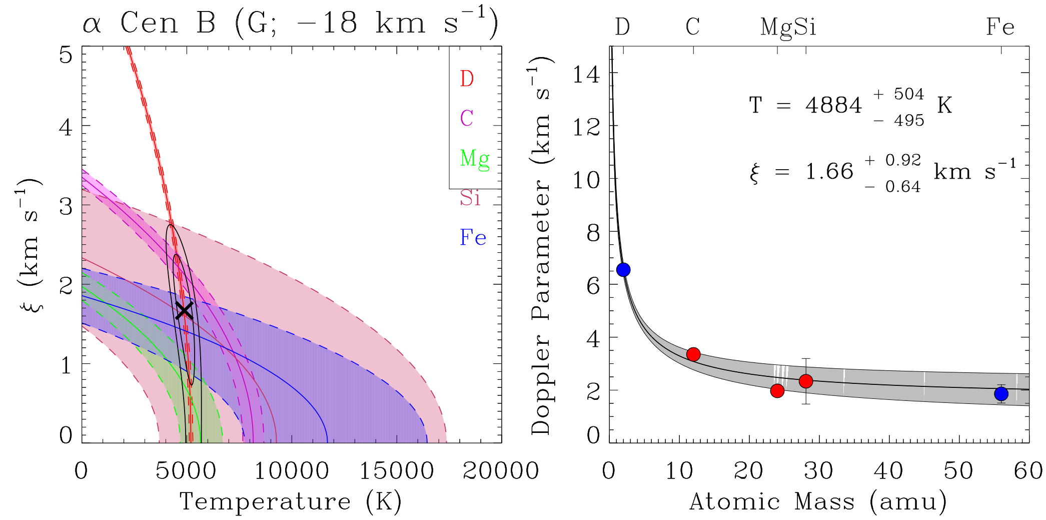

Figure 3.18: Temperature and turbulence curves for α Centauri B with deuterium, carbon, magnesium, silicon, and iron with the same formatting as Figure 3.17.

3.9 Implications on Breakthrough Starshot

Hoang et al. (2016) predicts that the most destructive part of the ISM for the Breakthrough Starshot mission will be large dust grains. These large grains have the ability to entirely destroy their proposed craft, called the StarChip. They are concerned that dust grains larger than 4 or 15 μm depending on the dimensions of the StarChips, of either a graphite or silicate composition will upon impact explode a gram-scale spacecraft traveling at 0.2c. Smaller grains might not completely destroy the spacecraft but they will deflect the nano-crafts or melt the surface through cratering. As a micron sized dust grain hits the chip, atoms, within a volume proportional to the size of the grain, will be heated above the binding energy, such that they escape from the surface leaving a crater behind (Hoang et al. 2016). Our proposed adjustment to the Weingartner & Draine (2001) model would imply the presence of a relatively large population of grains that have $a \sim 1\mu$m. This will result in more frequent collisions and a larger layer of destroyed material on the StarChip. Therefore, shielding mechanisms for the crafts must account for this considerable change. Future work will quantify the increased cratering caused by this new population of micron sized grains.

Gas also affects the spacecrafts by degrading the surface through the transfer of kinetic energy into heat during collisions. We have measured the temperature and turbulence for both lines of sight based on the Doppler parameters for various ions. Our results can be found in Table 5.1 and in Figures 3.17 and 3.18. The temperatures that we find are considerably lower than the assumed temperature of the LISM (7000 K), which could imply that larger dust grains are more likely to form. We compare the temperatures and turbulence with previously measured values from Redfield & Linsky (2004b) in Chapter 5.

Our analysis of the average composition of the dust through depletion measurements confirms that it is somewhere near olivine composition. Therefore, it was appropriate to use the Weingartner & Draine (2001) model for dust size distributions. From our added component to fit the in-situ measurements from Frisch et al. (1999), we derive probabilities of encountering a grain larger than 4 μm is $\sim 2e-05$ and for grains larger than 15 μm it is highly unlikely at $\sim 1e-41$. These are lower limits which will be explored further by introducing new compositions, measuring more ion transitions, and observing other nearby lines of sight.

Chapter 4

ASTRAL Stars

The Advanced Spectral Library Project (ASTRAL) is an *HST* Large Treasury Project whose goal is to collect high resolution ultraviolet spectrums of bright stars using STIS. The project's principal investigator is Thomas Ayres at the University of Colorado (CASA). In order to get a broadband spectra covering the entire UV, multiple exposures were taken in the far-UV ($1150 - 1700$ Å) and the near-UV ($1600 - 3100$ Å) with a variety of grating settings. In order to maximize the signal to noise ratio, they took $2 - 5$ exposures with integration times of $1000 - 3000$ seconds for each setting. Slight shifts on the detector are caused by systematic error in the STIS grating positioning mechanism and changes in the projected velocity due to telluric and spacecraft motions. The variety of grating settings allows for proper calibration of the wavelength array.

4.1 Post-processing of STIS Spectra

ASTRAL post-processing follows protocols from the StarCAT project and is elaborated on in Ayres (2010). The process begins with the *calstis* pipeline "x1d" file with extracted wavelengths, flux densities, photometric errors, and data quality flags of dozens of orders for the grating setting. After various post-facto adjustments of the instrument and telescope operations, the orders are stitched together with overlapping regions weighted by the individual sensitivity functions, accounting for bad pixels and wavelength gaps. An "active blaze correction" balances fluxes between adjacent orders. Blaze functions are caused by a grating-dependent variation in fluxes received by each order. In certain cases, exposures using E140H and E140M were co-added to increase the signal to noise in the overlapping region from 1150 to 1350 Å (Ayres 2010).

4.2 ASTRAL Fits

This section details the fitting for all of the ASTRAL hot and cool stars and the red giants that are not members of the α Centauri star system. They are organized by their distance from our solar system. Fits are performed in the manner described in Chapter 2.

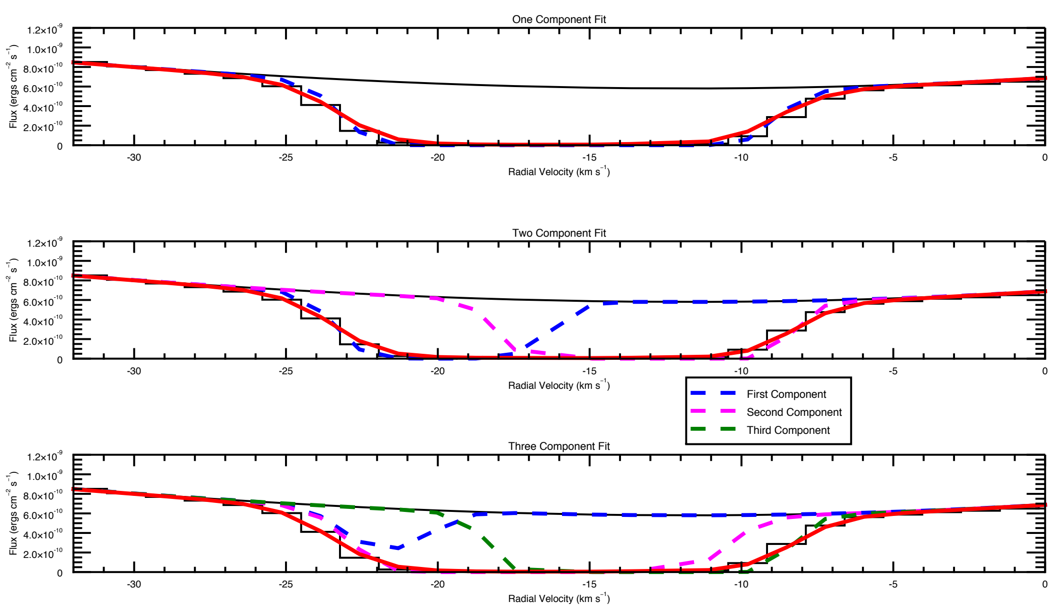

Figure 4.1: A comparison of a single magnesium fit with one, two, and three components. The two component fit is favored by the F-test although the Redfield & Linsky (2008) Kinematic model predicts three components. However, the extreme saturation leads us to not be able to make that assumption.

Many of these stars have been observed before which allows us to look for discrepancies and temporal changes. However, we take care not to allow previous results to influence our fitting procedure. For example HD 172167 was previously observed to have three components, however all features are super-saturated and an F-test confirms that the reduced chi-square of the two component fit is not significantly worse than the three component fit.(Figure 4.1)

Table 4.1: Historical Fits of Various Ions for ASTRAL Stars

HD No.	Other Name	Ion	Comp.	v (km s^{-1})	b (km s^{-1})	log N_{ion} (cm^{-2})	Reference
48915.....	α CMa A	D I	1	19.5	...	$12.43^{+0.14}_{-0.20}$	2
			2	13.7	...	$12.43^{+0.14}_{-0.20}$	2
		C II	1	17.6 ± 1.5	...	$14.62^{+0.23}_{-0.28}$	7
			2	11.7 ± 1.5	...	$13.78^{+0.15}_{-0.12}$	7
		Mg II	1	17.6 ± 1.5	...	$12.23^{+0.02}_{-0.03}$	7
			2	11.7 ± 1.5	...	$12.00^{+0.04}_{-0.05}$	7
			1	18.7 ± 1.1	2.71 ± 0.11	12.22 ± 0.04	10
			2	13.1 ± 1.1	3.08 ± 0.28	11.95 ± 0.06	10
		Fe II	1	17.6 ± 1.5	...	$11.94^{+0.01}_{-0.02}$	7
			2	11.7 ± 1.5	...	11.74 ± 0.03	7
			1	20.1 ± 1.1	2.05 ± 0.28	11.93 ± 0.03	9
			2	14.4 ± 1.1	3.00 ± 0.20	11.73 ± 0.15	9
61421.....	α CMi	D I	1	24.0 ± 0.10	7.59 ± 0.10	12.81 ± 0.03	3
			2	20.5 ± 0.10	7.59 ± 0.10	13.08 ± 0.04	3
		Mg II	1	20.80 ± 0.63	2.30 ± 0.07	12.36 ± 0.02	3
			2	23.37 ± 0.95	2.30 ± 0.07	12.11 ± 0.02	3
		Fe II	1	22.0 ± 0.10	2.1 ± 0.10	11.94 ± 0.03	3
			2	19.0 ± 0.10	2.1 ± 0.10	12.05 ± 0.02	3
			1	20.23 ± 0.10	2.71 ± 0.13	12.27 ± 0.02	8
172167.....	α Lyr	N I	1	-12.06 ± 2.16	3.10 ± 1.87	13.80 ± 0.13	6
			2	-18.52 ± 2.77	3.88 ± 1.95	13.64 ± 0.11	1
		Si II	1	-13.63 ± 1.64	1.73 ± 0.84	14.76 ± 0.33	6
			2	-17.49 ± 1.95	1.83 ± 0.72	14.69 ± 0.23	6
			3	-19.99 ± 2.08	2.26 ± 0.91	14.64 ± 0.25	6
		Fe II	1	-12.7 ± 1.5	2.25	13.03	8
			2	-16.0 ± 1.5	1.53	12.84	8
			3	-18.3 ± 1.5	1.83	12.81	8
62509.....	β Gem	D I	1	33.0 ± 1.0	7.8 ± 0.7	13.0 ± 0.1	4
			2	21.9 ± 1.0	8.7 ± 0.7	13.2 ± 0.1	4
		O I	1	32.67 ± 0.38	4.05 ± 1.31	14.25 ± 0.26	6
			2	21.39 ± 0.35	4.07 ± 0.89	14.56 ± 0.26	6
		Mg II	1	33.4 ± 0.6	2.49 ± 0.21	12.15 ± 0.03	4
			2	22.2 ± 0.6	3.18 ± 0.43	12.53 ± 0.04	4
		Fe II	1	31.52 ± 0.17	2.80 ± 0.28	11.97 ± 0.03	10
			2	19.36 ± 0.11	2.31 ± 0.18	12.23 ± 0.03	10
432.....	β Cas	D I	1	10 ± 1	...	13.4 ± 0.1	5
		Mg II	1	9.9 ± 0.4	2.55 ± 0.25	12.44 ± 0.08	4
		Fe II	1	9.5 ± 0.3	1.78 ± 0.8	12.36 ± 0.1	4
87901.....	α Leo	C II		...	...	≤ 9.62	11
164058.....	γDra	Mg II		$-20$to-5	...	≤ 13.6	10

Table 4.1: (1) Linsky & Wood (1996); (2) Bertin et al. (1995); (3) Linsky et al. (1995); (4) Dring et al. (1997); (5) Piskunov et al. (1997); (6) Redfield & Linsky (2004a); (7)Hébrard et al. (1999); (8) Lallement et al. (1995); (9)Lallement et al. (1994); (10) Redfield & Linsky (2002)(11) Vallerga et al. (1993)

We can compare these previous measurements with our own results from

HST/STIS data taken in May of 2015 in Table 4.2.

Table 4.2: May 2015 ASTRAL Target Fits

HD No.	Other Name	Ion	Comp.	v (km s^{-1})	b (km s^{-1})	log N_{ion} (cm^{-2})
48915.....	α CMa A	C II	1	13.34 ± 0.217	2.36 ± 0.39	14.01 ± 0.21
			2	19.69 ± 3.75	4.60 ± 1.76	13.69 ± 0.23
		Mg II	1	13.47 ± 0.14	2.488 ± 0.092	$11.966^{+0.014}_{-0.014}$
			2	19.49 ± 0.14	2.707 ± 0.084	$12.3173^{+0.0058}_{-0.0058}$
		Si (3)	1	8.88 ± 3.66	2.24 ± 2.13	12.016 ± 0.314
			2	16.21 ± 0.93	2.012 ± 0.84	13.020 ± 0.39
		Fe II	1	13.90 ± 0.29	2.33 ± 0.32	$11.718^{+0.087}_{-0.072}$
			2	19.88 ± 0.16	2.20 ± 0.15	$12.04^{+0.025}_{-0.024}$
61421.....	α CMi	D I	1	16.88 ± 0.21	6.29 ± 0.18	12.858 ± 0.021
			2	22.28 ± 0.22	6.56 ± 0.19	12.951 ± 0.017
		C II	1	19.75 ± 0.18	4.82 ± 0.089	13.675 ± 0.050
			2	20.55 ± 2.30	4.63 ± 0.80	12.99 ± 0.64
		N I (1)	1	18.74 ± 1.23	3.88 ± 1.45	13.05 ± 0.11
			2	21.90 ± 2.63	4.24 ± 1.41	13.07 ± 0.16
		N I (2)	1	18.60 ± 1.33	3.49 ± 1.52	12.57 ± 0.13
			2	20.38 ± 1.38	3.32 ± 1.54	13.04 ± 0.11
		O I	1	16.13 ± 0.76	1.58 ± 0.18	13.12 ± 0.11
			2	20.857 ± 0.097	3.98 ± 0.10	13.9393 ± 0.0088
		Mg II	1	18.75 ± 0.33	2.07 ± 1.12	$11.68^{+0.17}_{-0.49}$
			2	19.46 ± 0.16	3.63 ± 0.14	$12.29^{+0.35}_{-0.19}$
		Fe II	1	17.98 ± 2.72	2.57 ± 0.75	$11.89^{+0.12}_{-0.17}$
			2	18.70 ± 1.41	3.03 ± 0.81	$12.06^{+0.44}_{-0.21}$
172167.....	α Lyr	Mg II	1	-13.49 ± 3.77	2.57 ± 0.75	$13.53^{+0.29}_{-0.17}$
			2	-18.18 ± 4.018	2.17 ± 0.56	$12.92^{+0.76}_{-0.89}$
		Fe II	1	-12.87 ± 0.92	2.04 ± 0.18	$13.078^{+0.29}_{-0.40}$
			2	-17.24 ± 0.33	2.39 ± 0.22	$13.23^{+0.16}_{-0.43}$
62509.....	β Gem	D I	1	18.13 ± 1.36	8.04 ± 0.71	12.94 ± 0.18
			2	27.85 ± 1.09	10.03 ± 0.55	13.440 ± 0.085
		C II	1	21.06 ± 1.71	5.54 ± 1.08	13.80 ± 0.28
			2	28.00 ± 1.60	5.27 ± 1.08	13.94 ± 0.18
		N I(1)	1	21.63 ± 1.70	3.07 ± 0.97	13.51 ± 0.22
			2	28.77 ± 4.30	4.50 ± 1.70	13.30 ± 0.40
		O I	1	20.99 ± 0.49	4.64 ± 0.38	13.931 ± 0.047
			2	30.24 ± 0.59	4.85 ± 0.50	13.894 ± 0.054
		Mg II	1	19.652 ± 0.024	2.927 ± 0.080	$12.6526^{+0.0067}_{-0.0066}$
			2	30.899 ± 0.040	2.288 ± 0.065	$12.174^{+0.012}_{-0.012}$
		Fe II	1	19.250 ± 0.050	2.421 ± 0.070	$12.265^{+0.037}_{-0.034}$
			2	30.95 ± 0.50	1.91 ± 0.41	$11.86^{+0.048}_{-0.043}$
432.....	β Cas	D I	1	7.138 ± 0.069	8.421 ± 0.079	13.4079 ± 0.0034
		C II	1	6.280 ± 0.060	6.657 ± 0.069	13.8056 ± 0.0050
		Mg II	1	9.149 ± 0.055	3.28 ± 4.26	$12.49^{+0.045}_{-0.041}$
		Fe II	1	9.68 ± 0.18	1.74 ± 0.34	$12.126^{+0.051}_{-0.051}$
87901.....	α Leo	C II	1	8.14 ± 0.49	3.26 ± 0.12	14.02 ± 0.14
			2	16.15 ± 0.44	3.22 ± 0.20	14.033 ± 0.090
		N I(1)	1	10.44 ± 0.69	3.54 ± 0.47	13.94 ± 0.19
			2	14.81 ± 1.25	3.69 ± 0.80	13.61 ± 0.20
		N I(2)	1	10.08 ± 0.72	3.65 ± 0.66	13.85 ± 0.18
			2	15.77 ± 1.52	3.61 ± 1.03	13.53 ± 0.18
		N I(3)	1	9.58 ± 0.43	3.13 ± 0.41	13.79 ± 0.12
			2	15.05 ± 1.11	4.33 ± 0.81	13.58 ± 0.11
		O I	1	7.81 ± 0.43	2.37 ± 0.18	14.42 ± 0.22
			2	15.05 ± 0.60	3.03 ± 0.27	14.61 ± 0.14
		Mg II	1	9.89 ± 0.16	2.518 ± 0.036	$12.666^{+0.082}_{-0.069}$
			2	15.33 ± 0.33	2.86 ± 0.32	$12.67^{+0.053}_{-0.047}$
		Si II	1	10.78 ± 0.68	2.87 ± 0.59	$13.00^{+0.16}_{-0.12}$
			2	16.69 ± 1.09	1.99 ± 0.80	$12.33^{+0.38}_{-0.20}$
		Fe II	1	10.169 ± 0.098	2.076 ± 0.063	$12.230^{+0.035}_{-0.033}$
			2	15.55 ± 0.52	2.62 ± 0.40	$11.84^{+0.059}_{-0.052}$
164058.....	γDra	C II	1	-12.57 ± 0.30	8.26 ± 0.67	14.34 ± 0.11
		C II	1	-12.60 ± 0.26	8.20 ± 0.68	13.000 ± 0.052
		N I (2)	1	-15.2757 ± 3.0038	8.50 ± 2.32	13.92 ± 0.32
		O I	1	-12.275 ± 0.039	3.422 ± 0.23	15.98 ± 0.23
		Mg II	1	-14.046 ± 0.046	3.87 ± 0.13	$14.33^{+0.25}_{-0.16}$
		Fe II	1	-13.59 ± 0.12	5.46 ± 0.38	$13.2237^{+0.0048}_{-0.0048}$

Continued on next page

Table 4.2 – continued from previous page

HD No.	Other Name	Ion	Component No.	v (km s^{-1})	b (km s^{-1})	$\log N_{ion}$ (cm^{-2})
17573.....	41 Ari	C II	1	15.23 ± 0.55	2.78 ± 0.20	15.59 ± 0.24
			2	20.12 ± 1.66	3.67 ± 0.94	13.93 ± 0.26
		N I (1)	1	15.77 ± 0.74	3.56 ± 0.73	13.39 ± 0.13
			2	21.13 ± 0.78	3.28 ± 0.65	13.358 ± 0.084
		N I (2)	1	16.98 ± 0.81	5.68 ± 0.68	13.47 ± 0.14
			2	19.13 ± 0.56	3.94 ± 0.49	13.35 ± 0.11
		O I	1	17.005 ± 0.065	4.770 ± 0.049	14.435 ± 0.021
			2	19.08 ± 0.32	2.10 ± 0.33	13.96 ± 0.20
		Mg II	1	14.97 ± 0.18	2.50 ± 0.15	$12.345^{+0.025}_{-0.023}$
			2	19.60 ± 0.14	2.66 ± 0.14	$12.499^{+0.024}_{-0.023}$
		Fe II	1	15.15 ± 0.13	1.58 ± 0.13	$12.086^{+0.057}_{-0.051}$
			2	19.62 ± 0.20	2.39 ± 0.30	$12.173^{+0.037}_{-0.034}$

Table 4.2: The ions with numbers within parentheses are the individual fits for ions than generally have multiple resonance lines. This is generally because only the ion transitions with the largest oscillator strengths are visible and simultaneous fits can not be made. The number refers to the ion transitions shown in Table 2.1 ordered from short to long wavelengths.

By taking the weighted mean of the radial velocities of all individual and simultaneous fits for all ions we can compare the results with Redfield's Kinematic Model from Redfield & Linsky (2008). Errors are the result of a standard deviation of the fit values. The results of this can be found in Table 4.4 and Figure 4.2.

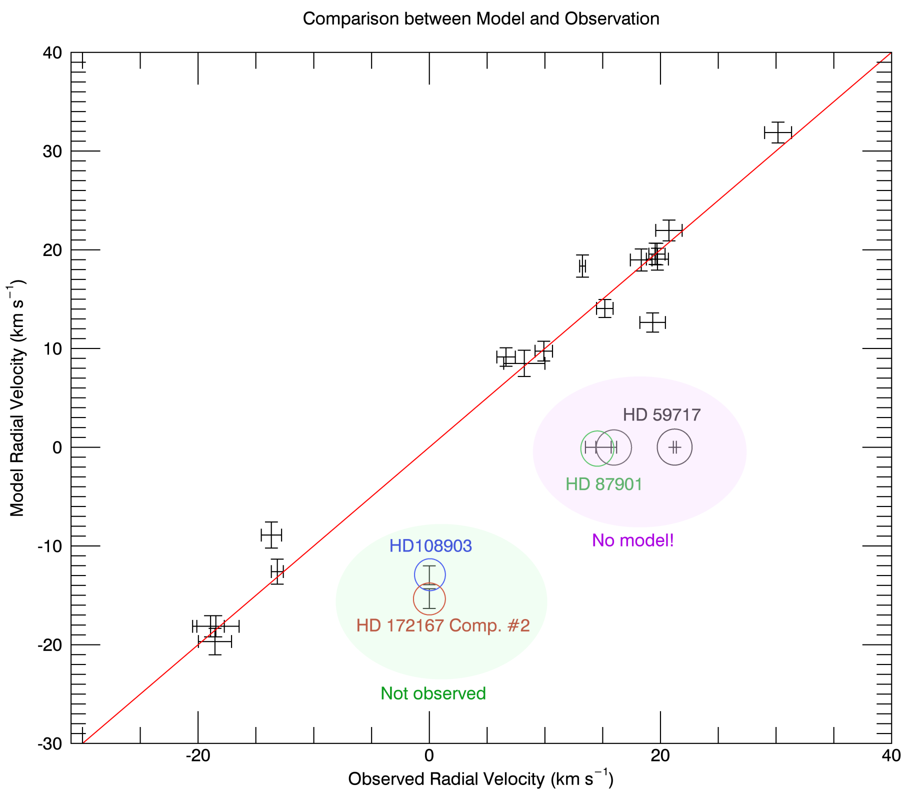

Figure 4.2: This is a comparison of our measurements with the Redfield & Linsky (2008) model with both of their associated errors. The two areas lined up on the 0 axes are the areas in which there is either no model or no observation of the predicted absorption feature. Generally there is very good agreement between the model and observations.

Table 4.3: Kinematic Model Prediction Comparison

HD Number	Comp.	Avg. v (km s^{-1})	Predicted v (km s^{-1})	Cloud Name
128621.....	1	-18.93 ± 1.19	-18.14 ± 1.07	G
128620.....	1	-18.47 ± 2.01	-18.14 ± 1.07	G
48915.....	1	13.26 ± 0.25	18.35 ± 1.13	LIC
	2	19.33 ± 1.11	12.64 ± 0.97	Blue
61421.....	1	18.34 ± 0.94	18.97 ± 1.11	LIC
	2	20.74 ± 1.14	21.96 ± 1.05	Aur
172167.....	1	-13.15 ± 0.52	-12.60 ± 1.27	LIC
	2	...	-15.33 ± 1.00	G
	3	-18.54 ± 1.43	-19.68 ± 1.34	Mic
62509.....	1	19.74 ± 0.95	19.05 ± 1.10	LIC
	2	30.18 ± 1.17	31.87 ± 1.05	Gem
432.....	1	8.22 ± 1.78	8.49 ± 1.33	LIC
87901.....	1	9.91 ± 0.75	9.73 ± 1.00	Leo
	2	15.31 ± 0.90	...	Unknown
108903.....	1	...	-12.97 ± 0.96	G
164058.....	1	-13.66 ± 0.88	-8.90 ± 1.32	LIC
17573.....	1	19.70 ± 0.70	19.56 ± 1.09	LIC
	2	15.19 ± 0.71	14.06 ± 0.91	Hyades
Red Giants				
59717.....	1	6.64 ± 0.80	9.14 ± 0.94	Blue
	2	14.63 ± 1.11	...	Unknown
	3	21.25 ± 0.13	...	Unknown
	4	83.68 ± 0.10	...	Astrosphere
25025.....	1	19.547 ± 0.017	19.60 ± 1.08	LIC
	2	56.47 ± 0.10	...	Astrosphere

Table 4.4: This table gives the average absorption feature radial velocities for all ions compared with the prediction from Redfield & Linsky (2008) and the names of the cloud responsible for the feature.

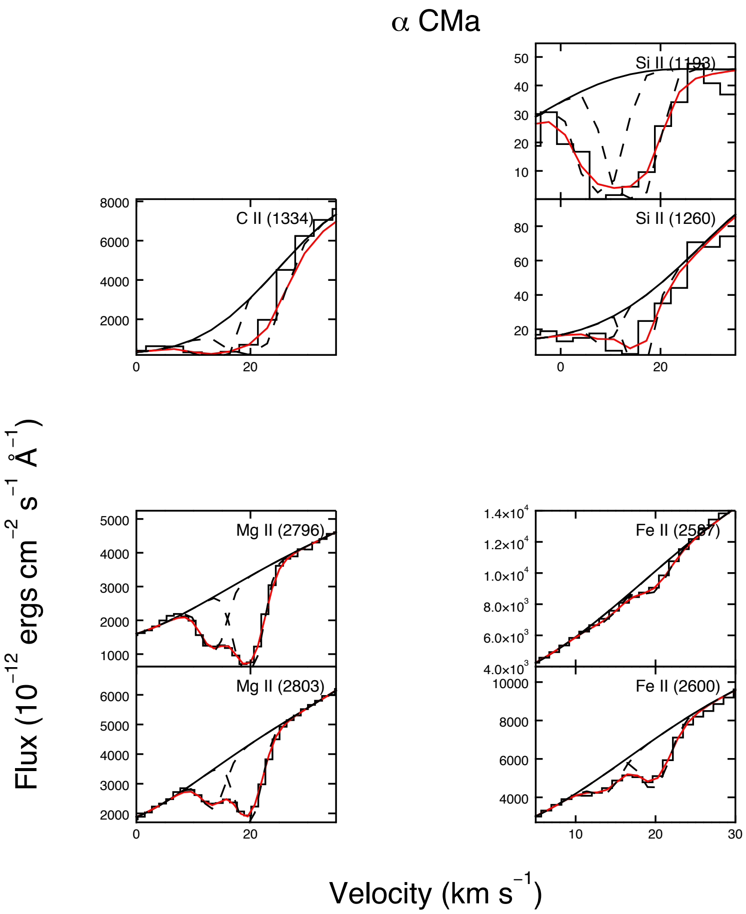

Figure 4.3: Absorption features for HD 48915, where the black histogram is the data, the black line is the reconstructed continuum, the thick red line is the fit, and the black dashed lines denote the individual components. The dashed green lines in these figures denote the expected radial velocity of geocoronal absorption. The y-axis for each figure has been modified by a scale factor of 10^{12} and all of the x-axis are on the same scales except for the iron fits.

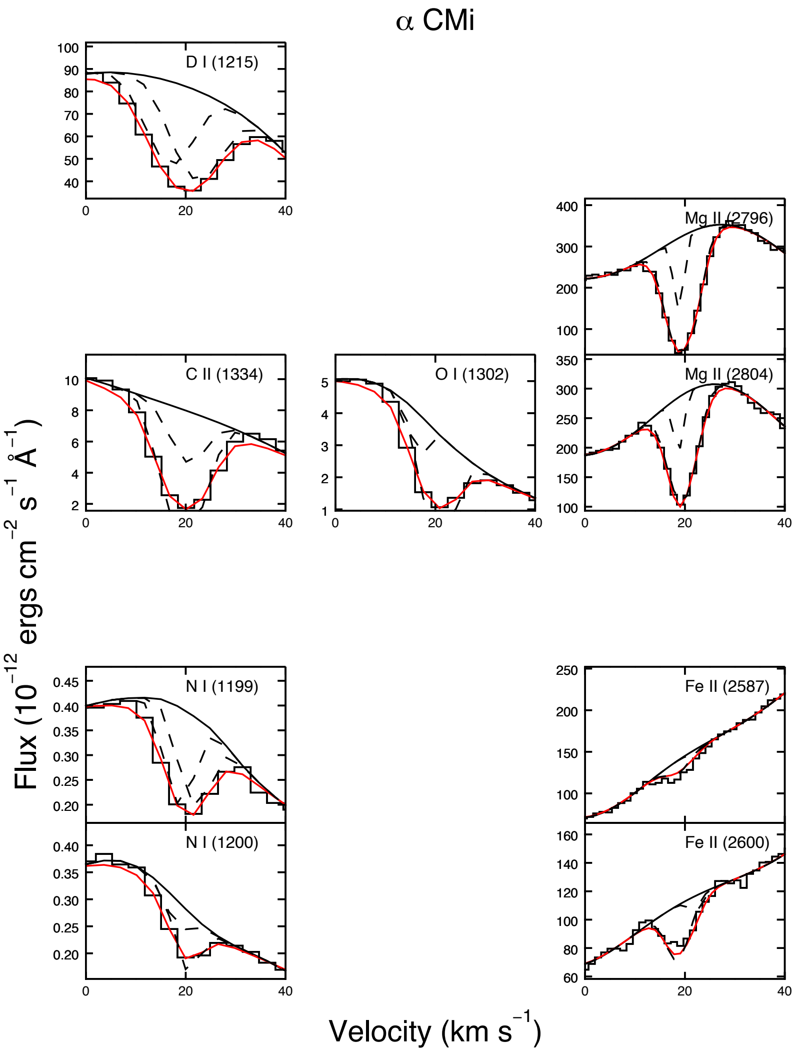

Figure 4.4: Absorption features for HD 61421, see caption from Figure 4.3.

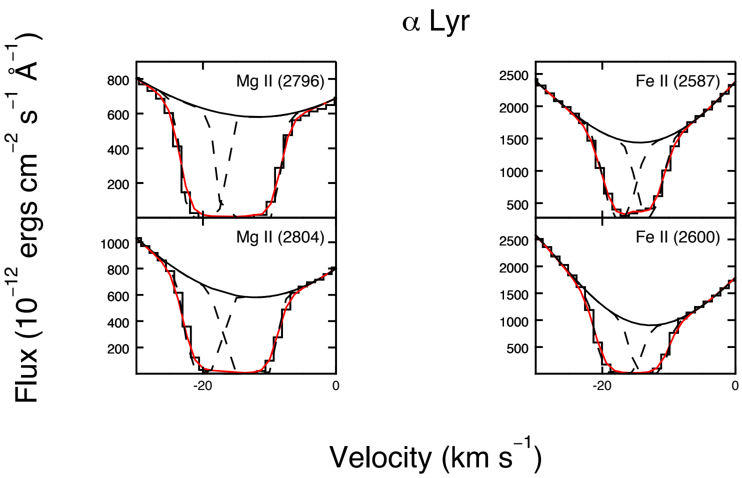

Figure 4.5: Absorption features for HD 172167, see caption from Figure 4.3.

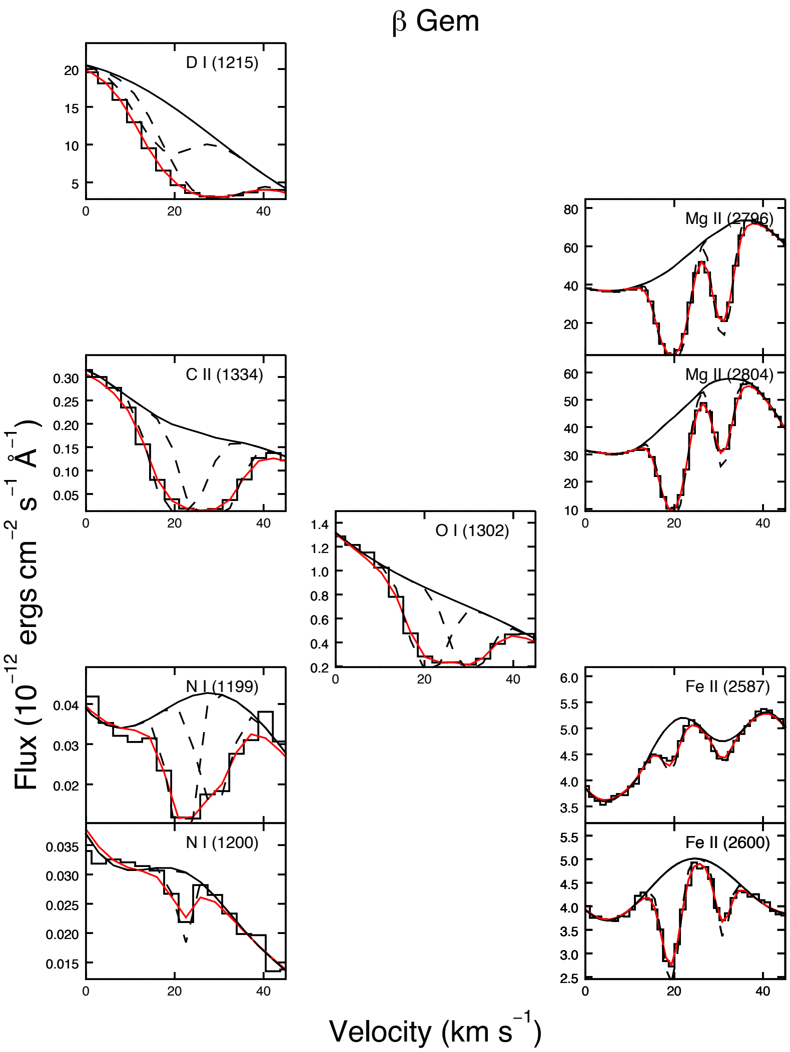

Figure 4.6: Absorption features for HD 62509, see caption from Figure 4.3.

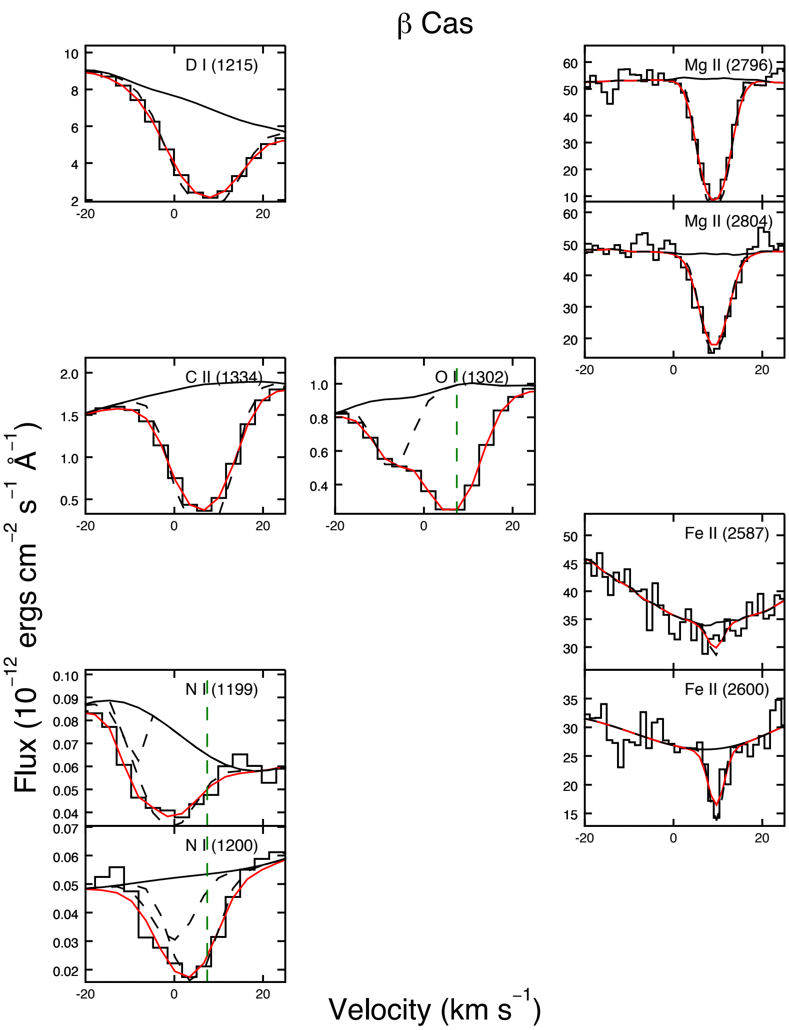

Figure 4.7: Absorption features for HD 432, see caption from Figure 4.3. In this figure we have added in the velocity at which we should see geocoronal absorption in nitrogen and oxygen; this is also the reason for a two component fit.

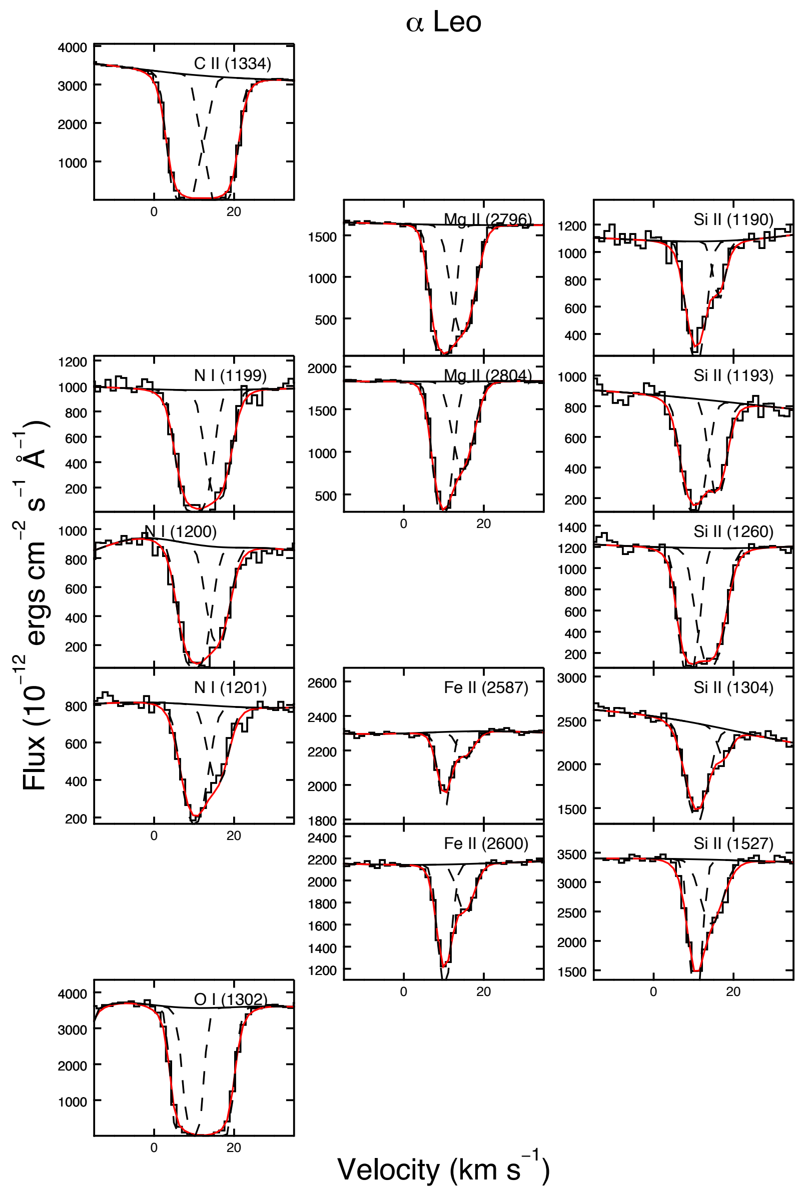

Figure 4.8: Absorption features for HD 87901, see caption from Figure 4.3.

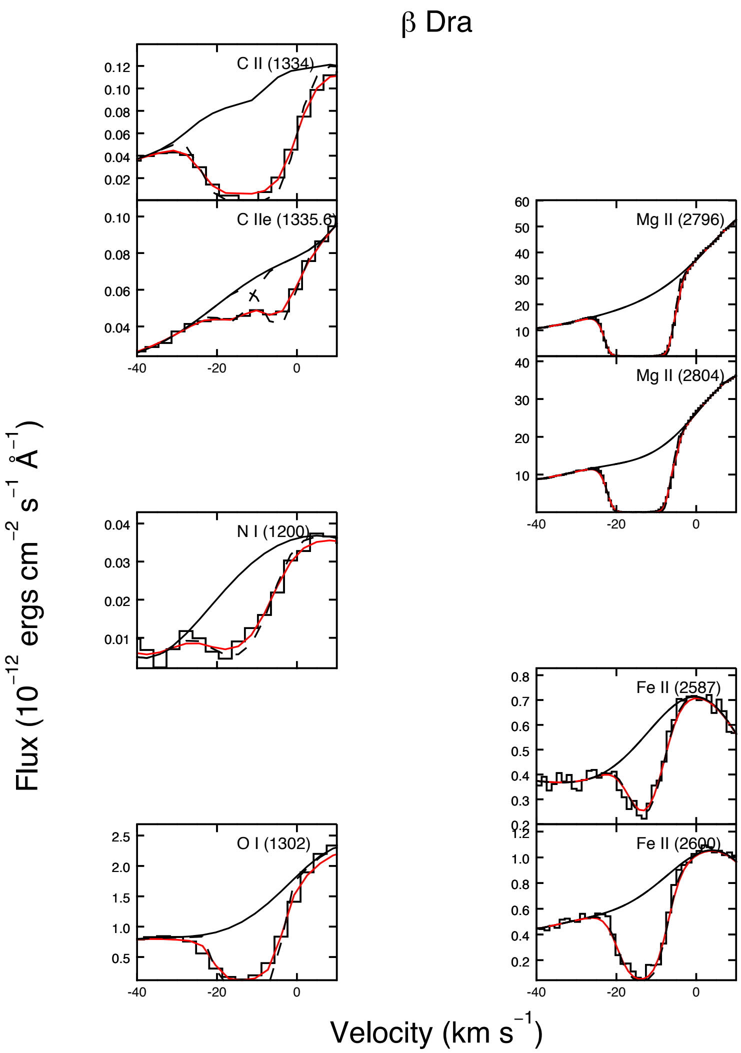

Figure 4.9: Absorption features for HD 164058, see caption from Figure 4.3.

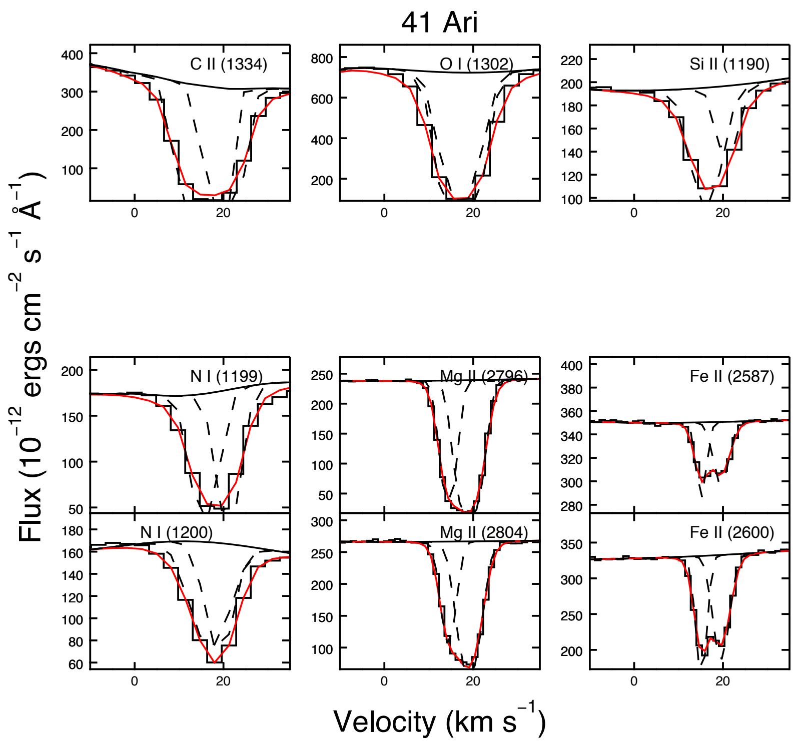

Figure 4.10: Absorption features for HD 17573, see caption from Figure 4.3.

4.3 Temperature and Turbulence

This section shows temperature and turbulence plots for all of the stars possible from the sample. We present all fits with converging amoebas, a multidimensional minimization function of Equation 2.1.

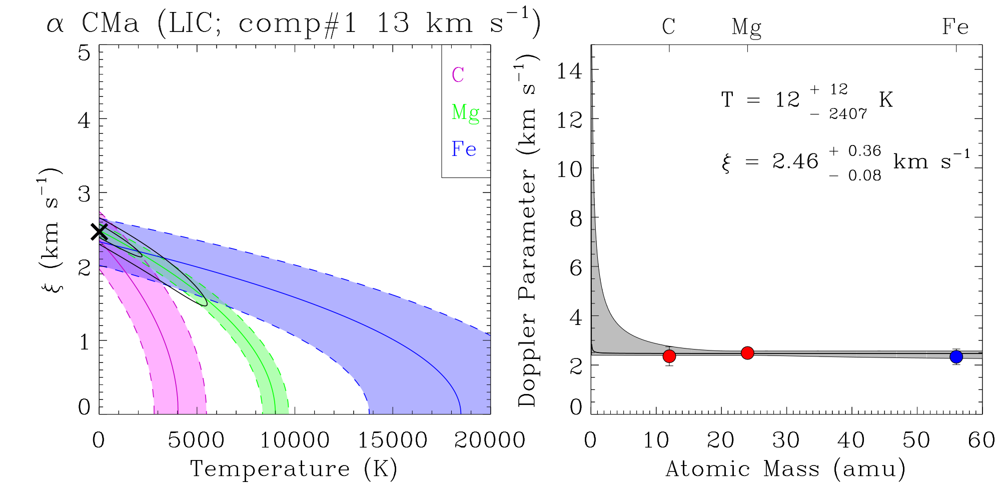

Figure 4.11: Temperature and turbulence curves for HD 48915 component #1. On the left plot, it shows solutions for individual ions using Equation 3.9. The shaded region surrounding the solution is a function of the errors in the Doppler parameter of the fit. Notice the vertical nature of the lighter ions that have a better constraint on temperature. The X marks the mean of the solutions weighted by their errors. The plot on the right shows in shaded grey the model Doppler parameter for the given temperature and turbulence based on the atomic mass of the ion. The red dots (high-res) and the blue dots (low-res) indicate the true Doppler parameter from the fits and their associated errors. The black contours denote the $\pm 1\ \sigma$ errors.

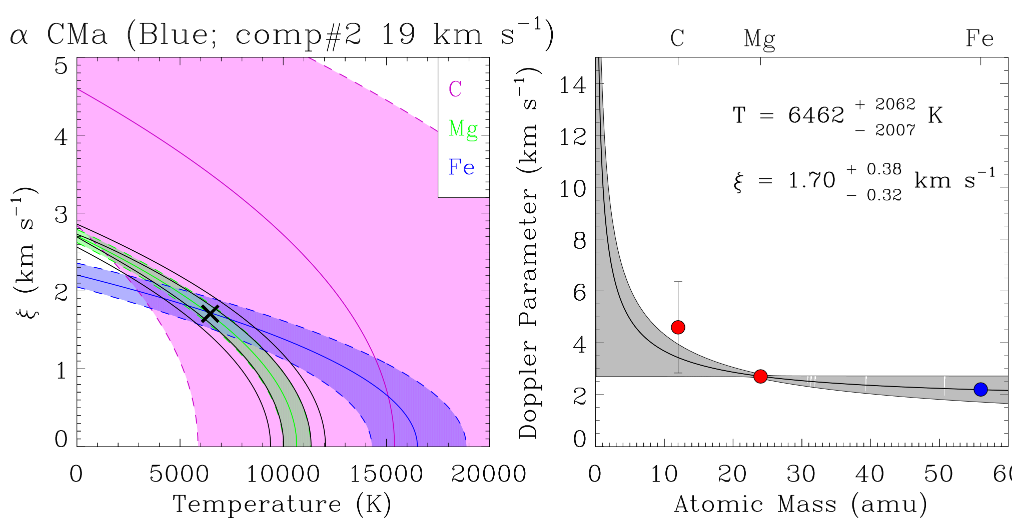

Figure 4.12: Temperature and turbulence curves for HD 48915 component #2, see caption from Figure 4.11.

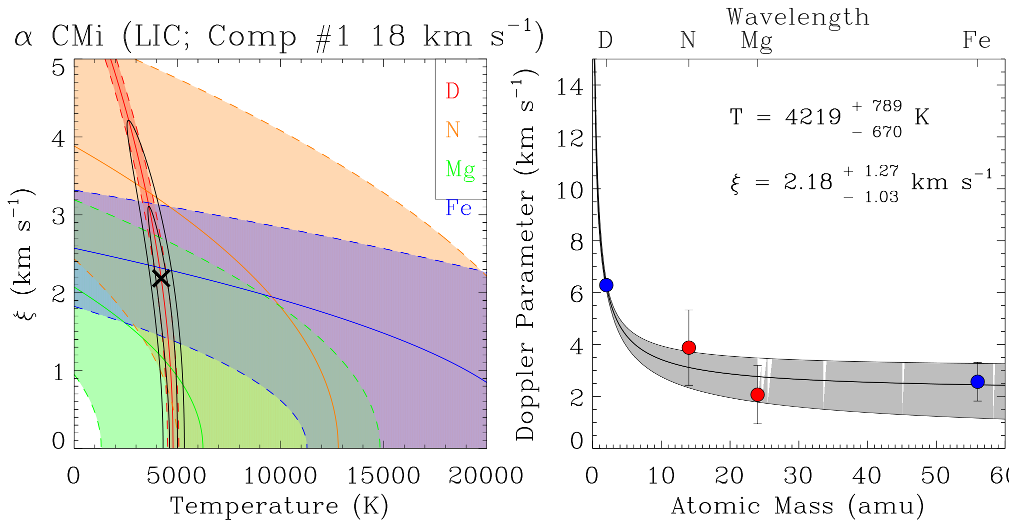

Figure 4.13: Temperature and turbulence curves for HD 61421 component #1, see caption from Figure 4.11.

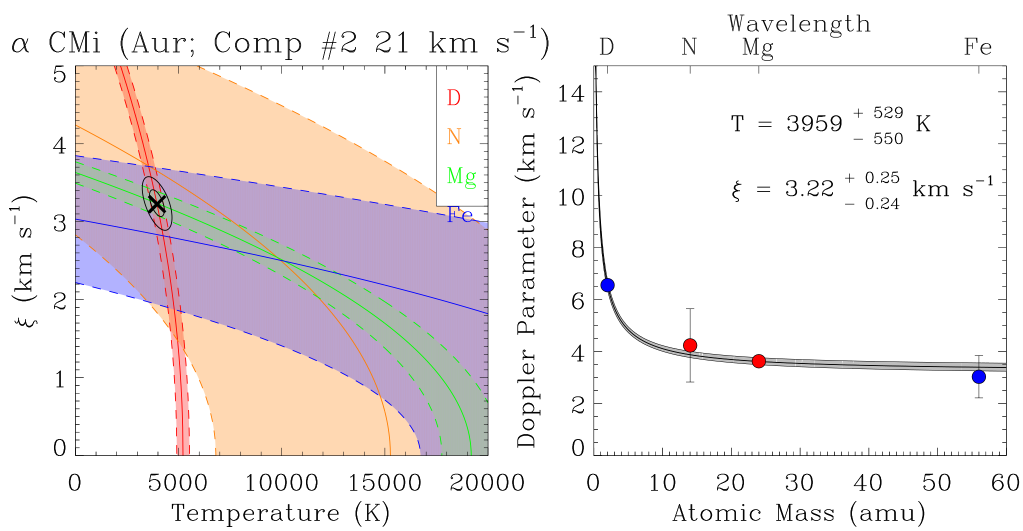

Figure 4.14: Temperature and turbulence curves for HD 61421 component #2, see caption from Figure 4.11.

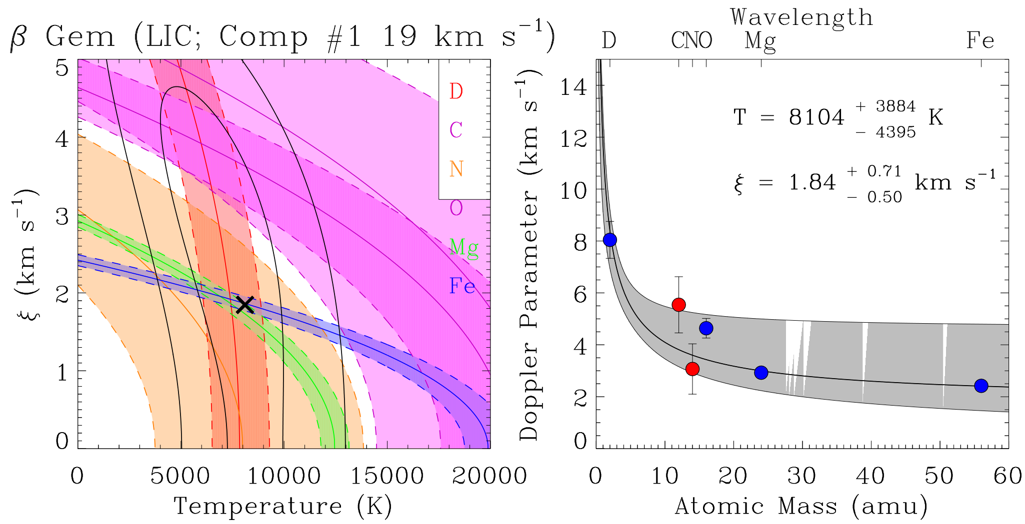

Figure 4.15: Temperature and turbulence curves for HD 62509 component #1, see caption from Figure 4.11.

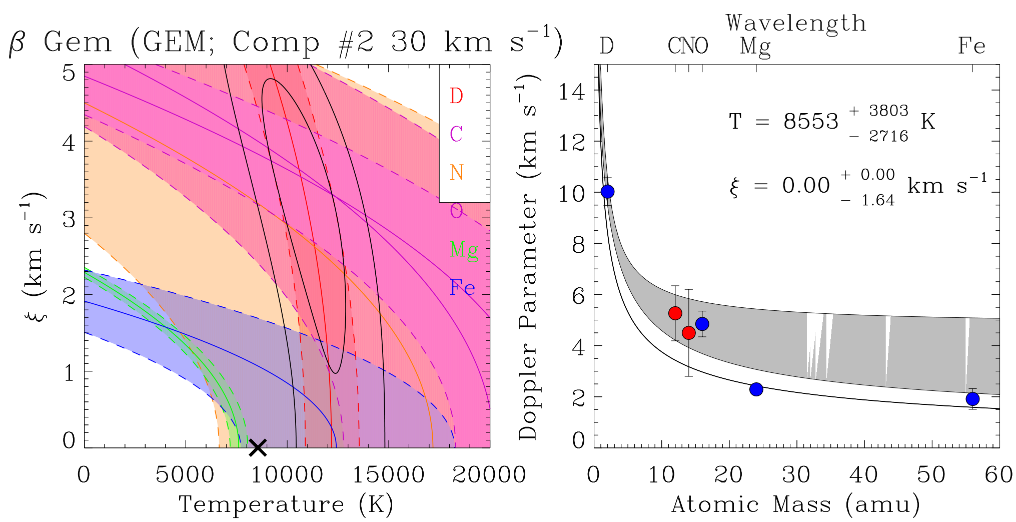

Figure 4.16: Temperature and turbulence curves for HD 62509 component #2, see caption from Figure 4.11.

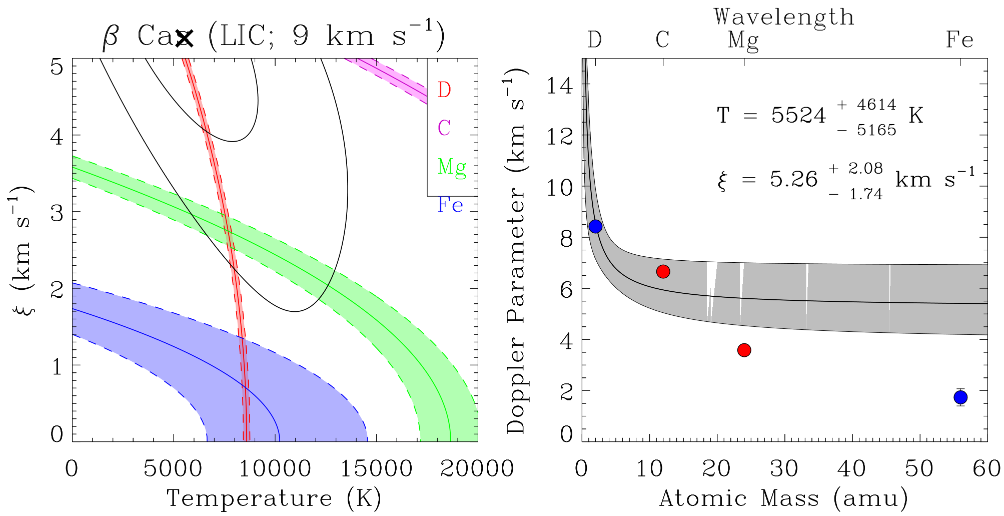

Figure 4.17: Temperature and turbulence curves for HD 432, see caption from Figure 4.11. This plot provides very inconclusive measurements due to inconsistencies in the absorption features in Figure 4.7.

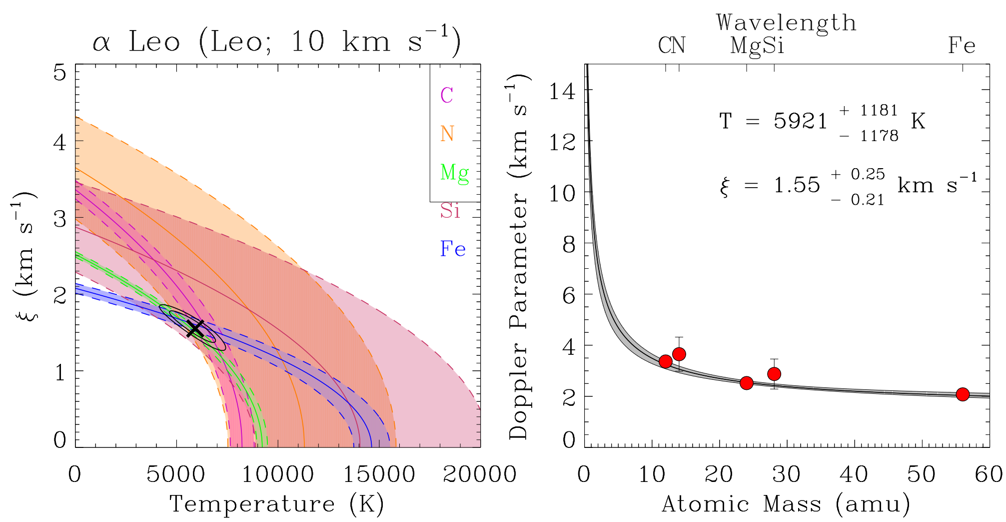

Figure 4.18: Temperature and turbulence curves for HD 87901 component #1, see caption from Figure 4.11.

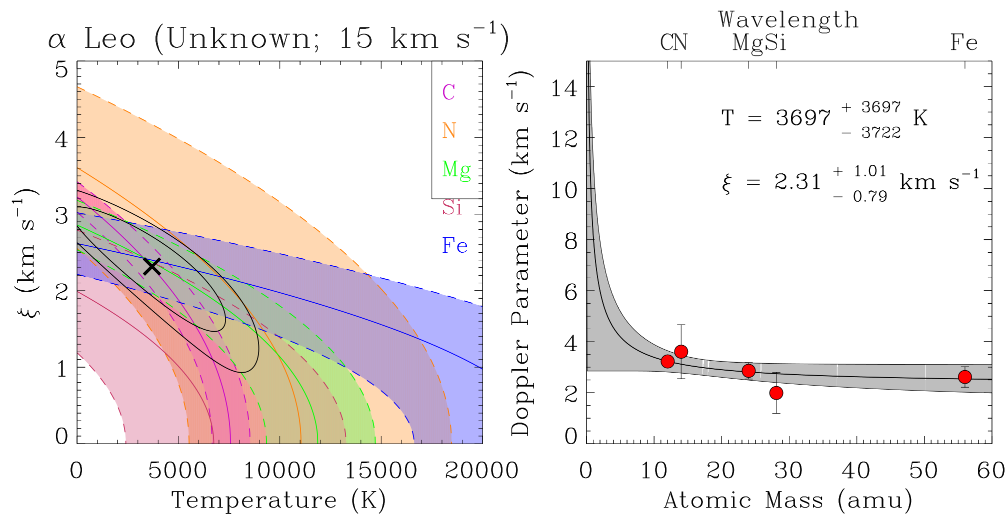

Figure 4.19: Temperature and turbulence curves for HD 87901 component #2, see caption from Figure 4.11.

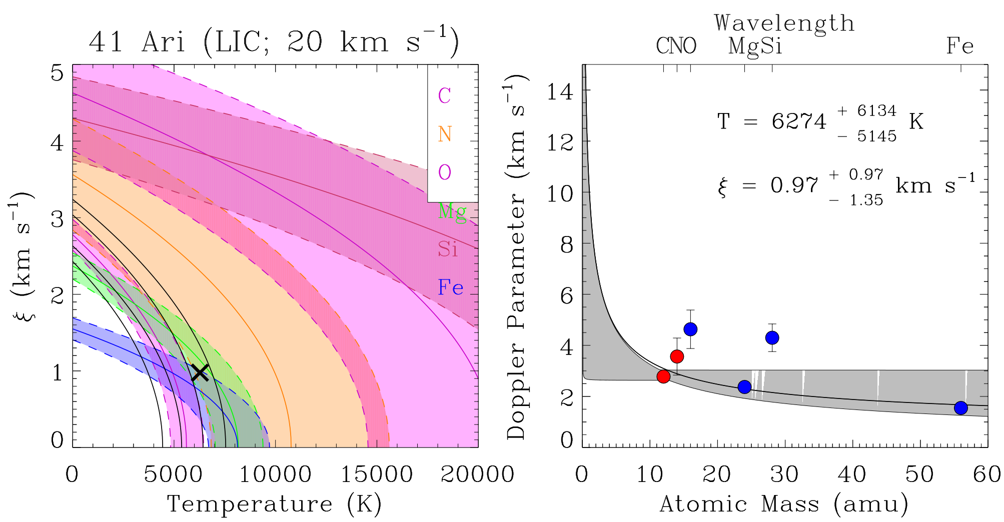

Figure 4.20: Temperature and turbulence curves for HD 17573 component #1, see caption from Figure 4.11.

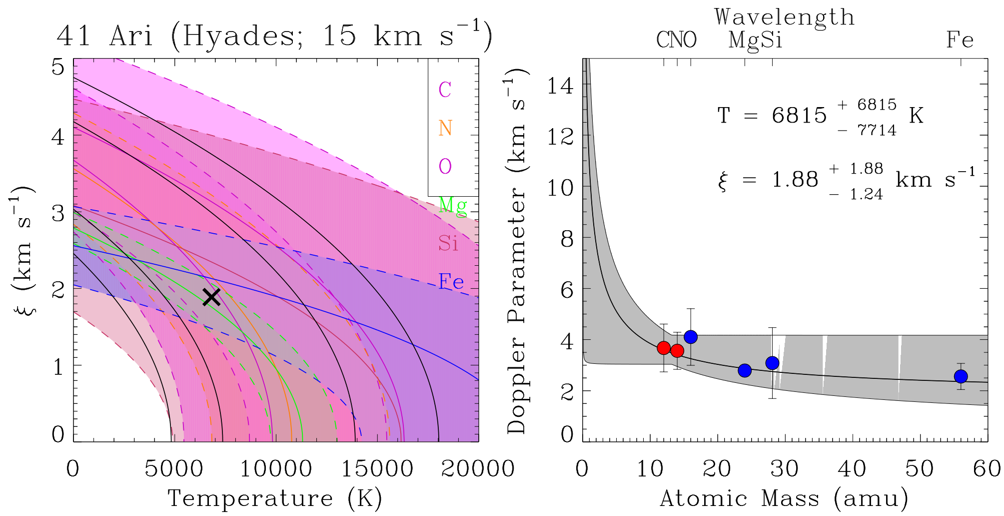

Figure 4.21: Temperature and turbulence curves for HD 17573 component #2, see caption from Figure 4.11.

From these temperature and turbulence plots, we notice that the oxygen and nitrogen Doppler parameters are generally less well constrained than the other components. This may be due to blending with geocoronal emission, which we hope to further investigate. We compare our measurements with Redfield & Linsky (2004b) in Chapter 5.

4.4 Red Giant Stars

We discuss the two red giant stars in a separate section because they present very different challenges and have unique features within their spectra. We look at only the magnesium doublet, in which we see evidence of astrospheres, strong stellar winds, and likely multiple ISM components. An example of this is found in Figure 2.5. Information about the two red giants can be found in Table 4.5.

These red giant stars are in a late stage of their life, in which they greatly increase in radii after switching to fusing a hydrogen shell surrounding their helium

Object Name (1)	Proper Name (2)	Distance (pc) (3)	V_{rad} (km/s) (4)	Stellar Type (5)
59717.....	σ-Pup	$59.38^{+1.65}_{-1.74}$	87.30 ± 0.74	K5III C
25025.....	γ-Eri	$62.34^{+2.18}_{-2.34}$	60.81 ± 0.25	M0III-B

Table 4.5: ASTRAL Red Giant Stars

core. This interesting particle interactions resulting in various features in the stellar spectra such as the huge saturation from stellar wind and the pronounced astrospheric absorption.

HD Number	Ion	Comp.	v (km s^{-1})	b (km s^{-1})	log N (cm^{-2})
59717.....	Mg II	1	6.64 ± 0.80	4.20 ± 0.38	13.36 ± 0.19
		2	14.63 ± 1.11	1.89 ± 0.57	13.06 ± 0.28
		3	21.25 ± 0.13	1.89 ± 0.16	12.98 ± 0.13
		4	83.68 ± 0.10	3.94 ± 0.14	12.079 ± 0.011
25025.....	Mg II	1	19.547 ± 0.017	2.386 ± 0.024	12.4861 ± 0.0044
	Mg II	2	56.47 ± 0.10	2.56 ± 0.11	12.194 ± 0.017

Table 4.6: Fits for carbon lines for magnesium lines shown in Figure 4.22

4.5 Depletion

Calculated depletions as described by Section 3.6 shown in Table 4.7.

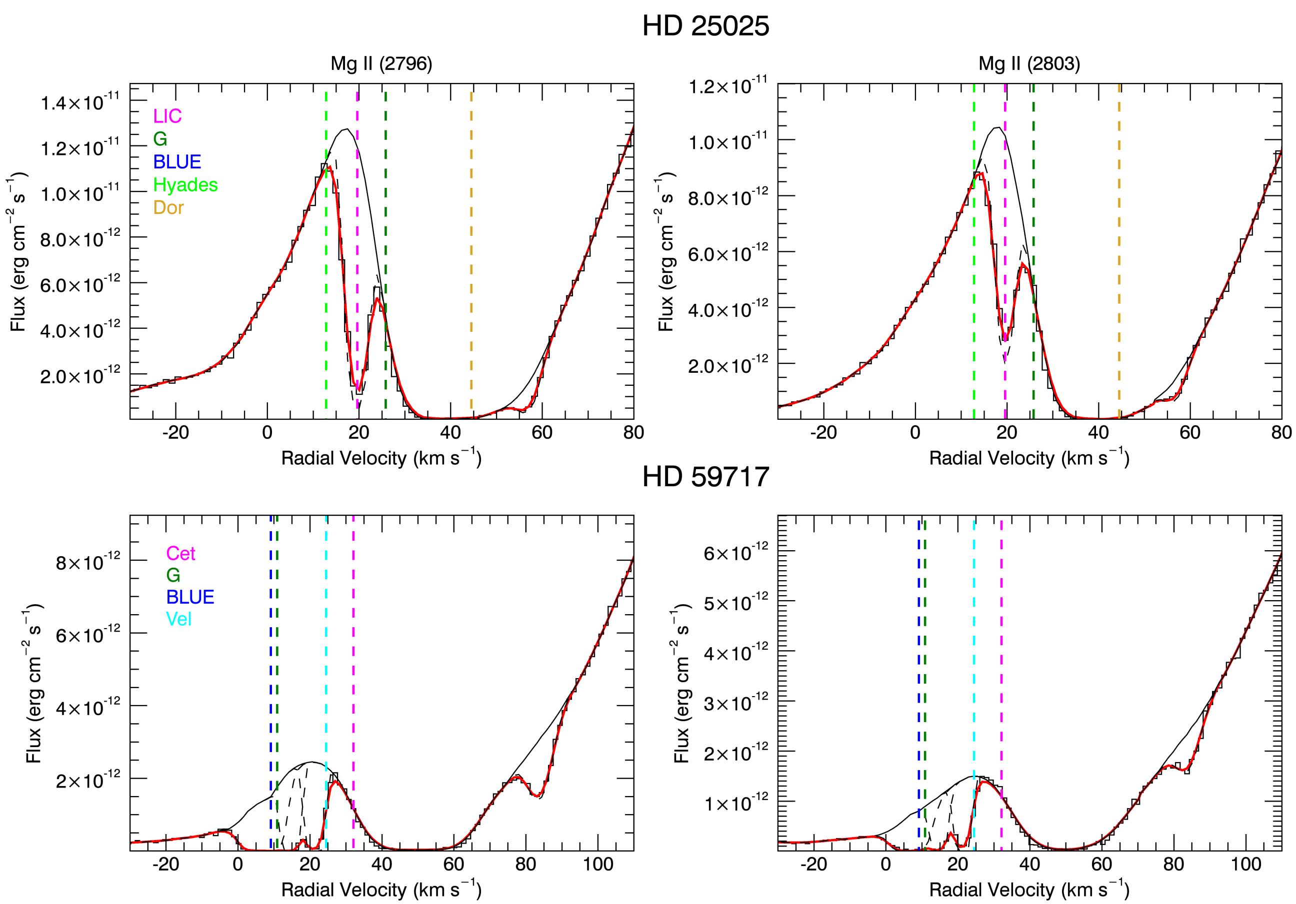

Figure 4.22: The upper profiles are magnesium fits for HD 25025 and the bottom are magnesium fits for HD 59717. The dashed vertical lines show the possible clouds responsible for the absorption features that traverse or are within 20 degrees of the line of sight according to Redfield's Kinematic Model (Redfield & Linsky 2008).

HD Number	Ion	Comp. #	Depletion (dex)	Dust (cm^{-2})
48915.....	C II	1	$+0.09^{+0.26}_{-0.26}$	$0.0^{+0.0}_{-0.0}$
		2	$-0.23^{+0.28}_{-0.28}$	$13.54^{+0.27}_{-0.0}$
	Mg II	1	$-1.094^{+0.104}_{-0.104}$	$13.024^{+0.098}_{-0.100}$
		2	$-0.743^{+0.096}_{-0.096}$	$12.97^{+0.11}_{-0.11}$
	Si II	1	$-1.02^{+0.35}_{-0.35}$	$12.997^{+0.065}_{-0.101}$
		2	$-0.02^{+0.43}_{-0.43}$	$11.70^{+1.19}_{-0.0.0}$
	Fe II	1	$-1.26^{+0.14}_{-0.12}$	$12.956^{+0.056}_{-0.059}$
		2	$-0.936^{+0.075}_{-0.074}$	$12.926^{+0.059}_{-0.061}$
61421.....	C II	1	$-0.78^{+0.10}_{-0.10}$	$14.370^{+0.068}_{-0.073}$
		2	$-1.46^{+0.69}_{-0.69}$	$14.434^{+0.062}_{-0.115}$
	N I	1	$-0.79^{+0.17}_{-0.17}$	$13.763^{+0.087}_{-0.104}$
		2	$-0.77^{+0.22}_{-0.22}$	$13.760^{+0.094}_{-0.124}$
	O II	1	$-1.60^{+0.16}_{-0.16}$	$14.709^{+0.053}_{-0.055}$
		2	$-0.781^{+0.059}_{-0.059}$	$14.641^{+0.061}_{-0.063}$
	Mg II	1	$-1.91^{+0.26}_{-0.58}$	$13.585^{+0.094}_{-0.094}$
		2	$-1.30^{+0.44}_{-0.28}$	$13.57^{+0.10}_{-0.13}$
	Fe II	1	$-1.62^{+0.17}_{-0.22}$	$13.499^{+0.054}_{-0.055}$
		2	$-1.45^{+0.49}_{-0.26}$	$13.494^{+0.057}_{-0.084}$
62509.....	C II	1	$-0.85^{+0.33}_{-0.33}$	$14.584^{+0.086}_{-0.14}$
		2	$-0.71^{+0.23}_{-0.23}$	$14.556^{+0.092}_{-0.133}$
	O II	1	$-0.989^{+0.097}_{-0.097}$	$14.873^{+0.060}_{-0.063}$
		2	$-1.03^{+0.10}_{-0.10}$	$14.877^{+0.059}_{-0.062}$
	Mg II	1	$-1.137^{+0.097}_{-0.097}$	$13.757^{+0.097}_{-0.099}$
		2	$-1.62^{+0.10}_{-0.10}$	$13.780^{+0.092}_{-0.093}$
	Fe II	1	$-1.445^{+0.087}_{-0.084}$	$13.694^{+0.053}_{-0.054}$
		2	$-1.848^{+0.098}_{-0.093}$	$13.704^{+0.051}_{-0.052}$
432.....	C II	1	$-0.714^{+0.055}_{-0.055}$	$14.427^{+0.062}_{-0.064}$
	N I	1	$-1.287^{+0.060}_{-0.060}$	$13.887^{+0.063}_{-0.064}$
	Mg II	1	$-1.17^{+0.14}_{-0.13}$	$13.629^{+0.098}_{-0.102}$
	Fe II	1	$-1.45^{+0.10}_{-0.10}$	$13.564^{+0.053}_{-0.054}$

Table 4.7: Depletion values for all of the stars possible in the sample; many stars did not have hydrogen column densities and therefore could not be calculated. The 0.0's are caused by having an overabundance compared with solar values. This can be attributed to geocoronal absorption in the nitrogen and oxygen lines or suggests that the assumption of solar abundance is not correct for that line of sight.

For these four stars, only one ion is more abundant than what we observe in the Sun (Asplund et al. 2005). Our persisting issues with blending geocoronal absorption is shown in the overly depleted oxygen and nitrogen. From Frisch et al. (2011) we know that these elements have lower condensation temperatures and, therefore, should not be as depleted as iron, magnesium, and silicon.

4.6 Discussion

In this section we have presented data on all of the targets in our sample excluding the α Centauri stars. We have calculated radial velocities, Doppler parameters, and column densities for all but one star (HD 108903) for various ion transitions in the ultraviolet. From this, we have estimated temperatures and turbulent velocities for six of the ten stars. We will elaborate on stars that presented challenges or had interesting features in the following subsections.

4.6.1 HD 48915

HD 432, or β Cas, presented unexpected challenges because of strange features in the oxygen and nitrogen ion transitions in the far-UV. This is normally an indicator that there is geocoronal absorption from the particles in the outer edges of Earth's atmosphere absorbing light corresponding to those wavelengths. This is denoted by dashed green lines in Figure 4.23 and more information about geocoronal absorption in stellar spectra can be found in Section 2.8.

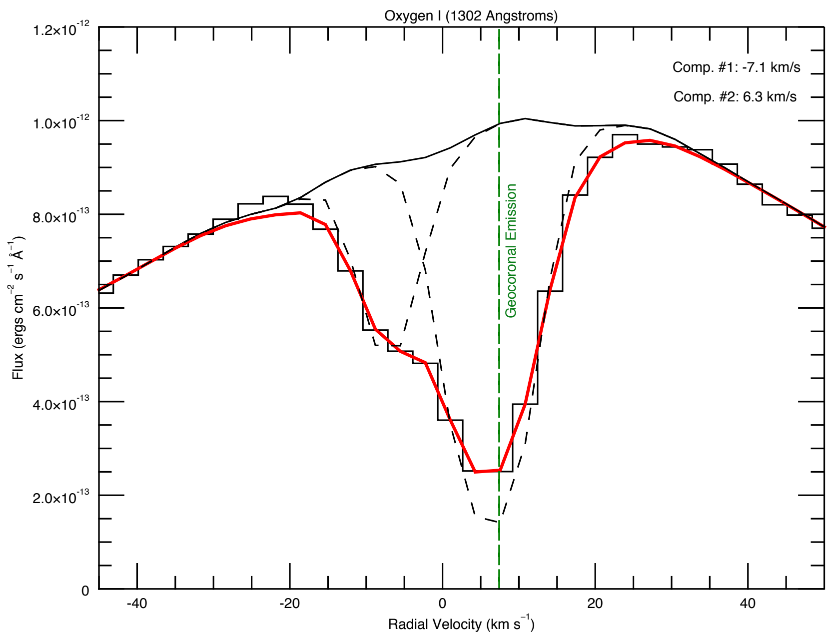

Figure 4.23: The HD 432 ground state oxygen feature at 1302 Å with the calculated radial velocity of the geocoronal emission calculated using Stumpff (1980).

What made this star more difficult than most to control for the geocoronal emission is that they overlap making it difficult to make an accurate approximation of the individual parameters of the ISM features. Because of this, nitrogen and oxygen were not used in the temperature and turbulence analysis. This is the same scenario for HD 48915 seen in Figure 4.3.

4.6.2 HD 172167

HD 172167 was the only star in the sample that had a prediction of three interstellar clouds traversing the line of sight. However, all of the ion transitions that we studied were either saturated or not visible. The only ions we were able to observe were the magnesium and iron double resonance lines, which were fully saturated as seen in Figure 4.5. We settled on two components because the F-test informed us that it was not substantially better to fit with three. All three fits can be seen in Figure 4.1.

4.6.3 HD 87901

HD 87901 was a fun and easy star to fit because of its high signal to noise using both E140H and E230H. Couple this with it being a hot star and you see beautifully simple continua. There are clearly two features visible and only one was predicted by the model. This star had been observed before but only by Vallerga et al. (1993), which only put a lower limit on the column density. We can now confidently say that there is a new cloud at $v_R \sim 15$ km s^{-1}. Gry & Jenkins (2017) recently published a paper identifying this new cloud and describing other characteristics of this line of sight within the last month.

4.6.4 HD 108903

HD 108903 is a high proper motion giant M star, which presented insurmountable problems. All observed ion transitions were saturated to the point that they were unable to be fit with any confidence. The saturation caused there to be an unknown number of components and made for arbitrary assumptions. We do not record any of my fits for this star. The challenge posed by this star are shown in Figure 4.24.

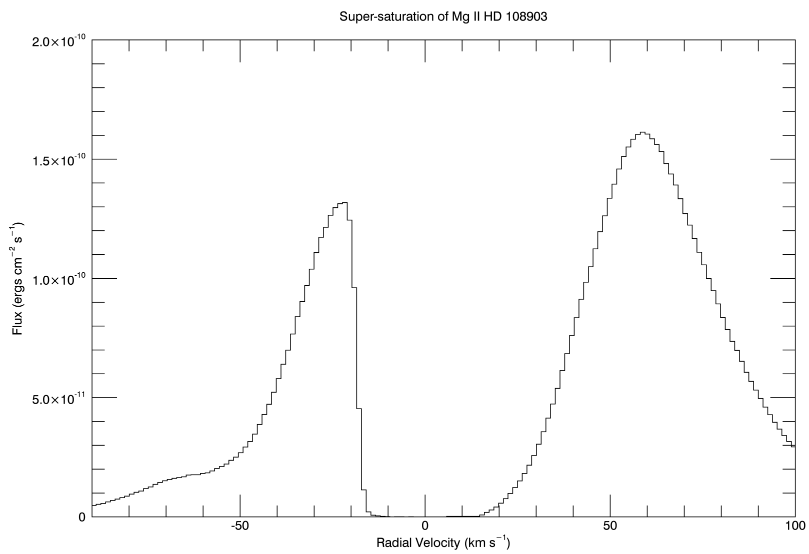

Figure 4.24: The HD 108903 Mg II line at 2796 Å showing extreme saturation that persists between all ions regardless of oscillator strengths.

Chapter 5

Conclusion

We have observed a total of thirteen stars from the ASTRAL sample taken in May of 2015 for interstellar medium absorption features across a range of ion transitions. From this, we have measured radial velocities, Doppler parameters, and column densities. This has led to the discovery of new interstellar clouds, an analysis of historical changes over a twenty year time scale for two stars in the sample, an adjusted size distribution of dust grains along the α Centauri line of sight based on in-situ observations of interstellar particle masses from Frisch et al. (1999), and new estimates for temperature, turbulence, depletion, and electron densities. After all of this, we can take a step back and look at how this compares with what has been observed, what has been predicted, and trends in this small sample. In Figure 5.1, we see general agreement between previous measurements of the radial velocity of the ISM absorption features and the May 2015 dataset from ASTRAL.

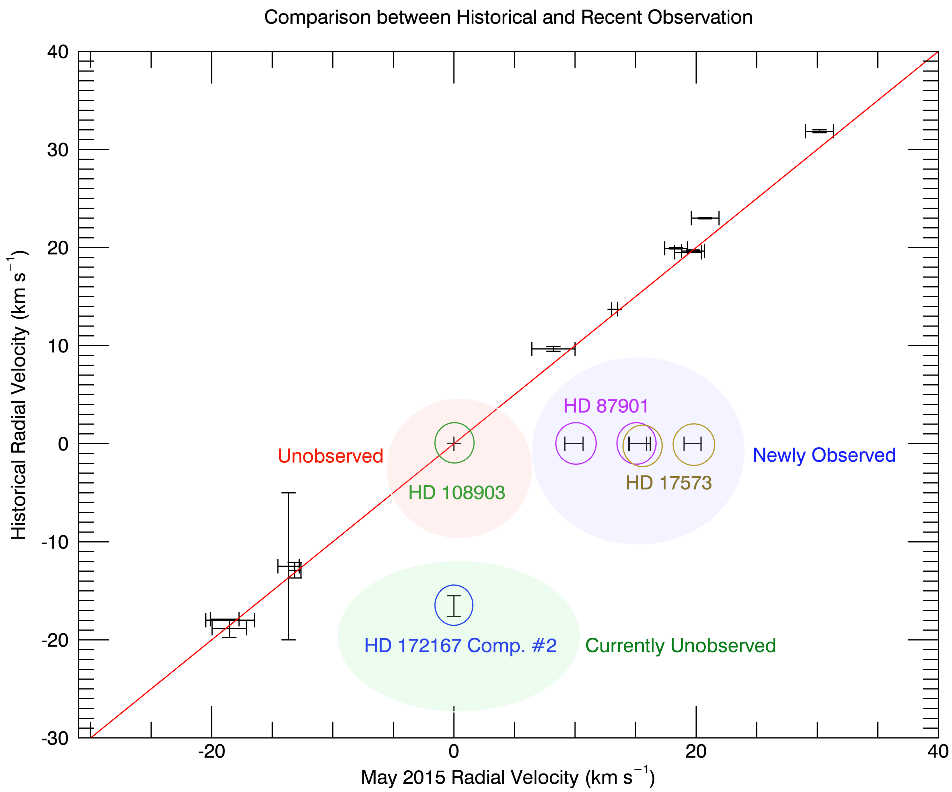

Figure 5.1: Historical radial velocity of components compared with new observations. The red line shows complete agreement between historical measurements and the ASTRAL spectra. Unobserved components or stars are shown along the zero axes.

From this, we see a new cloud along the HD 87901 line of sight, the first ISM observations of HD 17573, and a case of over saturation causing us to not be able to observe a triple component line of sight (Figure 4.1) After this we can look at the discrepancy between the Kinematic Model from Redfield & Linsky (2008) and our observations. (Figure 5.2)

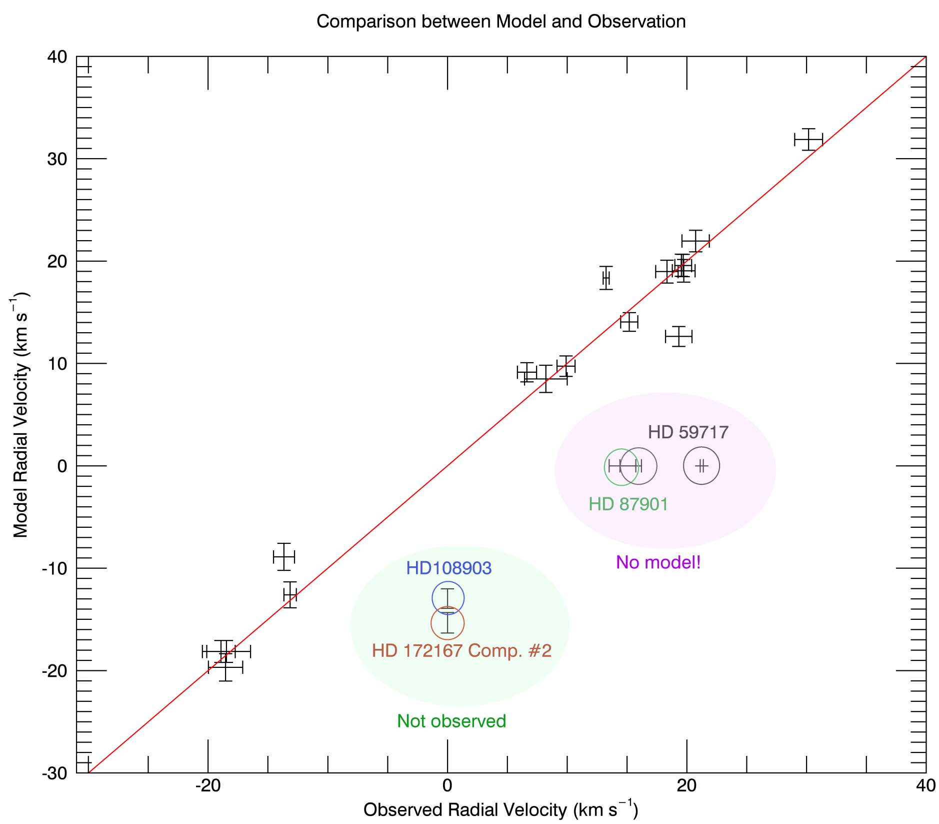

Figure 5.2: Model radial velocity prediction of components compared with new observations.

As expected we see the same trends from Figure 5.1 because the model is mostly based on these previous observations. It would we be valuable to observe the region surrounding HD 87901 to get the angular scale of this new cloud. This is addressed in part by Gry & Jenkins (2017).

Apart from HD 108903, we have observations of magnesium and iron for all stars and can look at general trends for the Doppler and column densities of each in Figure 5.3.

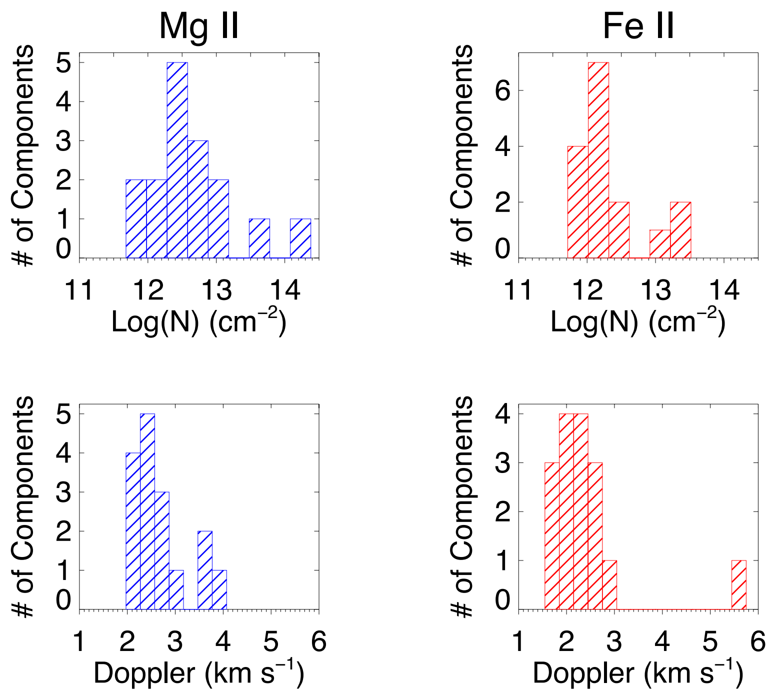

Figure 5.3: Distribution of column densities and Doppler parameters for all components of all stars in our sample.

From this figure, we see two components that stand out in the magnesium column densities, which are due to the over saturation of HD 164058 and HD 172167 as seen in Figure 4.9 and 4.5. This suggests that it may be more physically appropriate to have fit both stars with more components, however we need to find an ion transition without saturation to get an appropriate fit. Similarly, we see a very broad iron feature that is also caused by the over-saturation of HD 164058. Therefore, it is safe to say that this should be fit with two components even though it is not supported by an F-test.

The next comparisons we can make are between the measured temperatures from Redfield & Linsky (2004b) and our new observations shown in Table 5.1.

We can see a general trend toward cooler temperatures, however, most are within their errors.

HD Number	Comp.	$V_R$km s^{-1}	T (K)	ξ (km s^{-1})	Hist. T (K)	Hist. ξ (km s^{-1})	Cloud	Ions Used
128621.....	1	-18.93 ± 1.19	4884^{+504}_{-495}	$1.66^{+0.92}_{-0.64}$	5500^{+330}_{-320}	$1.37^{+0.34}_{-0.41}$	G	D I, O I, Mg II, Si II, Fe II
128620.....	1	-18.47 ± 2.01	4862^{+402}_{-397}	$1.17^{+1.17}_{-0.66}$	5100^{+1200}_{-1100}	$1.21^{+0.33}_{-0.49}$	G	D I, C II, Mg II, Si II, Fe II
48915.....	1	13.26 ± 0.25	12^{+12}_{-2407}	$2.46^{+0.36}_{-0.08}$	x	x	LIC	C II, Mg II, Fe II
	2	19.33 ± 1.11	4878^{+4878}_{-8301}	$1.93^{+1.93}_{-0.92}$	...	...	Blue	C II, Mg II, Fe II
61421.....	1	18.34 ± 0.94	4219^{+789}_{-670}	$2.18^{+1.27}_{-1.03}$	6710^{+660}_{-630}	$1.21^{+0.35}_{-0.45}$	LIC	D I, N I, Mg II, Fe II
	2	20.74 ± 1.14	3959^{+529}_{-550}	$3.22^{+0.25}_{-0.24}$	6710^{+660}_{-630}	$1.21^{+0.35}_{-0.45}$	Aur	D I, N I, Mg II, Fe II
62509.....	1	19.74 ± 0.95	8104^{+3884}_{-4395}	$1.84^{+0.71}_{-0.50}$	9000^{+1600}_{-1500}	$1.67^{+0.27}_{-0.32}$	LIC	D I,C II, N I, O I, Mg II, Fe II
	2	30.18 ± 1.17	8553^{+3803}_{-2716}	$0.00^{+0.00}_{-1.64}$	6100^{+3100}_{-2600}	$1.93^{+0.79}_{-0.59}$	Gem	D I, C II, N I, O I, Mg II, Fe II
432.....	1	8.22 ± 1.78	5524^{+4614}_{-5165}	$5.26^{+2.08}_{-1.74}$	9760^{+800}_{-880}	$0.0^{+1.1}_{-0.0}$	LIC	D I, C II, Mg II, Fe II
87901.....	1	9.91 ± 0.75	5921^{+1181}_{-1178}	$1.55^{+0.25}_{-0.21}$	...	...	Leo	C II, N I, Mg II, Si II, Fe II
	2	15.31 ± 0.90	3697^{+3697}_{-3722}	$2.31^{+1.01}_{-0.79}$	...	...	Unknown	C II, N I, Mg II, Si II, Fe II
17573.....	1	15.19 ± 0.71	6274^{+6134}_{-5145}	$0.97^{+0.97}_{-1.35}$	...	...	LIC	C II, N I, O I, Mg II, Si II, Fe II
	2	19.70 ± 0.70	6815^{+6815}_{-7714}	$1.88^{+1.88}_{-1.24}$	...	...	Hyades	C II, N I, O I, Mg II, Si II, Fe II

Table 5.1: Temperature and turbulence analysis compared with previously observed value from Redfield & Linsky (2004b)

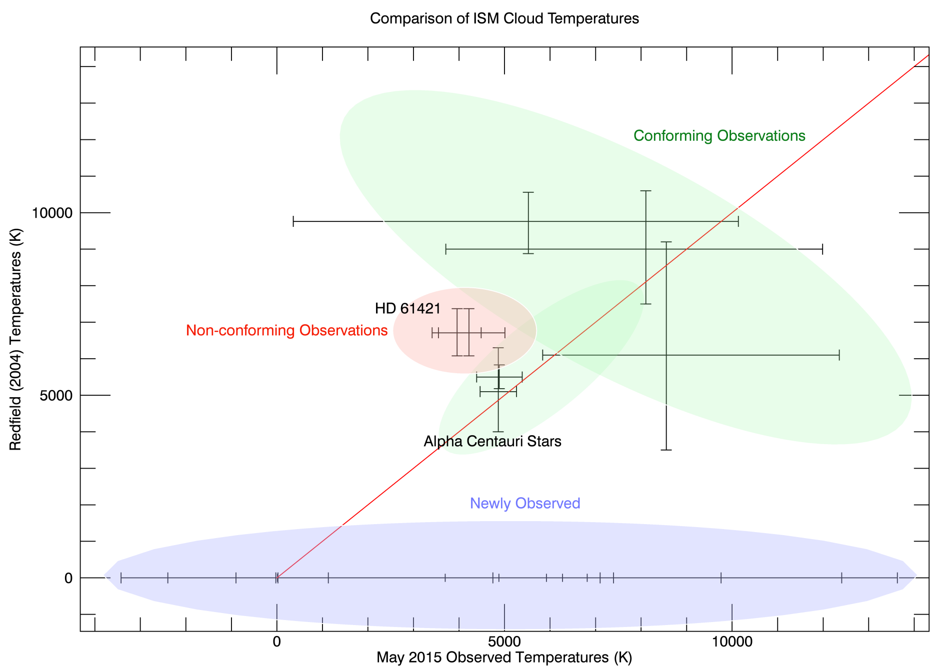

Figure 5.4: Comparison of the temperatures measured in Redfield & Linsky (2004b) with this study. This shows three populations: conforming measurements, non-conforming measurements, and new measurements.

Next, we compared the turbulent velocities (ξ) and see that we generally predict higher velocities but again are mostly within the errors.

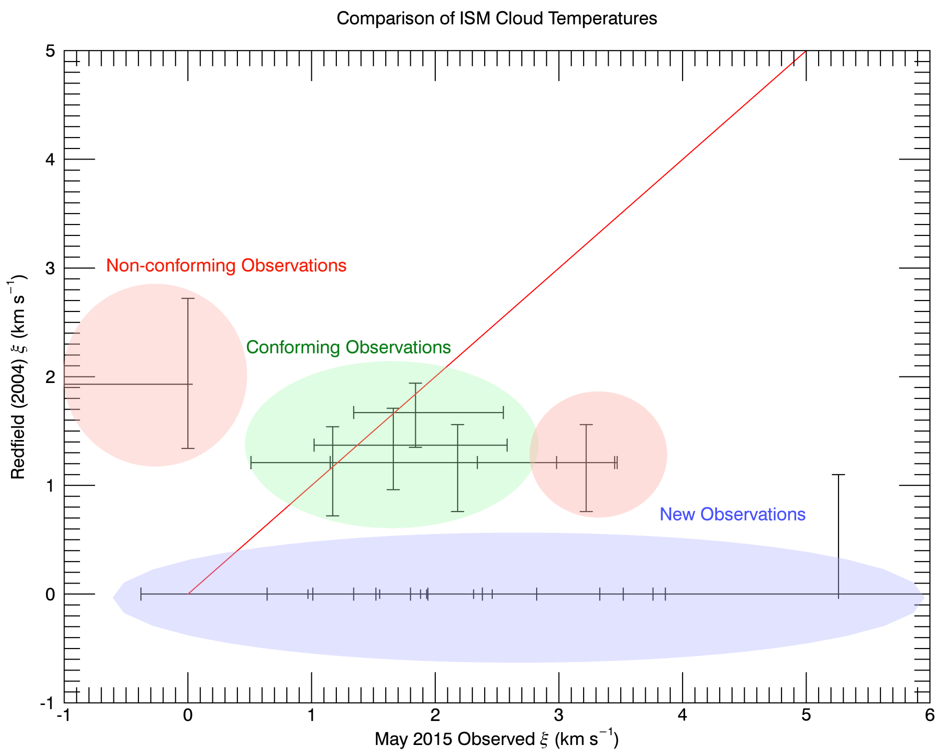

Figure 5.5: Comparison of the turbulent velocities observed in Redfield & Linsky (2004b) with this study. This shows three populations: conforming measurements, non-conforming measurements, and new measurements.

Our sample has provided new temperature and turbulence measurements of HD 87901, HD 17573, and HD 48915. Because the errors in some components is very large, we hope to be able to constrain them further by observing more oxygen lines in order to mitigate blending from geocoronal absorption.

5.1 Back to *Breakthrough Starshot*

As shown and discussed in Chapter 3, we have calculated a lower-limit probability for a single StarChip to encounter a dust grain larger than 4 μm along the line of sight. For the 1000 chips they intend to send, the likelihood that one of those will be hit by a grain larger than 4μm is $\sim 4.01\%$. However, a more significant problem will likely be the erosion caused by constant collisions with sub-micron grains that crater the surface of the chip through transient spot heating (Hoang et al. 2016). Collisions will also cause heating of the nanocrafts and will likely result in some melting because the cooling timescale is longer than the collision rate. The apparent decrease in temperature along the line of sight shown in Table 5.1 over the last decade may not be statistically significant, however it would imply the condensation of more gas into dust grains and an increase in larger grains. The increase in turbulent velocities, however, points to increased shattering of grains (Hirashita & Yan 2009). The interstellar medium in this region is significantly lower than the estimates that Hoang et al. (2016) used for the local interstellar medium. This should result in less heating of the StarChips.

Even with our adjustment of the Weingartner & Draine (2001) grain size distribution, the likelihood of complete destruction of the chip by a single large dust grain is highly unlikely. This is good news for *Breakthrough Starshot* because there is little they can do to avoid or lessen these collisions as the chips race through the medium at $v \sim 0.2c$. Shielding against the cratering of grains $a \sim 1\mu$m will be the deciding factor on whether these chips can withstand the journey through the interstellar medium.

5.2 Future Work

I have been working on this project for over two years now and have learned a great deal in the process. However, there is plenty more that we are able to do with these incredible high-resolution spectra. We would like to extend the chapter on α Centauri into a published paper by further investigating the specific interstellar conditions that *Breakthrough Starshot* will likely encounter. This would be a follow up paper to Hoang et al. (2016). In order to do this however, a lot more work must be done. There are other important ion transitions that we could fit to further constrain temperature and turbulence such as aluminum and more oxygen lines. These oxygen lines would also help mitigate blending of geocoronal absorption observed in both oxygen and nitrogen profiles. We can estimate electron densities with magnesium and silicon transitions, in addition to the carbon transitions we have used thus far. This would give us multiple checks on our values.

We would like to extend the Weingartner & Draine (2001) model to incorporate other compositions such as pyroxene molecules that are likely present in the local interstellar medium (Draine 2011). In addition to this, it would be more comprehensive to apply our data to the whole range of cases, R_V values, and b_C values. From this we can place further constraints on the range of possible probabilities for such grains.

Bibliography

Anglada-Escudé, G., et al. 2016, Nature, 536, 437

Asplund, M., Grevesse, N., & Sauval, A. J. 2005, in Astronomical Society of the Pacific Conference Series, Vol. 336, Cosmic Abundances as Records of Stellar Evolution and Nucleosynthesis, ed. T. G. Barnes, III & F. N. Bash, 25

Ayres, T. R. 2010, Apjs, 187, 149

—. 2015, Apj, 149, 58

Beech, M. 2015, Alpha Centauri (Springer)

Berghfer, T. W., & chwerdt, D. Breit. 2002, Aap, 390, 299

Bertin, P., Vidal-Madjar, A., Lallement, R., Ferlet, R., & Lemoine, M. 1995, Aap, 302, 889

Boulanger, F., Cox, P., & Jones, A. P. 2000, in Infrared Space Astronomy, Today and Tomorrow, ed. F. Casoli, J. Lequeux, & F. David, 251

Breakthrough. ????, Breakthrough Announcement (2016), year = 2016, howpublished = `https://breakthroughinitiatives.org/News/4`, note = Accessed: 2015-04-14

Cardelli, J. A., Clayton, G. C., & Mathis, J. S. 1989, Apj, 345, 245

Draine, B. T. 2011, Physics of the Interstellar and Intergalactic Medium (Princeton University Press)

Dring, A. R., Linsky, J., Murthy, J., Henry, R. C., Moos, W., Vidal-Madjar, A., Audouze, J., & Landsman, W. 1997, Apj, 488, 760

Ebel, D. S. 2000, Jgr, 105, 10363

Fisk, L. A., & Gloeckler, G. 2014, Apj, 789, 41

Francis, C., & Anderson, E. 2014, Mnras, 441, 1105

Frisch, P. C., et al. 1999, Apj, 525, 492

Frisch, P. C., Redfield, S., & Slavin, J. D. 2011, Araa, 49, 237

Galeazzi, M., et al. 2014, Nat, 512, 171

Goldsmith, D. W., Habing, H. J., & Field, G. B. 1969, Apj, 158, 173

Grisdale, K., Agertz, O., Romeo, A. B., Renaud, F., & Read, J. I. 2017, Mnras, 466, 1093

Gry, C., & Jenkins, E. B. 2017, Aap, 598, A31

Hartkopf, W. I., Mason, B. D., & Worley, C. E. 2001, Aj, 122, 3472

Hébrard, G., Mallouris, C., Ferlet, R., Koester, D., Lemoine, M., Vidal-Madjar, A., & York, D. 1999, Aap, 350, 643

Heger, A., Fryer, C. L., Woosley, S. E., Langer, N., & Hartmann, D. H. 2003, Apj, 591, 288

Hirashita, H., & Yan, H. 2009, Mnras, 394, 1061

Hoang, T., Lazarian, A., Burkhart, B., & Loeb, A. 2016, ArXiv e-prints

IPAC, C. ????, IPAC Cal Tech (2008), publisher = http://coolcosmos.ipac.caltech.edu/cosmic_classroom/ir_tutorial/images/transmission.jpg, note = Accessed: 2015-04-14, year = 2008

Jakosky, B. M., Pepin, R. O., Johnson, R. E., & Fox, J. L. 1994, Icarus, 111, 271

Jenkins, E. B. 2009, Apj, 700, 1299

Kameswara, Rao, R. 1984, Bulletin of the Astronomical Society of India, 81

Lallement, R., Bertin, P., Ferlet, R., Vidal-Madjar, A., & Bertaux, J. L. 1994, Aap, 286, 898

Lallement, R., Ferlet, R., Lagrange, A. M., Lemoine, M., & Vidal-Madjar, A. 1995, Aap, 304, 461

Lammer, H., et al. 2009, The Astronomy and Astrophysics Review, 17, 181

Li, A., & Draine, B. T. 2001, Apj, 554, 778

Linsky, J. L., Diplas, A., Wood, B. E., Brown, A., Ayres, T. R., & Savage, B. D. 1995, Apj, 451, 335

Linsky, J. L., & Wood, B. E. 1996, Apj, 463, 254

McKee, C. F., & Ostriker, J. P. 1977, Apj, 218, 148

Morton, D. C. 1991, Apjs, 77, 119

—. 2003, Apjs, 149, 205

Nussbaumer, H., & Storey, P. J. 1981, Aap, 96, 91

Osterbrock, D. E. 1989, Astrophysics of gaseous nebulae and active galactic nuclei (University of California)

Piskunov, N., Wood, B. E., Linsky, J. L., Dempsey, R. C., & Ayres, R. 1997, Apj, 474, 315

Pourbaix, D., et al. 2002, Aap, 386, 280

Redfield, S., & Falcon, R. E. 2008, Apj, 683, 207

Redfield, S., & Linsky, J. L. 2002, Apjs, 139, 439

—. 2004a, Apj, 602, 776

—. 2004b, Apj, 613, 1004

—. 2007, ArXiv e-prints

—. 2008, Apj, 673, 283

Reipurth, B., & Mikkola, S. 2012, Nat, 492, 221

Rodríguez-Merino, L. H., Chavez, M., Bertone, E., & Buzzoni, A. 2005a, Apj, 626, 411

—. 2005b, Apj, 626, 411

Slavin, J. D., & Frisch, P. C. 2002, Apj, 565, 364

Stumpff, P. 1980, Aaps, 41, 1

Trumpler, R. J. 1930, Pasp, 42, 214

Vallerga, J. V., Vedder, P. W., Craig, N., & Welsh, B. Y. 1993, Apj, 411, 729 van Leeuwen, F. 2007, Aap, 474, 653

Weingartner, J. C., & Draine, B. T. 2001, Apj, 548, 296

Witze, A. 2016, Nat, 536, 381

Wolfire, M. G., Hollenbach, D., McKee, C. F., Tielens, A. G. G. M., & Bakes, E. L. O. 1995, Apj, 443, 152

Wolszczan, A., & Frail, D. A. 1992, Nat, 355, 145

Wood, B. E., Linsky, J. L., Hébrard, G., Williger, G. M., Moos, H. W., & Blair, W. P. 2004, Apj, 609, 838